M 2014

U.PORTO
FEUP FACULDADE DE ENGENHARIA
UNIVERSIDADE DO PORTO

PREPARATION AND OPTIMIZATION OF HEMATITE PHOTOANODES FOR HYDROGEN PRODUCTION FROM PHOTOELECTROCHEMICAL CELLS

ANTÓNIO MAXIMINO NOGUEIRA VILANOVA

TESE DE MESTRADO APRESENTADA
À FACULDADE DE ENGENHARIA DA UNIVERSIDADE DO PORTO EM
MIEA - MESTRADO INTEGRADO EM ENGENHARIA DO AMBIENTE

U.PORTO
FEUP FACULDADE DE ENGENHARIA
UNIVERSIDADE DO PORTO

MESTRADO INTEGRADO EM ENGENHARIA DO AMBIENTE 2013/2014

PREPARATION AND OPTIMIZATION OF HEMATITE PHOTOANODES FOR HYDROGEN PRODUCTION FROM PHOTOELECTROCHEMICAL CELLS

ANTÓNIO MAXIMINO NOGUEIRA VILANOVA

Dissertation presented to obtain the degree of

MASTER IN ENVIRONMENTAL ENGINEERING

President of the Jury: Cidália Maria de Sousa Botelho

Assistant Professor in the Chemical Engineering Department at FEUP

Supervisor: Luísa Manuela Madureira Andrade Silva

Assistant Researcher in the Chemical Engineering Department at FEUP

Co-Supervisor: Adélio Miguel Magalhães Mendes

Associated Professor in the Chemical Engineering Department at FEUP

July 2014

"Why does the eye see a thing more clearly in dreams than the imagination when awake?"

Leonardo da Vinci

ACKNOWLEDGMENTS

First I would like to thank my supervisor Dr. Luísa Andrade Silva for giving all necessary instructions and for having continuously monitored the progress of my work. I am very grateful for all the availability, patience and motivation, especially in times of increased anxiety and workload. I am also very thankful to my supervisor for allowing me to complete my course on the subject of renewable energies, since for me the opportunity to work in the engineering area I like best was the biggest motivational factor I had.

I also have to make a heartfelt thanks to my co-supervisor, Professor Adélio Mendes, for giving me the opportunity to do this dissertation with Solar Group in a laboratory with so privileged working conditions and for his inspirational example.

I would like to make a very special thanks to Paula Dias for being such a helpful co-worker. Despite all the setbacks and adversities that happened throughout this work, she never failed in giving me all the necessary help and cooperation. I am also very grateful for all the transmitted knowledge, friendliness, optimism and enthusiasm that allowed me to do this dissertation in a truly enviable working environment.

I am also very grateful to all members of the Solar Group, for hosting me so well and for always being so readily helpful in any situation. Whether in times of work, or in moments of conviviality, I've learned a lot at professional and personal level.

I cannot forget thanking all my friends at FEUP for all the good times we spent and for always having been a source of happiness and encouragement, namely the lunch group (André C. André G., Carla, Hélder, Nuno, and Rafael).

Last but not least, I express my warm gratitude to my mother Lucília, my father Manuel and my sisters Mariana and Madalena, the most important people to me, to whom I owe much of who I am.

ABSTRACT

The search for efficient, renewable and clean technological solutions for energy production able to satisfy the enhanced mankind energy demand is an important concern of the scientific community and, in particular, for environmental engineering. So far, the sun is our primary source of clean and abundant energy and it is the most powerful resource able to supply the world energy needs. Photoeletrochemical water splitting with semiconductor photoelectrodes is a practical way to convert solar energy into a renewable fuel. Due to its abundance, low cost, stability and capability of absorbing light with wavelengths longer than 400 nm, hematite has been considered a very promising material for water splitting.

In this work, spray pyrolysis technique was chosen to deposit hematite films because it allows high reproducibility of stable samples, it has easy operation steps and it does not require the use of expensive equipment. This study focused on two key aspects to improve the photoresponse of hematite photoanodes: (1) optimization of the hematite morphology; (2) reduction of the required overpotential. For the hematite morphology control a *Design of Experiments* study was performed to optimize the experimental setup. The DoE software calculated the optimal operating conditions being: sprayed solution volume of 70 ml, spray nozzle height of 20 cm and 45 s time gap between sprays. Based on these conditions, the mathematical model predicted a maximum current density of 0.525 $mA \cdot cm^{-2}$. A pre-treatment with TEOS was also performed to reduce the interfacial strain between the FTO and hematite crystals, leading to better Fe_2O_3 film organization. This treatment yielded a much higher current density and a lower onset potential, allowing producing a current density of 0.601 $mA \cdot cm^{-2}$ at 1.45 V_{RHE}, which represented an increase of ~29 % on the performance of the sample. It was found that 450 °C was the optimal temperature for hematite deposition, which allowed reaching a current density of 0.730 $mA \cdot cm^{-2}$. Top view SEM images confirmed that the deposition at 450 °C allowed obtaining hematite structures with a well-defined cubic shape. Considering the state-of-the-art of hematite photoanodes doping, silicon[IV] and titanium[IV] were the dopants chosen to be tested in this study. Apparently Ti[IV] doping seemed to favour a better crystal growth and allowed obtaining improvements in terms of working potential (onset potential moved to lower values and dark current moved to higher potentials).

One of the most important contributions and perhaps the most innovative aspect of this work was the stability test that was performed. After 168 h of simulated sunlight exposure, the tested sample showed an improvement in its performance of more than 6 % in relation to the first *I-V* measurement, having never lost efficiency over this period.

KEYWORDS: Water Splitting, Photoeletrochemical Hydrogen Production, Hematite Photoanodes, Spray Pyrolysis, Hematite Doping, DoE, Photoanode Stability Test

RESUMO

A procura de soluções tecnológicas eficientes, renováveis e limpas que possam satisfazer as necessidades energéticas da humanidade é um assunto de muita relevância para a comunidade científica, em particular para a engenharia do ambiente. Até ao momento, o Sol é a nossa fonte primária de energia limpa e abundante e é também o recurso energético com maior capacidade para satisfazer as necessidades energéticas mundiais. A separação fotoeletroquímica da molécula de água através de fotoelétrodos semicondutores é uma forma prática de converter energia solar num combustível renovável. Devido à sua abundância, baixo custo, estabilidade e capacidade de absorver luz com comprimentos de onda superiores a 400 nm, a hematite tem sido considerada um material muito promissor para a eletrólise da água.

Neste trabalho a técnica de pirólise por *spray* foi escolhida para fazer a deposição de filmes de hematite devido à sua capacidade para produzir amostras estáveis e com reprodutibilidade, facilidade de operação e utilização de equipamentos de baixo custo. Este trabalho focou-se em dois aspetos fundamentais para melhorar a resposta dos fotoânodos: (1) otimização da morfologia de hematite; (2) redução do sobrepotencial de ativação. Para o controlo da morfologia da hematite foi feito um estudo de *DoE* com o objetivo de otimizar a instalação experimental. O software calculou as condições de deposição ótimas: volume de solução pulverizada de 70 ml, altura do *spray* de 20 cm e intervalo de tempo entre sprays de 45 s. Para estas condições, o modelo matemático previu uma densidade de corrente máxima de 0.525 $mA \cdot cm^{-2}$. Fez-se pré-tratamento com TEOS para reduzir a tensão da interface entre o FTO e os cristais de hematite, permitindo obter uma melhor organização estrutural do filme. Este pré-tratamento permitiu obter densidades de corrente maiores para 1.45 V_{RHE}, tendo-se alcançado o valor de 0.601 $mA \cdot cm^{-2}$, o que representa uma melhoria de ~29% na performance da amostra. Constatou-se que 450 °C era a temperatura ótima para as deposições de hematite, permitindo obter uma densidade de corrente de 0.730 $mA \cdot cm^{-2}$ para 1.45 V_{RHE}. Imagens de SEM confirmaram que nestas condições se produziu uma morfologia diferente, tendo-se formado estruturas cúbicas. Tendo em conta outros estudos sobre dopagem de fotoânodos de hematite, testou-se o silício[IV] e o titânio[IV] como dopantes. Aparentemente, a dopagem com Ti[IV] favoreceu o crescimento dos cristais e permitiu alcançar melhorias ao nível do potencial de trabalho (o sobrepotencial de ativação baixou e a *dark current* apareceu para potenciais mais altos).

Um dos contributos mais importantes deste trabalho e talvez o aspeto mais inovador foi o estudo de estabilidade realizado. Após 168 h de exposição contínua à luz solar, a amostra testada mostrou uma melhoria na sua eficiência de mais de 6 % em relação à primeira medição *I-V*, nunca tendo perdido eficiência ao longo deste período.

PALAVRAS-CHAVE: Eletrólise da Água, Produção Fotoeletroquímica de Hidrogénio, Fotoânodos de Hematite, Pirólise por Spray, Dopagem de Hematite, DoE, Teste de Estabilidade em Fotoânodos

I declare, under oath, that this work is original and that all non-original contributions were properly referenced with identifying the source.

António Maximino Nogueira Vilanova

Porto, 4 de Julho de 2014

LIST OF CONTENTS

LIST OF FIGURES

LIST OF TABLES

NOMENCLATURE

VARIABLES

Variable	Definition	Unit
A	Absorbance	%
E_c	Potential of the edge of the conduction band	V
E_F	Fermi level	V
E_g	Bandgap	eV
E_{Redox}	Redox potential or electrolyte energy mediator	V
E_V	Potential of the valence band edge	V
h	Planck constant, $6.6260693(11)\times10^{-34}$	J·s
I	Current	A
J	Current density	$mA\cdot cm^{-2}$
pH	Ionic Hydrogen Potential	pH scale values
v	Speed of light, 3.0×10^8	$m\cdot s^{-1}$
V	Potential	V
$V_{Applied}$	Applied bias potential	V
V_{fb}	Flatband potential	V
W	Depletion layer	nm

GREEK SYMBOLS

Greek Symbol	Definition
α	Absorption coefficient

SUPERSCRIPTS

Superscripts	Definition
°	Standard

SUBSCRIPTS

Subscripts	Definition
e^-	Electrons (identified by “n”)
h^+	Holes (identified by “p”)

ABBREVIATIONS

Abbreviation	Definition
AAO	Anodic aluminium oxide
ALD	Atomic layer deposition
APCVD	Atmospheric pressure chemical vapour deposition
AM	Air mass
CE	Counter electrode
CVD	Chemical vapour deposition
DoE	Design of Experiments
FM	Frank-van der Merwe
FTO	Fluorine doped tin oxide
HPLC	High-performance liquid chromatography
LEPABE	Laboratory for Process Engineering, Environment, Biotechnology and Energy
NHE	Normal hydrogen electrode
OER	Oxygen evolution reaction
PEC	Photoelectrochemical
QFL	Quasi Fermi level
RE	Reference electrode
RHE	Reversible hydrogen electrode
SCE	Saturated calomel electrode
SK	Stranski-Krastanov
STH	Solar-to-hydrogen conversion efficiency
TCO	Transparent conducting oxides
TEOS	Tetraethyl orthosilicate
UV	Ultra-violet
VW	Volmer-Weber
WE	Working electrode

1 INTRODUCTION

1.1 BACKGROUND AND MOTIVATION

A concept that has gained increasing relevance in the 21st century is sustainable development. The United Nations World Commission on Environment and Development (WCED) in its 1987 report *Our Common Future* defined sustainable development as the development that seeks to meet the needs of the present generation without compromising the ability of future generations to meet their own needs. This means enabling now and in the future people to achieve a satisfactory level of social and economic development and human and cultural achievement making at the same time a reasonable use of land resources and preserving the species and natural habitats [1]. This concept is based on three main pillars: environmental, economic and socio-political. There should be a reciprocal and balanced interaction between these domains to achieve sustainability [2].

It is known that human beings have sacrificed the ecological balance of the planet Earth in the past years to benefit from improved living conditions, more comfort for day-to-day tasks and to have access to technological development that reduces the effort required to achieve their objectives. All this desire for a lifestyle of comfort and tranquillity led to one of the greatest challenges that mankind faces today: the need to provide energy for meeting those desired living standards [2, 3]. It is therefore imperative to search for efficient and clean technological solutions able to satisfy the mankind energy demand which is a matter of particular importance for an environmental engineer.

By 2011 the global population power consumption was around 15 TW and it is expected to reach 30 TW by 2050. Fossil fuels, which currently provide about 85 % of mankind energy supply, will be unable to keep up this increase on demand [3]. The resulting increase of fossil fuels price is considerable and it is expected to continue rising until prohibitive levels. Even though the negative impact on the economy is very significant and cannot be ignored, the emission of greenhouse gases is perhaps a far more serious concern with a detrimental effect on climate change, which is already apparent. Therefore, there is an urgent need to develop alternative and environmentally friendly fuels [2, 4]. The world is heading towards the hydrogen economy with the hope that hydrogen will be a sustainable fuel for the future [3-5]. As much as 450 billion m^3 of hydrogen are currently produced in the world, most are consumed as raw material for producing various other chemicals and not as a fuel [6].

So far, the sun is our primary source of clean and abundant energy and is the most powerful resource able to supply the world energy needs [7]. However, solar energy also has a set of problems and challenges that need to be solved as soon as possible so that this energy source

will become truly attractive for the global economy. The main problems are related to its intermittency (day/night cycles and weather conditions) and consequent energy storage, enabling its usage at any moment and in the required quantities without restrictions. Based on these considerations, it becomes evident that besides the production of electricity from photovoltaic cells it is necessary to find a way to convert solar energy into a fuel that can be stored and transported to the consumer. Water is a convenient and abundant source of hydrogen. Around 3.5×10^{13} l of water is needed to store the energy consumed in one year in the form of hydrogen, but it represents only 0.000002 % of the total amount of water contained in oceans [3]. Photoeletrochemical (PEC) water splitting is a practical way to convert solar energy into a renewable fuel with several advantages [3, 4, 6]. Firstly, hydrogen is produced in a separate electrode, so no additional energy for its separation and purification is required. Secondly, no energy for heating the system is needed since it works at room temperature. Thirdly, the materials used for this process can be entirely inorganic, which offers a chemical robustness and durability that is difficult to achieve from biological systems [3, 8].

In the last few years, research on water splitting technologies emerged as an area of great interest and remarkable breakthroughs on the development of such systems have been achieved. By splitting water using PEC systems instead of typical electrolysers, the need for independent electricity generation is avoided, as is the need for grid connection. Moreover, solar hydrogen production by water splitting also opens the way to a significant CO_2 emissions reduction [9]. Finally, in a PEC cell system, the functions of solar cell and electrolyser are combined in a single device, which is favourable in terms of packaging and overall systems costs. There are still some key challenges that must be addressed to turn PEC cells into an economically viable option, mainly in what concerns the produced photocurrent. This should be of about 8 $mA \cdot cm^{-2}$, the minimum required to reach 10 % efficiency, which is the target for commercialization [10].

1.2 OBJECTIVES OF THIS WORK AND PROJECT PRESENTATION

This dissertation aimed to contribute to the study of hematite deposition optimization by spray pyrolysis and doping materials for hematite photoelectrodes, targeting maximum performance. The present work included the assembly and optimization of an experimental setup to perform spray pyrolysis depositions of hematite films with high photoelectrochemical performance. The assembled setup was based on previous reported works [11, 12]. Several tests were performed to optimize the experimental setup for bare hematite deposition. Additionally, some different doping materials and concentrations were tested.

Besides the engineering component of assembling an experimental setup from the very beginning, the development of this project enabled a systematic learning about the phenomena involved in the solar hydrogen production by water splitting.

1.3 LABORATORY PRESENTATION

LEPABE (Laboratory for Process Engineering, Environment, Biotechnology and Energy) is a research unit operating within the Faculty of Engineering of the University of Porto. Its scientific interests are focused on Chemical, Environmental and Biological Engineering and related fields. LEPABE's permanent staff includes 22 scientists who supervise around 75 research students. LEPABE's scientific architecture comprises 3 main target areas: (1) Environment and Health; (2) Energy, Processes and Products; (3) Biotechnology and Interfaces. LEPABE emphasizes the cross-feeding of different fields and, therefore, scientists are stimulated to work in cooperation with colleagues coming from different specialized fields, in this and other Units, looking at increasing synergies and seeking for advances in interfacial areas.

The scientific background of LEPABE's permanent staff is multidisciplinary, which has proven to be very helpful supporting the development of the three target areas mentioned above, as well as of other emerging areas such as nano-science and new energy technologies. The staff's fundamental skills include separation and catalytic membrane reaction science, advanced mathematical simulation and modelling, chemistry of trace compounds, surface science, environmental biotechnology and molecular biology, water quality, waste solid, liquid and gas treatment, automatic process control and transport phenomena.

The present and future contributions of Chemical, Environmental and Biochemical Engineering rely upon the combined development of in-depth molecular unravelling and modelling, in order to cope with the demands of new/innovative products and energy sustainable processes, capable of integrating eco-efficiency and health concerns together with economically sound and flexible design and operation. The diversified expertise of LEPABE's staff members is an indisputable asset that enables this Unit to tackle such challenge.

A distinct feature of LEPABE's activities has always been the ability to articulate the search for scientific advances with technological applications and innovative solutions, including a number of patents already approved. This has enabled fruitful collaborations with industrial companies and institutional bodies in the fields of polymers, food processing, paint technology, water, waste-water, solid waste and gas treatment, air quality and health, gas separation, oil refining, petrochemical processing, forest products and new energy production systems.

1.4 MAIN CONTRIBUTIONS OF THIS WORK

One of the main contributions of this work was the assembly and optimization of the spray pyrolysis setup for materials deposition, a technique that was not previously implemented in the host laboratory. This setup is of great importance for the researchers working on solar hydrogen production since it gives them the ability to prepare their own testing samples in an easy and fast process. Moreover, this setup can be used for other materials prepared in the host lab, such as titanium dioxide or graphene-based materials.

In particular, this work allowed the optimization of the experimental setup for hematite films deposition. The stability study of the produced samples is an important contribution of this work since in the literature only few studies reported the stability of the photoelectrodes for photoelectrochemical hydrogen production.

1.5 OUTLINE OF THIS WORK

Chapter 1 - Introduction

A brief introduction to the topic of hydrogen production from solar energy was made. The present situation of finding solutions to the mankind energy needs was contextualized and it was shown the importance of photoelectrochemical hydrogen production to achieve sustainable development. The objectives and contributions of this work were presented as well as the laboratory where this project was developed.

Chapter 2 – State of the Art

Important aspects of the PEC cells working mechanisms and their materials were discussed. An overview concerning the electrochemical techniques, such as current-voltage characteristics, was outlined. A brief description of the technologies evolution that has been implemented to obtain efficient hematite photoelectrodes was reported. A data collection of the best results achieved with the preparation of hematite photoelectrodes for hydrogen production and a research on which are the best materials for doping these photoelectrodes was performed.

Chapter 3 – Technical Description and Procedures

The spray pyrolysis technique and the assembly of the experimental setup used in this project were explained in detail. Procedures for the glass substrates production, deposition of materials, photoelectrochemical cell use and characterization of the produced photoelectrodes were described in this chapter. The methodology applied to determine the film thickness and to test the stability of samples was also explained.

Chapter 4 – Results and Discussion

The main results obtained in this study were presented and discussed in this chapter, namely which were the optimal conditions for hematite films deposition by spray pyrolysis, the results of the various studies made on the experimental setup components, specifically the dopants that have improved the samples efficiency and stability assessment.

2 STATE OF THE ART

2.1 THE PRINCIPLES BEHIND PHOTOELECTROCHEMICAL CELLS

A photoelectrochemical cell is composed by a photo-sensitive electrode and a counter-electrode, both immersed in an aqueous electrolyte solution [7]. The principal component of the PEC cell is the semiconductor, which converts incident photons to electron-hole pairs when exposed to sunlight [13]. Photons with energy $h \cdot v$ higher than semiconductor's bandgap generate electron-hole pairs ($e_{CB}^{-} + h_{VB}^{+}$) in the conduction and valence bands, respectively:

$$\text{Semiconductor} + hv \rightarrow (e_{CB}^{-} + h_{VB}^{+}) \tag{2.1}$$

Considering a typical n-type semiconductor, holes exhibit oxidation potential while the electrons are transferred over the external circuit to the cathode to promote water reduction into hydrogen gas [7]. In alkaline media, holes oxidize water to oxygen in the semiconductor surface (photoanode),

$$2h^{+} + 2OH^{-}\ (aq.) \rightarrow H_2O\ (l) + {}^{1}/_{2}\,O_2\ (g) \tag{2.2}$$

while the photoexcited conduction band electrons, transported to the counter-electrode (cathode) of the PEC cell, reduce water to form hydrogen gas [7].

$$2H_2O\ (l) + 2e^{-} \rightarrow 2OH^{-}(aq.) + H_2\ (g) \tag{2.3}$$

The key requirements for a semiconductor photoelectrode are mainly efficient absorption of visible light and good charge transport [13]. As shown in Figure 2.1, the solar-to-hydrogen efficiency of a semiconductor can be influenced by the light absorption (1), the charge transport (2 and 4) and the reaction kinetics (3 and 5). The latter parameter can be modified by adding a catalyst on the surface. The other parameters are intrinsic properties of the material [12].

Semiconductors' ability of absorbing light is determined by the bandgap (E_g), separating the valence and the conduction bands; only electromagnetic waves with wavelengths lower than E_g can be collected by promoting an electron between two bands. The valence band is filled with electrons (at 0 K and standard conditions) and the conduction band corresponds to the first excited level above the gap (empty at 0 K). The difference between the bottom of the conduction band (E_C) and the top of the valence band (E_V) defines the bandgap, while the Fermi

level (E_F) describes the distribution of electrons and holes over all the available energy levels in a solid. In a band structure picture, the Fermi level can be understood as a hypothetical energy level of an electron, such that at thermodynamic equilibrium this energy level would have a 50% probability of being occupied at any given time. The Fermi level position distinguishes different class of materials. Thus, in metals and semimetals E_F lies inside at least one band. In insulators and semiconductors E_F is inside a band gap, however in semiconductors the bands are near enough to the E_F to be thermally populated with electrons or holes. The two latter types of materials are differentiated by the bandgap energy (1 to 4 eV for semiconductors – Figure 2.2 - and E_g > 4 eV for insulators) [12-14].

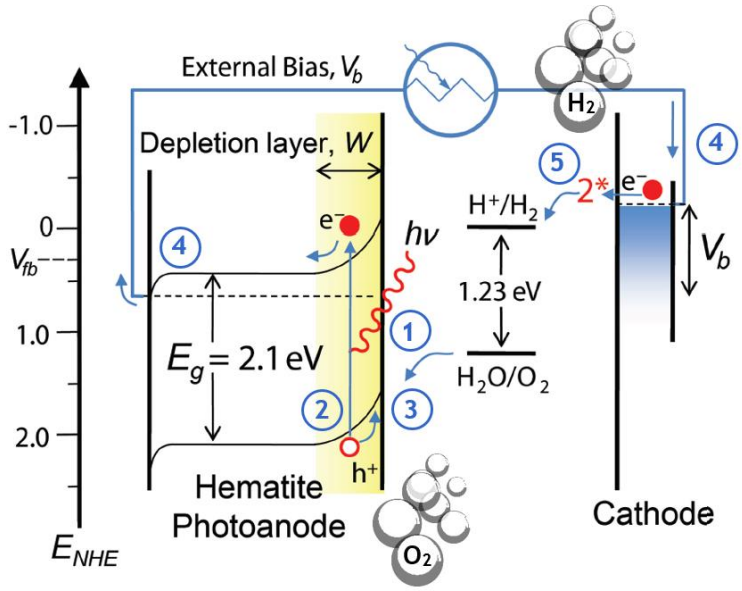

Figure 2.1 *- Schematic representation of the relevant processes involved in the photo-oxidation of water using a n-type semiconductor as a photoanode; (1) - absorption of a photon, generating an electron-hole pair in the material; (2) diffusion of holes towards the interface with electrolyte where water oxidation takes place (3); (4) - transport of electrons through the semiconductor and the external circuit; (5) water reduction at the metallic cathode surface. Adapted from* [12].

When the semiconductor is in contact with an electrolyte with redox energy (E_{Redox}) different from E_F, equilibrium of the electrochemical potential in the two components is achieved by electron exchange at the interface. On one side, the electrons are transferred to the electrolyte and are depleted in a certain thickness of the material (space charge layer). Therefore, Fermi levels are adjusted due to the formation of an electric double layer between the solid and the electrolyte. The depletion of electrons at the surface of the semiconductor will induce an electric field between the bulk of the semiconductor and its surface, corresponding to bending of the valence and conduction bands [12, 13].

For a given semiconductor and electrolyte, there exists a unique potential for which the potential drop between the surface and the bulk is zero and there is no space charge layer – the flatband potential. For a certain redox couple, the flatband potential (V_{fb}) corresponds to

particular redox potential of the electrolyte when there is no excess charge in the semiconductor and consequently no band bending. When a positive difference of potential is applied ($V_{applied}$) between the n-type semiconductor and a reference electrode the band bending of the semiconductor is modified [12]. Illumination can modify the band bending of a semiconductor in equilibrium with an electrolyte as the electron and hole densities are increased due to light absorption [12, 13].

This band model does not clearly consider bulk traps or surface states (due to dangling bonds or adsorbed species on the surface). The bulk traps act as recombination centres between photogenerated charges and will decrease the efficiency of charge separation. The surface states can act as donor or acceptor species and will influence the electrochemical and photoelectrochemical properties of a semiconductor (surface recombination) [12].

Semiconductors for practical applications are often doped, mainly with the intention to improve the conductivity. In metal oxide photoelectrodes, shallow donors and acceptors are almost always required because of the low intrinsic charge carrier mobilities. Certain dopants can improve the optical absorption of wide bandgap semiconductors, increase the minority carrier diffusion length or enhance the catalytic activity at the surface of the semiconductor. Other dopants can unfavourably affect the semiconductor proprieties by creating the effects mentioned above (bulk traps or surface recombination) [13].

Currently, water splitting PEC devices achieve very low conversion efficiencies since most of the semiconductors used for this application have a large energy bandgap. The band edge potentials of many semiconductors are not suitable for oxygen and hydrogen evolution and the water splitting reaction cannot take place. Consequently an additional bias voltage is required to promote the reduction reaction [7]. When the bias potential is applied with respect to a reference electrode, the potential difference will be distributed over the space charge layer and the Helmholtz layer (which consists of a continuous layer of anions that is formed in the electrolyte to balance the positive surface of the semiconductor) [13]. Thus, one of the key aspects concerning the choice of a semiconductor material is related to its band edge positions, which determine the maximum reduction and oxidation potentials of the photogenerated electrons and holes in it [13].

First of all, the material must be water stable. The photostability of a material depends on the relative position of the band edges, the Fermi level of electrons (in dark) and the quasi Fermi Level of electrons and holes (under illumination) compared to the cathodic and anodic decomposition potentials. The inadequate positions of these bands lead some materials to readily corrode in water. The material should absorb a large portion of the solar spectrum and its bandgap should be as small as possible. However, the energy difference between the oxidizing hole and the reducing electron should be higher than the water dissociation electrochemical potential (1.23 eV) [12, 14]. Consequently a bandgap of 1.6 – 2.0 eV is

considered to be the best compromise for the water splitting reaction (Figure 2.2). The position of the energetic bands must also be taken into account, as the valence band shall be below the redox potential of O_2 formation and the conduction band shall be above the redox potential of H_2 formation [12]. The band positions of most metal oxides show the same pH dependence as the water reduction and oxidation potentials, so relative positions remain the same at other pH values [13].

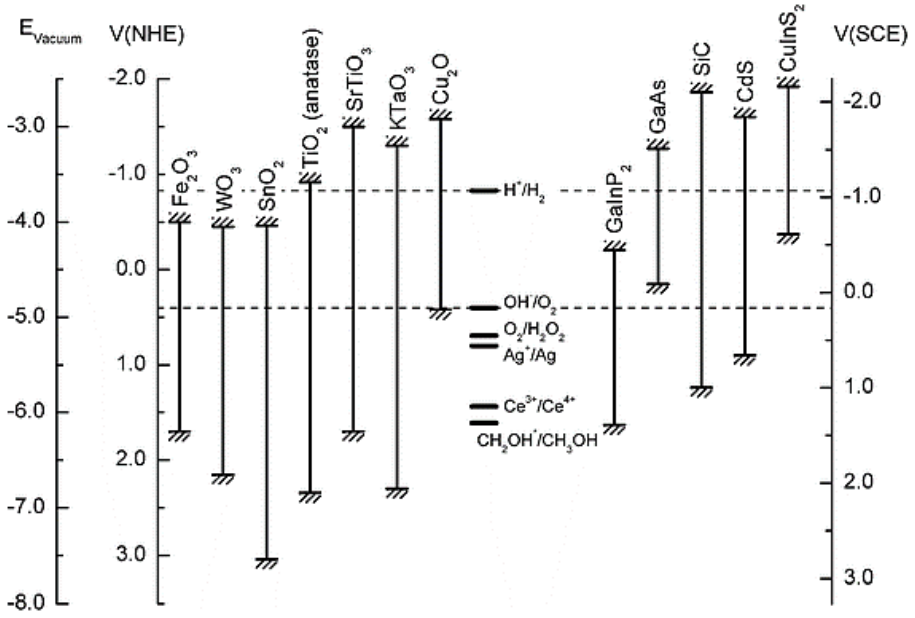

***Figure 2.2** – Band edge positions for some semiconductors at pH 14 and some important redox potentials* [13].

The first material recognized to split water under UV light was TiO_2, reported by Fujishima and Honda in 1971 [10, 15]. Since then, many research efforts have been made to find a suitable material for preparing efficient photoelectrodes. During the last decades, different types of semiconductors were studied [10, 15]. Metal oxides, such as WO_3 and Fe_2O_3, are considered very promising as their spectral sensitivity reaches further into the visible spectrum with bandgaps of 2.6 and 2.0 eV, respectively (Figure 2.2). Their abundance and chemical stability in water allow their use in industrial applications. As a drawback, these semiconductors have a conduction band edge at an energy level inferior than the reversible hydrogen potential. Thus, a choice for these materials is accompanied with the need of an electrical bias for hydrogen evolution [12, 14]. Good visible light absorption, high chemical stability, band edge positions that straddle the water reduction and oxidation potentials, efficient charge transport, low overpotentials for reduction/oxidation of water and low cost are important factors that determine the semiconductor performance in water splitting [13].

2.2 HEMATITE: A PROMISING MATERIAL FOR WATER-SPLITTING

Iron is the fourth most common element in the earth's crust (6.3 wt.%) and because iron is readily oxidized in air to the ferrous (+2) and ferric (+3) states, iron oxide is very abundant [16]; hematite (α-Fe_2O_3) is the most common crystalline structure of iron oxide [15].

The first study on the hematite ability for water photolysis was made in 1976 by Hardee and Bard [17]. They found out that hematite was both stable under anodic polarization and capable of absorbing light with wavelengths longer than 400 nm. In this study thin films of Fe_2O_3 were produced on Ti and Pt substrates by chemical vapour deposition (CVD) of $Fe(AcAc)_3$. Then, it was observed a 700 $\mu A \cdot cm^{-2}$ current density generated from their electrodes under illumination of 500 nm light at a potential of 0.8 V vs. SCE in 0.5 M KCl as electrolyte. It was concluded that hematite was truly a promising material for water splitting, but its flatband potential was not enough to reduce water and so an external bias had to be applied to accomplish water splitting [15, 16]. In the past few decades numerous studies have been made on hematite photoelectrodes, mainly on controlling the hematite films morphology and on searching more efficient doping materials. Presently, the main ongoing studies are focused on two key aspects: (1) reduction of the overpotential required by employing various surface treatments; (2) optimization of the electrode morphology, which can significantly increase the water splitting photocurrent density (Figure 2.3) [16].

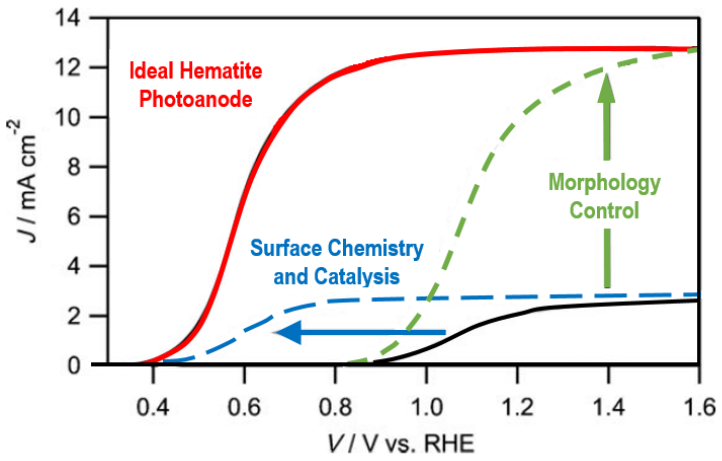

Figure 2.3 *- The two-part strategy to obtain the ideal hematite photoanode (red line): increase the photocurrent density by controlling the hematite morphology (green line) and reduce the overpotential required to start the water splitting reaction by surface treatments engineering (blue line) [16].*

2.2.1 OVERPOTENTIAL REDUCTION ON HEMATITE PHOTOANODES

Based on the V_{fb} usually reported for hematite, an external bias of only 0.3–0.4 V_{RHE} should be necessary to initiate the water splitting reaction. However, the onset potential is typically not observed until 0.8–1.0 V_{RHE}. The remaining overpotential of ca. 0.5–0.6 V is a major drawback for the implementation of hematite photoelectrodes for solar hydrogen production and it has been attributed to two distinct surface properties. Firstly, there is evidence that mid-bandgap energy states resulting from both oxygen vacancies and crystalline disorder can trap holes at the surface. Secondly, the oxygen evolution reaction (OER) kinetics is sluggish [16]. To overcome this limitation, various catalysts have been tested on the surface of hematite photoanodes and the best performing catalyst material reported for OER was IrO_2 [15, 16]. However, even if a very efficient OER catalyst is used, the surface trapping states still plays an important role contributing with a significant overpotential (0.3–0.4 V). It was recently reported that surface trapping states can be passivated by using extremely thin Al_2O_3 overlayers made by atomic layer deposition (ALD), responsible for reducing the overpotential in 100 mV for nanostructured photoanodes. This corresponds to an enhanced photocurrent by a factor of 3.5 (from 0.24 $mA \cdot cm^{-2}$ to 0.85 $mA \cdot cm^{-2}$) at +1.0 V_{RHE} under standard illumination conditions. The subsequent addition of Co^{2+} ions as co-catalyst further decreased the overpotential and leaded to a record photocurrent density of 0.42 $mA \cdot cm^{-2}$ at 0.9 V_{RHE} [18].

2.2.2 HEMATITE MORPHOLOGY CONTROL TECHNIQUES

The control of hematite morphology allows improving the photocurrent plateau and different tools to control the dimensions and morphology of hematite materials at the nanometer length scale have been explored [15].

One technique that allows obtaining porous thin hematite films with good morphology consists of coating a dispersion of nanoparticles and a porogen onto a conductive substrate. By changing the concentration and the oxidative environment during nucleation and growth steps, the hematite morphology control can be done. Drying and then heating these films in air burns away the porogen and sinters the remaining oxide. Thus, a porous structure of interconnected particles can be formed [15]. This concept was first attempted with hematite in 1994 [19]. It was observed that hematite micrometer-thick porous films have good adhesion to the substrate and a particle size in the 25–75 nm range. However, the efficiency of these photoanodes towards water splitting was quite low. It was concluded that charge carrier recombination was the critical factor controlling the photocurrent. The cause of the excessive recombination and poor performance was attributed to a higher quantum efficiency of similar particles dispersed in the electrolyte. This limitation was later addressed by modifying the film thickness to optimize the light absorption vs. carrier transport issue, but no significant improvements were

obtained [16]. However, high water splitting photocurrents can be obtained after successfully incorporating dopants at sufficient concentration. In a study done by Sivula *et al.* [20] under standard illumination conditions (AM 1.5G 100 $mW \cdot cm^{-2}$), a photocurrent of 0.56 $mA \cdot cm^{-2}$ at 1.23 V_{RHE} was obtained and over 1.0 $mA \cdot cm^{-2}$ before the onset of dark current (1.55 V_{RHE}). A high sintering temperature of 800 ºC was found to be necessary to afford photoactivity and the feature size increased from the original 5–10 nm to more than 50 nm. To overcome this feature size limitation, a method to independently control feature size and functionality with nanostructured oxide electrodes using an encapsulation approach was then developed. The photocurrent of the encapsulated electrode reached 1.86 $mA \cdot cm^{-2}$ at 1.43 V_{RHE} with a maximum photocurrent of 2.34 $mA \cdot cm^{-2}$ before the onset of the dark current, while the control electrode gave only a maximum of 1.5 $mA \cdot cm^{-2}$. It can be concluded that the temperatures required to sinter and to make these films active result in particles size too large for getting high photocurrents [15, 16]. In a recent study from Zong *et al.* [21] a low-cost and facile colloidal electrophoretic deposition approach was developed for scalable fabrication of α-Fe_2O_3 films. Large-sized uniform films (*e.g.* 80 mm × 70 mm) with tailored thickness and nanostructures were prepared on conductive glass substrates and a photocurrent of 1.1 $mA \cdot cm^{-2}$ at 1.23 V_{RHE} under standard illumination was achieved. This is among the highest reported values achieved for hematite films prepared using other complex colloidal approaches.

An alternative way to produce hematite photoelectrodes is to use nanosized rod or wire arrays, which can overcome the grain boundaries created from the colloidal approach. A facile method to produce hematite nanowires is by the simple thermal oxidation of iron foils. Due to the increased volume of the oxide over the metal, when foils of iron are thermally oxidized under the right conditions, arrays of Fe_2O_3 nanowires spontaneously grow from the surface of the foil. With diameters of 20–40 nm and lengths of up to 5 mm these nanowire arrays lead to larger surface areas, sufficient light absorption and a direct path for the conduction of electrons to the substrate. Defects present in nanowires prepared by this method and the presence of suboxides near the interface of the substrate are usually pointed out as major disadvantages since they greatly enhance the recombination [15, 22, 23]. Another simple method to create hematite arrays on a variety of substrates via a metastable akaganeite is from the controlled precipitation of Fe^{3+} ions in aqueous solution. However, it was found that bulk or surface defects were the major factors limiting the hematite performance prepared by this route since residual hydroxyl groups or vacancies were likely to blame [15]. More recently, a method to prepare hematite nanorod arrays using an anodic aluminium oxide (AAO) template was reported [24]. The result was a 10 μm thick rod array that showed water oxidation photocurrent densities of about 1 $mA \cdot cm^{-2}$ at a potential of 1.5 V_{RHE} under AM 1.5 illumination. Still, no defined photocurrent plateau was observed [16, 24]. In a more recent study, hematite nanorods were grown on a FTO substrate by a hydrothermal method in the presence on Mn; a photocurrent

density of 1.6 mA·cm^{-2} at 1.23 V_{RHE} and a plateau photocurrent density of 3.2 mA·cm^{-2} at 1.8 V_{RHE} in a 1 M NaOH electrolyte solution (pH 13.6) were achieved. The increase in the photocurrent density, and thus in the oxygen evolving capacity, was attributed to the increased donor density resulting from Mn doping of the Fe_2O_3 nanorods [25]. In another very interesting study, a new PEC device structure was developed to create ultrathin hematite films deposited on a 3D nanophotonic structures. A current density of 3.05 mA·cm^{-2} at 1.23 V_{RHE} has been achieved on such nanophotonic structure, which was about three times more than the one for planar photoelectrodes [26].

A third route to produce hematite photoelectrodes is based on nanostructuring techniques using potentiostatic anodization. Prakasam *et al*. first showed that iron foils could be nanostructured using anodization in a glycerol-based electrolyte [27]. Ordered nanopores were observed with pore size ranging from 20 to 250 nm and depths up to 600 nm depending on the anodization voltage and time. Under simulated solar illumination these photoanodes produced a photocurrent of 0.05 mA·cm^{-2} at 0.4 V_{SCE} in 1 M NaOH (1.45 V_{RHE}). Another work by the same group reported 1.1 mA·cm^{-2} at 1.4 V_{RHE} in 1 M NaOH [28]. The authors attributed the high photocurrent to the double layered structure which includes both a large surface area for water oxidation and a vertically orientated nanotube array for electron transport. McFarland and co-workers reported a method to deposit iron hydroxides from $FeCl_3$ solutions under cathodic polarization [29]. The subsequent annealing at high temperature (700 ºC) then resulted in porous hematite films. This method readily allowed for the incorporation of dopants which were found to have an effect on the morphology of the sintered electrodes. However, the generally observed large particle size obtained with this technique remains a limitation to higher photocurrent densities [16]. A hematite photoanode showing to be stable and producing a record-breaking performance of 4.32 mA·cm^{-2} photoelectrochemical water oxidation current at 1.23 V_{RHE} was recently reported. This photocurrent corresponds to 34 % of the maximum theoretical limit expected for hematite with a bandgap of 2.1 V. The hematite single-crystalline "wormlike" morphology was produced by *in-situ* two-step annealing probes at 550 °C and 800 °C of ß-FeOOH nanorods that grew directly on a transparent conducting oxide glass via an all-solution method. In addition, this structure was modified by platinum doping to improve the charge transfer of hematite and an oxygen-evolving co-catalyst on the surface [30].

A quite more complex but very promising technology has been studied in the last few years, the atmospheric pressure chemical vapour deposition (APCVD). In 2006 Kay *et al*. reported APCVD films optimized with cauliflower-type structures having a feature size of 5–10 nm that grew on FTO substrates at a rate of about 100 nm·min^{-1} [31]. The best film produced a photocurrent density of 1.8 mA·cm^{-2} at 1.23 V_{RHE} under standard illumination in 1 M NaOH and was further increased to 2.2 mA·cm^{-2} by treating the surface with Co^{2+} ions [16]. Higher temperatures were found to decrease the deposition rate, leading to a larger particle size and

reducing the photocurrent density [31]. An important parameter governing the structure and quality of nanostructures prepared by particle-assisted CVD systems is the particle to precursor ratio [32]. By changing the carrier gas flow rate, keeping the same concentration of iron precursor, and re-optimizing the other experimental parameters, the amount of time the precursors resided in the critical region of particle nucleation and growth above the deposition substrate was effectively tuned. It was found that using a carrier gas flow rate three times higher than the previous result enhanced the preferential orientation of the basal planes normal to the substrate. This resulted in an optimized thickness and photocurrents above 3 $mA \cdot cm^{-2}$ [33]. In general, APCVD results demonstrated that water oxidizing photocurrents over 3 $mA \cdot cm^{-2}$ at relatively low bias potentials are possible. While this is a considerable step towards high performance hematite, the photocurrent density remains far from the 12.6 $mA \cdot cm^{-2}$ value possible for cauliflower-type morphology due to the fact of thick stems increase the number of photons absorbed far from the semiconductor-liquid junction (SCLJ) [15, 16].

To improve the results obtained by applying APCVD technique a new concept was then demonstrated, which used a nanostructured material as the host scaffold [15]. By coating the scaffold with a thin layer of Fe_2O_3 by APCVD, a 20 % increase in the photocurrent was expected to be observed over control samples prepared on flat FTO substrates. However, the 60 nm thickness optimized layer of hematite was too thick. Attempts to use thinner films of hematite resulted in poor performances and pointed to a high recombination of photogenerated holes at the hematite/scaffold interface [34]. This limitation was addressed by including a SnO_2 or a SiO_x buffer layer. When a SiO_x buffer layer was deposited on the FTO, reasonable photocurrents were obtained with only a 12.5 nm thickness of Fe_2O_3. Films with the buffer layer and with similar thickness to the ones without the buffer layer showed less recombination upon examining photocurrent transient behaviour. Unfortunately, the best ultrathin hematite film employing a buffer layer showed slightly lower values when compared to APCVD films. This was possibly due to the high reflectivity of the compact and flat films. [15, 16].

As shown so far, there are many technologies that enable changing and controlling the morphology of hematite. Surely there are even more innovative technologies that have not been properly studied yet, which represents a great scope for the study and optimization of the hematite morphology control. However, there are two major problems associated with all these techniques: (1) they are quite complex and the reproducibility of samples with good results is very difficult to obtain; (2) these technologies require very detailed knowledge of its operation principles and many of them are associated to high costs for producing samples. Though, there is a technology that allows high reproducibility of stable samples, easy operation steps and does not require the use of very expensive equipment: spray pyrolysis. This technique can consistently produce electrodes with high performance and basically consists of a Fe^{3+} aqueous or ethanolic solution that is simply sprayed onto a heated substrate. To assess if

hematite samples produced by spray pyrolysis in this study have a promising and acceptable efficiency, a literature review was done to obtain the record values for the current densities achieved for samples produced by the different technologies that were discussed above. These results are shown in Table 2.1.

***Table 2.1** - Record values of the current densities achieved for hematite samples produced by different deposition techniques.*

Morphology Control Technique	Dopant	Catalyst	Current Density (*I-V* curve)	Simulated Sunlight	References
Spray Pyrolysis	–	–	< 0.5 mA·cm^{-2} at 1.45 V_{RHE}, with some dark current	130 mW·cm^{-2}	Duret, J. Phys. Chem B 2005, 109 [35]
Spray Pyrolysis	Si (TEOS)	–	0.72 mA·cm^{-2} at 1.45 V_{RHE}	100 mW·cm^{-2}	Formal, Adv. Funct. Mater. 2010, 20 [36]
Ultrasonic Spray Pyrolysis	Si (TEOS)	–	< 1.2 mA·cm^{-2} at 1.45 V_{RHE}	100 mW·cm^{-2}	Cesar, JACS 2006 [31]
Ultrasonic Spray Pyrolysis	–	–	> 2.1 mA·cm^{-2} at 1.45 V_{RHE}, with some dark current	130 mW·cm^{-2}	Duret, J. Phys. Chem B 2005, 109 [35]
Colloidal Electrophoretic Deposition	–	–	1.1 mA·cm^{-2} at 1.23 V_{RHE}	100 mW·cm^{-2}	Zong *et al.* [21]
3D nanophotonic structure	–	AAO	3.05 mA·cm^{-2} at 1.23 V_{RHE}	100 mW·cm^{-2}	Qiu, Y., *et al.*, 2014 [26]
Electrodeposition	Ti	–	1.5 mA·cm^{-2} at 1.45 V_{RHE}	100 mW·cm^{-2}	Hu, ChemComm 2009 [37]
APCVD	–	Al_2O_3 and Co^{2+} treatment	0.42 mA·cm^{-2} at 0.9 V_{RHE}	100 mW·cm^{-2}	Formal, Chem. Sci., 2011, 2 [18]
APCVD	Si (TEOS)	–	< 1.8 mA·cm^{-2} at 1.45 V_{RHE}	100 mW·cm^{-2}	Cesar, JACS 2007 [14]
APCVD	Si (TEOS)	Co	2.3 mA·cm^{-2} at 1.23 V_{RHE}	100 mW·cm^{-2}	Kay, JACS 2007 [38]
APCVD	Si (TEOS)	IrO_2 nanoparticules	~3 mA·cm^{-2} at 1.23 V_{RHE}	100 mW·cm^{-2}	Tilley, Angew. Chem. Int. Ed.2010, 49 [39]
Solution-processed porous hematite	Ti	–	2.34 mA·cm^{-2} at 1.45 V_{RHE}	100 mW·cm^{-2}	Brillet, Nano Letters 2010 [40]
Hydrothermal method	Ti	–	3 mA·cm^{-2} at 1.45 V_{RHE}	100 mW·cm^{-2}	Deng, Appl Phys 2012, 112 [41]
Solution-based method	Pt	Co-Pi	4.32 mA·cm^{-2} at 1.23 V_{RHE}	100 mW·cm^{-2}	Kim, Scientific Reports 2013 [30]

2.3 PHOTOELECTROCHEMICAL MEASUREMENTS

A PEC cell basically consists of a reservoir that contains the electrolyte, the photoactive material (working electrode – WE), the counter electrode (CE) and the reference electrode (RE). It has to have an optically transparent window for allowing the sample to be illuminated and facilities to electrically connect the electrodes to the external system (Figure 2.4)[42].

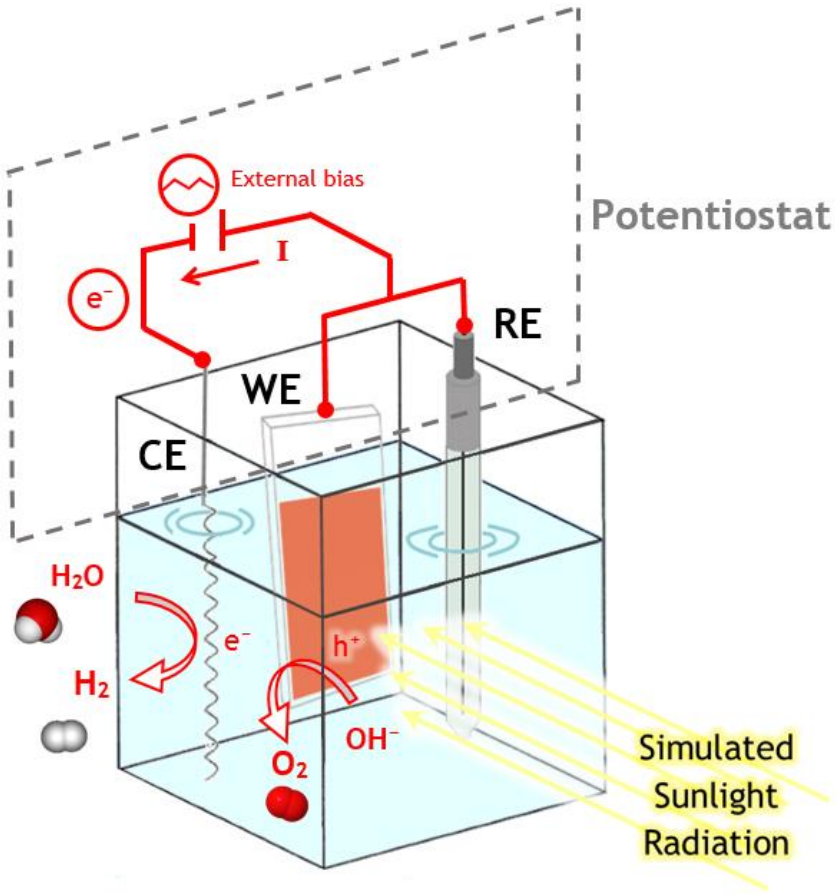

***Figure 2.4** - Example of a 3-electrode configuration PEC cell for water splitting.*

The photoresponse is conventionally measured under standard conditions: 1 sun illumination (1000 $W \cdot m^{-2}$), 25 ºC and AM1.5G [12, 14, 42]. The main aspect that distinguishes the PEC cell design from a standard electrochemical cell is the presence of an optically transparent window through which the sample can be illuminated. The optically transparent window material is very important as it should have a transmittance higher than 90 % from 250 nm (*e.g.* a quartz window) [10]. The PEC cell design must ensure that the illuminated area corresponds to an area that is completely immersed in the electrolyte [42].

Photoelectrochemical measurements on thin films require an optically transparent and conducting substrate as a back-contact. This substrate should form an Ohmic contact with the photoactive material to ensure uninhibited current flow. In most cases for n-type photoanodes this substrate is a glass doped with transparent conducting oxides (TCOs) by sputtering. The most common TCO used is FTO (fluorine doped tin oxide) due to its commercial availability, high carrier concentration and mobility and an optical transparency higher than 80 % [42].

In electrochemical cells the electrolyte consists of a solvent with active species to be reduced or oxidized, depending if it is an alkaline or an acidic media. Photoactive semiconductor materials immersed in a redox electrolyte are greatly affected by the solution properties, redox level and stability, interfacial kinetics (adsorption), viscosity, conductivity, ionic activity and transparency within the crucial wavelength region [10]. As mentioned, the

choice of a suitable electrolyte solution is very important, mainly in what concerns the redox couple selection. It should contribute to improved charge-transfer kinetics, stability, as well as help preventing undesirable phenomena such as surface recombination and trapping. Also, the electrolyte concentration should be sufficiently high to avoid large ohmic voltage losses (concentrations of at least 0.5 M are recommended) [10, 42].

The reaction at the counter-electrode should be as fast as possible and should have a high catalytic activity in order to prevent performance limitations. Usually, platinum is used as counter-electrode; this material presents good stability over a wide range of electrolytes and pH, as well as it shows low overpotentials for hydrogen evolution (~0.1 V). To avoid inhomogeneous current densities at the working electrode, the counter-electrode should face it symmetrically. Moreover, the counter-electrode surface area should be twice larger than the photoelectrode area.[42]

The 3-electrode configuration allows measuring the applied potential with respect to a fixed reference electrode, allowing turning visible the independent response of the working electrode to any change in the applied potential. In water splitting studies the applied potential is reported against RHE (Reversible Hydrogen Electrode), thus the potential measured with the Ag/AgCl electrode must be converted into RHE scale using the following expression [42]:

$$E_{RHE} = E_{Ag/AgCl} + E^{0}_{Ag/AgCl\ vs.\ SHE} + 0.059 \times pH \qquad (2.4)$$

Current-voltage measurements are the most important technique to determine the performance characteristics of photoelectrodes for water splitting. These measurements allow obtaining the photocurrent density and energy conversion efficiency as a function of applied potential, the dark current as a function of the applied potential, the onset potential, electron vs. hole transport limitations and transient effects that indicate recombination. For a hematite photoanode the dark current is expected to start for potentials of approximately 1.7 V_{RHE}, which indicates that the electrochemical oxidation of water is occurring at the semiconductor surface. Conventionally the onset potential is expected to start at approximately 0.95 V_{RHE}. This happens as a result of the free holes in the valence band concentration increase as the Fermi level is pulled down and starts to approach the valence band in the region near the surface. This value is much more positive than the flatband of hematite, which is around 0.3 V_{RHE}. The difference is due to slow oxidation kinetics and/or to recombination in the space charge region [10, 12, 14, 42].

3 TECHNICAL DESCRIPTION AND PROCEDURES

3.1 PRODUCTION OF MATERIALS FOR HEMATITE PHOTOANODES

3.1.1 SPRAY PYROLYSIS TECHNIQUE

There are many techniques to nanostructure hematite, such as the colloidal, nanowire and anodization approaches, which have been briefly described within Chapter 2. However, a simple spray pyrolysis technique allows producing electrodes with high performance [15, 16]. This technique consists of a Fe^{3+} aqueous or ethanolic solution that is sprayed onto a hot substrate (400–500 ºC) and photocurrent densities in the 0.5–1.0 $mA \cdot cm^{-2}$ range are typically obtained under simulated solar illumination. It is known that good photoactivities can be obtained with this method, even without adding dopants to increase the conductivity of α-Fe_2O_3. This technique generally produces compact films (not porous) and the surface area limits the produced photocurrent under standard illumination conditions. However, the ease and reproducibility of this technique is a very important advantage and so it has led to valuable fundamental studies on adding dopants to the precursor solutions [12, 15, 16].

3.1.2 EXPERIMENTAL SETUP ASSEMBLY

An important goal of this work was to assemble and optimize an experimental facility that allows the deposition of bare hematite films, as well as performing pre-treatment of samples with TEOS (Tetraethyl orthosilicate) and doping with different materials. This part of the work has particular importance because this was the first time that materials deposited by spray-pyrolysis were made in the host laboratory. The accuracy of the experimental setup assembly and its optimization will be crucial for any future works that may be carried out in this theme.

For making a correct material deposition and thus obtain uniform films it was extremely important to ensure that glass substrates were placed in a central position towards the spray nozzle and also ensure that the spray was composed of fine droplets with a uniform size distribution. The spray nozzle was therefore either adjustable in height or laterally along an axis of rotation corresponding to the support where it was placed (Figure 3.1). The placement of the glass substrates in a central position on the heating plate was made using a laser pointer placed near the spray nozzle.

The solution feeding to the spray nozzle was initially made with a HPLC pump. In this configuration the solution was sucked from a closed bottle with a constant flow rate of 10 $ml \cdot s^{-1}$. After some deposition tests it was decided to replace the HPLC pump by other equipment, since the solution suction was often interrupted by the formation of air bubbles

and by accumulation of particles inside the tubes (which easily clogged due to their very small diameter). It was used a stainless steel pressurized tank to replace the HPLC pump (Figure 3.1).

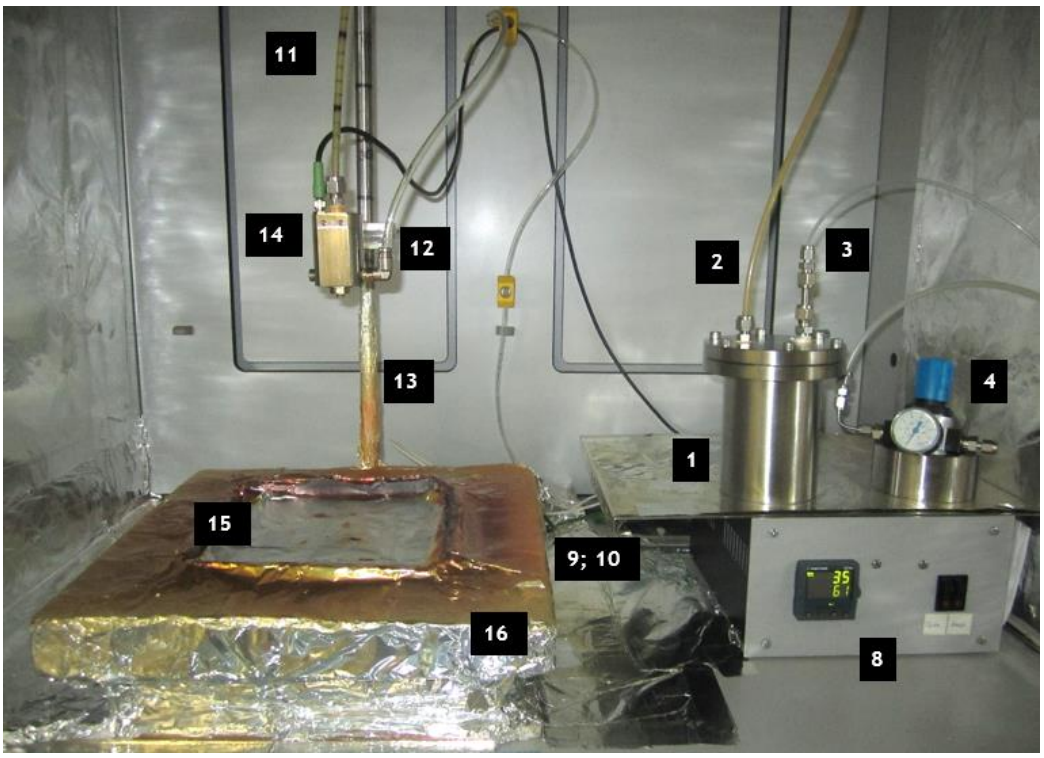

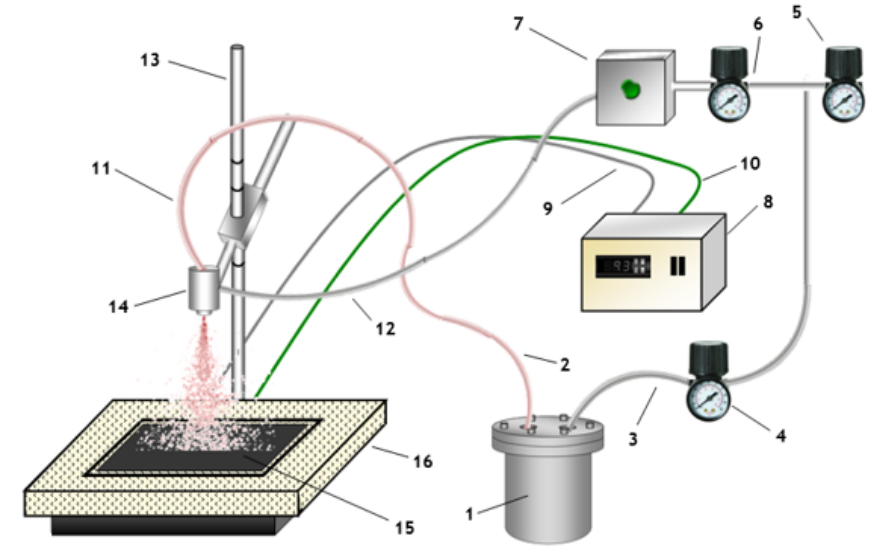

1 - Pressurized solution tank
2 - Pressurized solution output
3 - Pressurized nitrogen inlet
4 - Nitrogen pressure reducer gauge (0,5 to 1,0 bar)
5 - Network nitrogen pressure gauge (6 bar)
6 - Nitrogen pressure reducer gauge (1,0 bar)
7 - Spray control box
8 - Temperature control box
9 - Cables of the heating resistors
10 - Thermocouple cable
11 - Spray solution feed
12 - Spray nitrogen feed
13 - Calibrated vertical support (20, 25,..., 40 cm)
14 - Spray nozzle
15 - Heating plate painted with black ceramic paint
16 - Ceramic insulation board

Figure 3.1 *- Photograph and schematic representation of the different components that are part of the experimental setup for material depositions.*

The volume of iron (III) acetylacetonate solution was previously measured before being added to the tank. The pressurization of the tank was done by using pressurized nitrogen from the laboratory pipeline. The pressure inside the tank was always maintained at 1 bar and it was controlled by a pressure reducer gauge. Thus, continuous solution re-feeding to the spray nozzle was always ensured by the pressure of the gas which forced the solution to flow out of the tank to replenish the equilibrium pressure of 1 bar after each spray (Figure 3.2 a). In order to control the volume of solution deposited in each spray it was used a partially transparent tube to feed the spray nozzle that allowed seeing the solution level inside. This tube was marked with lines with different sizes to distinguish fractions of 0.1 ml and 0.5 ml (Figure 3.2 b).

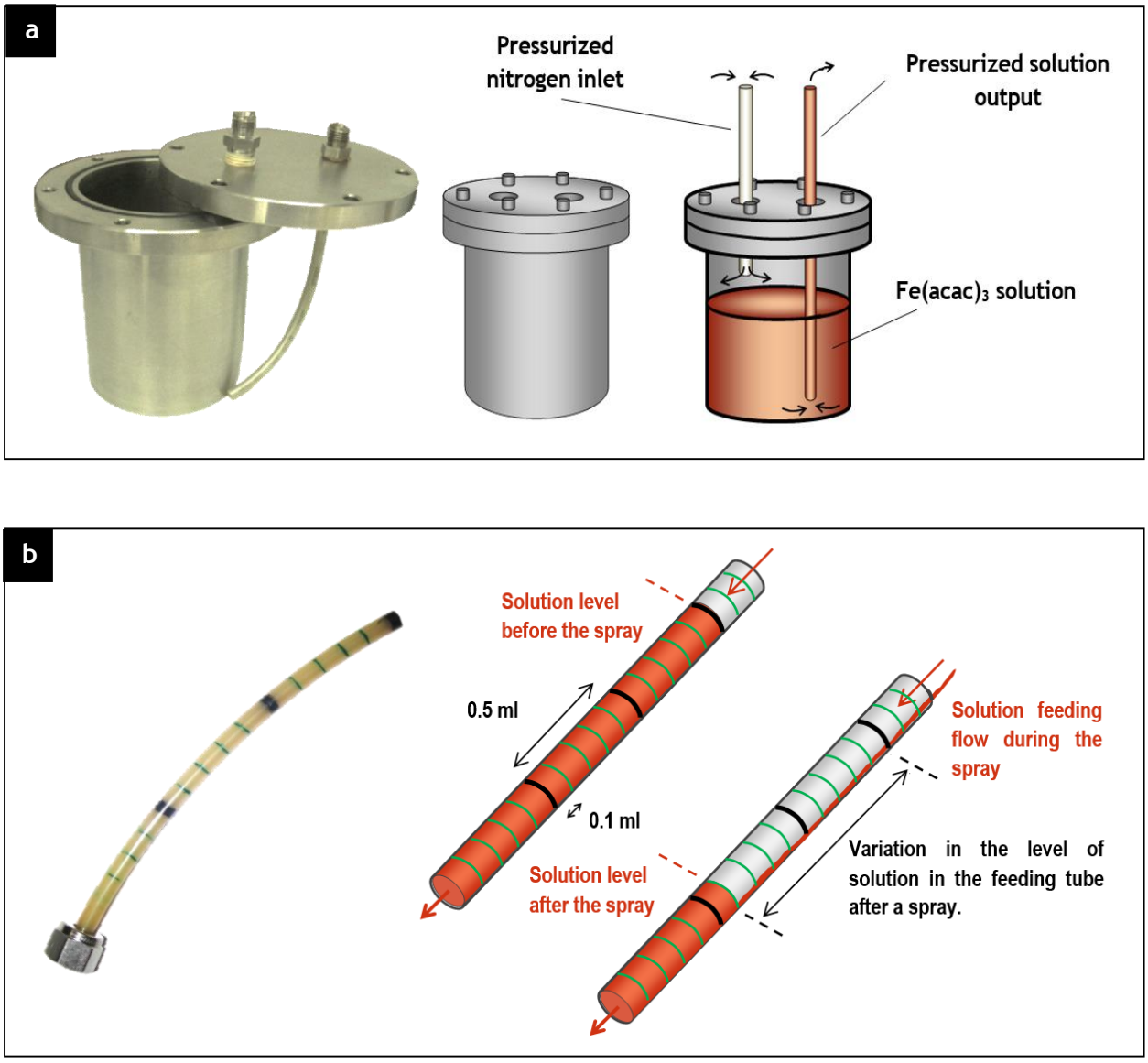

Figure 3.2 *- Schemes of the experimental setup components that are part of the pressurized solution feed configuration; a) Pressurized solution tank; b) Methodology for controlling the solution volume of each spray using the tube marked with different volume fractions.*

The deposition time was controlled with a chronometer. After each deposition the volume of solution that remained in the tank was always measured to ensure that the desired volume of solution was correctly deposited.

The spraying was done using a manual control where the nozzle feeding gas was maintained slightly above 1 bar pressure. It was important to ensure that the gas pressure in the nozzle was not much higher than the solution pressure from the tank, since that would create a gas barrier that would not allow passage of solution to the spray nozzle.

According to some studies [10, 12, 14-16, 43] hematite deposition should be carried out in a heated substrate to at least 400 °C to achieve good morphology and then heated to at least 450 °C for samples annealing. To achieve this range of temperature values a heating plate with four thermal resistors was used. These resistors were connected to a manual temperature controller and the monitoring was made by using a thermocouple installed in the base of the heating plate, allowing real-time measurements. The surface of the heating plate was painted with a black ceramic paint resistant to high temperature, allowing a temperature distribution as much uniform as possible. The heating plate was side protected with a ceramic material to ensure adequate thermal insulation. The temperature of the heating plate was measured for different heating surfaces where the glass substrates were placed on. The results of this study are presented in Appendix A. It was concluded that the best heating surface was an aluminium foil, being also the only surface that allowed reaching the desired temperature range. To find out the temperature distribution of the hot plate and the maximum temperature reached on its surface, a temperature study with SolidWorks Software in the heating plate was also done [44]. The predicted maximum temperature that could be reached by the thermal resistors was around 500 ºC (Figure 3.3). The temperature distribution uniformity of the hot plate was validated using a thermal imager - Appendix B.

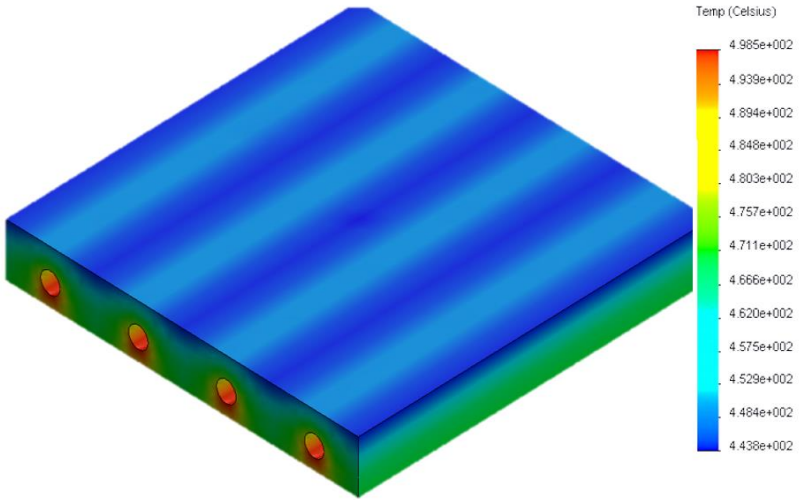

***Figure 3.3** - Results of the SolidWorks thermal study on the heating plate [44].*

3.1.3 FTO GLASS SUBSTRATE FOR Fe_2O_3 PHOTOELECTRODES

The glass substrates were prepared by procedures described elsewhere [10, 12]. Substrates of fluorine-doped tin oxide (FTO) glass 30 × 12 mm^2 were manually cut with a diamond tip glass cutter (Figure 3.4 a) from a glass plate with 30 × 30 cm^2. Then, the glass substrates were ultrasonically washed in an Amsonic device (Figure 3.4 b). The substrates were then disinfected by UV radiation for 15 minutes and stored in sealed plates until use.

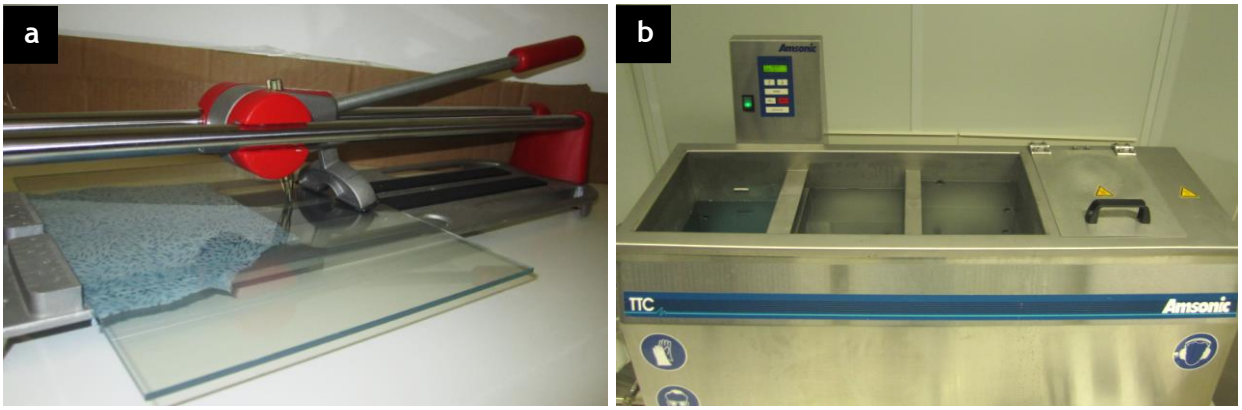

Figure 3.4 *- Equipment used in the preparation of glass substrates; a) Glass cutter with a diamond tip; b) Amsonic used in glass washing;*

3.1.4 DEPOSITION OF MATERIALS AND DOE PLANNING

One of the two-part strategy for improving hematite performance is the morphology control. The spray pyrolysis deposition of α-Fe_2O_3 from an iron (III) acetylacetonate precursor was identified as an appropriate technique for obtaining hematite thin-films because of its ability to give uniform thin-films over large areas with good performance. The crystalline organization affected by the film nucleation and growth is a critical parameter for the photoactivity of thin hematite films. Several studies showed that the morphology and crystallization of hematite is related to the amount of solution deposited, which is reflected in the film thickness, to the substrate temperature, and to the pre-treatment of the substrate [12, 15, 16, 30, 45, 46]. Consequently, taking into account the experimental setup used, the following parameters were controlled in order to allow the study of the photoanodes performance improvement: (1) amount of sprayed solution in each test, which is directly related to the growth of crystals and the film thickness; (2) time gap between sprays, which affects the temperature variations in the substrate; (3) height of the spray nozzle, which determines the shape of the droplets when they reach the substrate, the dispersion of these droplets and thus the uniformity of the film.

Figure 3.5 shows the samples distribution in the heating plate. Three glass substrates of 1.2 cm × 3 cm and one of 2 cm × 3 cm were used for each deposition. Smaller samples were used for the *I-V* characterization tests and the larger samples for the film thickness determination.

For *I-V* measurements the production of three samples under the same conditions ensured reproducible results.

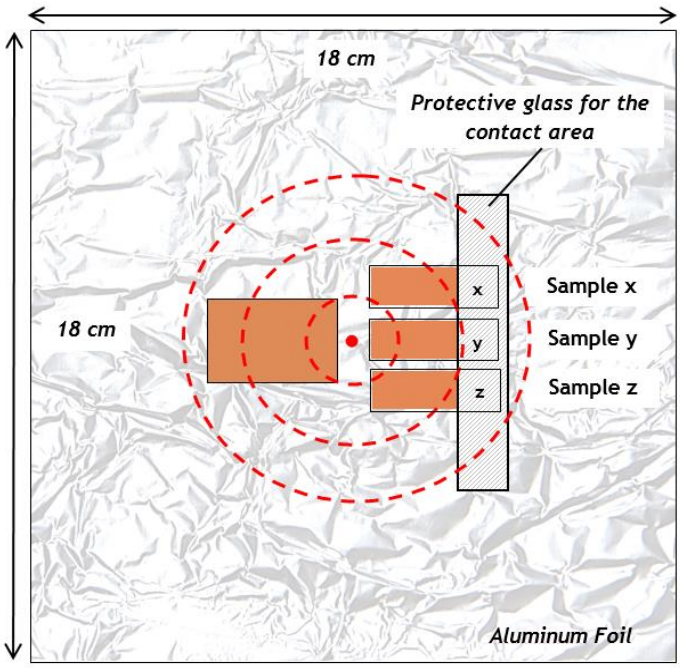

Figure 3.5 *- Arrangement configuration of samples in the heating plate.*

Based on some studies [10, 12, 14-16, 43], a standardized procedure was defined for the preparation of the iron (III) acetylacetonate solution and TEOS pre-treatment. For the hematite depositions, a solution of $Fe(AcAc)_3$ (99.9 %, Aldrich) in ethanol (99.5 %, Aga) was prepared. Then the glass substrates, placed on top an aluminium foil, were sprayed with this solution; three temperatures were tested (400 ºC, 450 ºC and 500 ˚C). After spraying, the samples were maintained at the same deposition temperature for 30 minutes. In what concerns the TEOS pre-treatment, the substrates were first heated to 450 ºC on the heating plate and then approximately 10 ml (per 6 samples, meaning approximately 1.67 ml per sample) of a diluted TEOS solution (10 % volume in ethanol) were hand-sprayed with a glass atomizer onto the hot substrates. These samples were cooled before heating again to deposit the Fe_2O_3.

Initially several preliminary tests were made to study the photoanodes performance for different values of deposited solution, the spray nozzle height and the time interval between sprays. Thanks to these preliminary tests it was possible to reach important conclusions that were crucial to the progress of work. The following assumptions were made: (1) the ideal volume of the solution deposited would be between 45 ml and 95 ml; (2) the ideal height of the spray nozzle would be around 30 cm; (3) the time gap between sprays should be at least 30 seconds; (4) The optimum film thickness should be between 20 and 35 nm.

To determine with the maximum possible accuracy which would be the optimal conditions for the hematite deposition that affect its morphology, a RSM (Response Surface Methodology)

method was used. RSM method exploits the relation between the different operating conditions and their response, thus allowing, together with the factorial design experiments, to diminish the number of experiments to be performed with the maximum relevant information of each experiment [47-49]. In this work the DoE (Design of Experiments) analysis was achieved with a commercially available software - JMP 5.01 (SAS software). Due to the preliminary tests, the upper and lower limits of the defined response variables were identified. Then it was intended to maximize the response variable *j* (current density in $mA \cdot cm^{-2}$), by giving the software the ranges of values for the process variables *v* (volume of solution deposited in ml), *h* (height of the spray nozzle, in cm) and *t* (time between sprays, in seconds). In this work the Central Composite Design model was used. This is a fractional factorial or factorial model that starts with central points and will then estimate new points from the initial central points [47, 48]. In this case, 3 central points were used and the number of replicates remained zero. Except some experiments with adverse conditions the number of replicates should be kept at zero to avoid performing a large number of experiments unnecessarily with much expense in time and materials [47, 48]. The program suggested performing a set of 17 experiments.

After obtaining the optimal deposition conditions with the above described variables, a brief study on the temperature of the heating plate surface was also performed to conclude if higher temperatures allowed obtaining samples with better performances. It was also studied if placing a stainless steel cylindrical protective structure around samples (17 cm diameter and 17 cm height) would create a more favourable deposition environment, either in terms of temperature stabilization during the tests or in terms of spray droplets dispersion.

3.2 CHARACTERIZATION OF SAMPLES

3.2.1 PHOTOELECTROCHEMICAL CELL SETUP

The PEC cell device, known as “cappuccino”, was chosen to perform the electrochemical characterization. The cappuccino cell (Figure 3.6) is made of polyetheretherketone (Erta PEEK®) and has a 20 mm diameter uncoated fused silica window (Robson Scientific, England) pressed against an o-ring by a metallic window part [10, 14, 38]. This cell was filled with a 1.0 M NaOH (25 ºC, pH=13.8) electrolyte solution in which the photoelectrode was immersed. The total immersed active surface area was approximately 2.5 cm^2, 0.5 cm^2 of which being illuminated through an external mask. A 99.9 % pure platinum wire (Alfa Aeasar®, Germany) was used as counter-electrode. A standard 3-electrode configuration was considered, being the Ag/AgCl/Sat KCl electrode (Metrohm, Switzerland) used as a reference electrode (RE), the platinum wire as counter-electrode (CE) and the photoanode as working electrode (WE) [10, 14, 38].

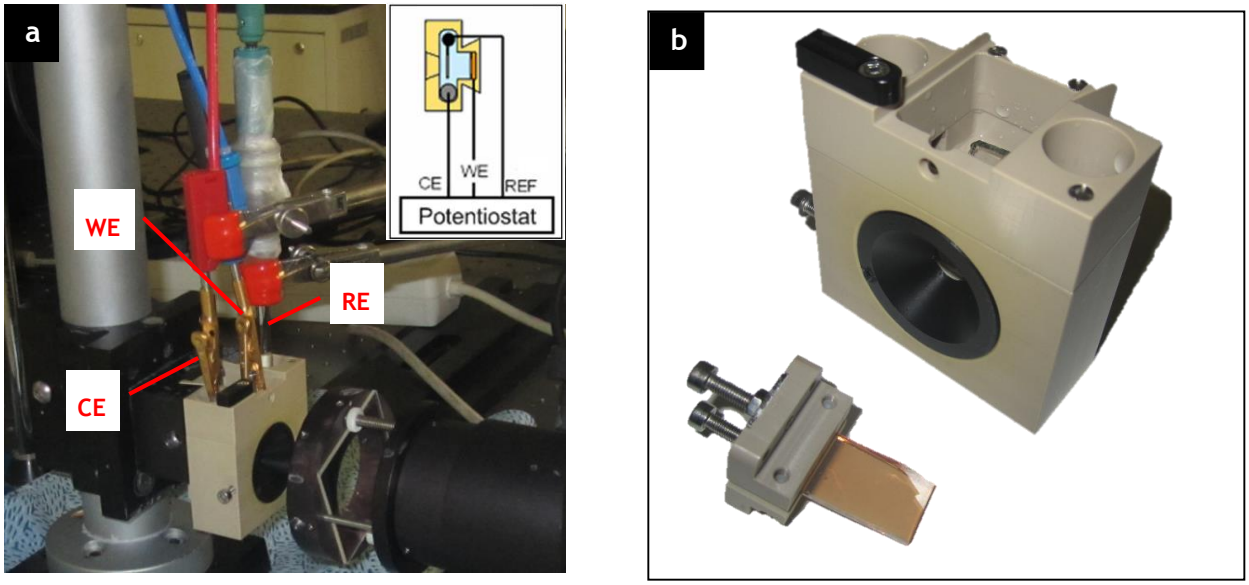

Figure 3.6 *- Details of the test bench; a) the cappuccino PEC cell supported on the precision rail and carrier in a 3-electrode configuration; b) the cappuccino PEC cell with a hematite sample placed on the sample holder;*

3.2.2 *I-V* MEASUREMENTS

The photocurrent-voltage *(I-V)* characteristic curve was obtained by applying an external potential bias to the cell and measuring the generated photocurrent using a ZENNIUM workstation (Zahner Elektrik, Germany, Figure 3.7 a) controlled by Thales software package (Thales Z 2.0). The measurements were performed at 25 °C in the dark and under 1-sun simulated sunlight, calibrated with a c-Si photodiode, at a scan rate of 10 $mV \cdot s^{-1}$ between 0.8 and 1.8 V_{RHE}. Two *(I-V)* curves were obtained in the dark, two in the exposure to the sunlight and one after the exposure to sunlight for each sample to allow the results validation. A standard 3-electrode configuration was used. The measured potential was corrected for reversible hydrogen electrode potential units (V_{RHE}) and the measured current values were corrected for the sample area that was effectively illuminated by the simulator.

***Figure 3.7** - Photoelectrochemical cells characterization equipment; a) the Zanher Zennium workstation; b) Newport sunlight simulator.*

3.2.3 STABILITY TESTS

Stability issues are one of the most important problems to be solved in photoelectrochemical cells [10, 50]. Usually, when a semiconductor electrode is placed in contact with an electrolyte solution, ionic oxidation or reduction of the semiconductor with simultaneous reduction or oxidation of a component can occur. Some n-type semiconductors such as α-Fe_2O_3 are sufficiently stable in aqueous electrolytes because their decomposition is controlled by very slow corrosion reaction kinetics [10, 12, 16, 50]. Thus, it is of utmost importance trying to obtain stable samples to ensure constant efficiency of energy conversion for the longest possible amount of time. The conversion efficiency of sunlight into stored energy (the solar fuel) is generally named solar-to-hydrogen efficiency (STH) and is one of the key performance indicators of a PEC cell [12, 13]. The STH in terms of Gibbs free energy has been chosen as the efficiency measurement in some recent studies aiming to standardize semiconductor photoelectrochemistry characterization [12, 13]. During the stability tests, the hematite photoanodes were continuously submitted to simulated solar illumination (1 sun, AM 1.5G, 1000 $W \cdot m^{-2}$) at a specific potential (in this study 1.45 V_{RHE} was considered) and the correspondent current density response was measured over time. *I-V* curves were obtained time to time to check the photoanode performance. The curves in the dark allowed assessing if the dark current appeared at lower potentials in the course of time. It was assumed that the stability test should be finished if a 10 % decrease in the generated photocurrent was observed.

3.2.4 FILM THICKNESS

UV-visible absorption data was used to estimate the thickness of the hematite samples. Since there is a similarity in the shape of the spectra of all samples, their thicknesses can be estimated assuming a Lambertian absorption behaviour:

$$\ln\ (1 - A) = -\ \alpha \cdot \ell \qquad (3.1)$$

where A is the absorbance, α is the hematite absorbance coefficient taken at $(44\ nm)^{-1}$ for a wavelength of 400 nm and ℓ is the thickness of the hematite film in nanometres [10, 51].

To measure the samples absorbance it was used a spectrophotometer that measured the reflectance and transmittance of samples. Then the absorbance of samples was calculated by the following expression:

$$Abs_{corrected}\ (\%) = Abs_{sample}\ (\%) - Abs_{FTO}\ (\%) \qquad (3.2)$$

Since the glass substrate was not 100 % transparent (Figure 3.8 a) it was necessary to measure the absorbance of FTO glass (control) to then make the correction of the absorbance value for each sample. The absorbance (in percentage) was calculated by subtracting to the incident radiation the transmitted and reflected radiation percentages both measured by the device. This procedure can be more easily understood with the scheme of Figure 3.8 b.

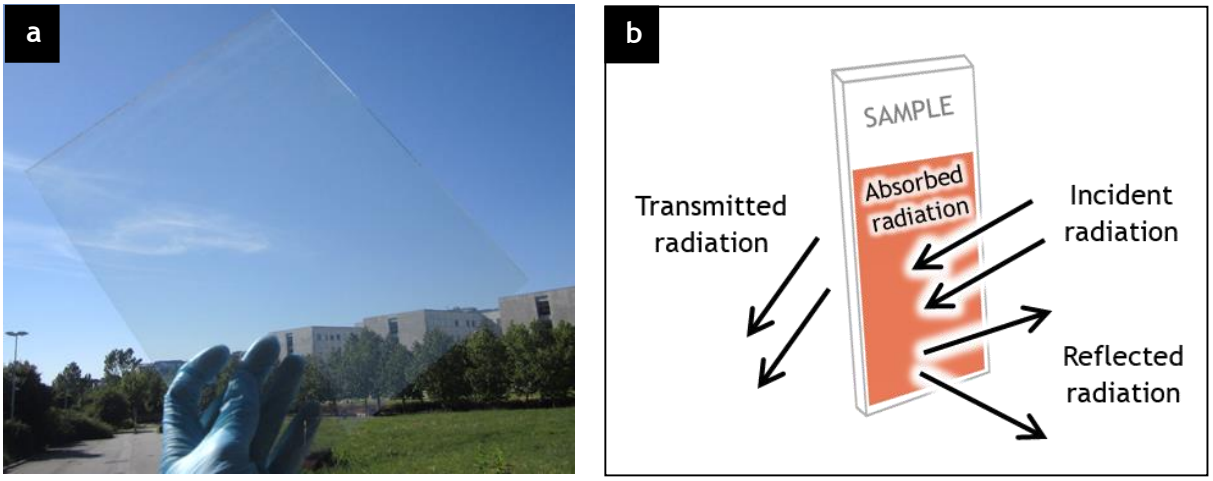

Figure 3.8 *- a) The FTO glass substrate; b) Scheme of the incident radiation behaviour in a hematite film sample.*

3.2.5 SCANNING ELECTRON MICROSCOPY (SEM) ANALYSIS

The morphology of the sprayed hematite thin films and the FTO glass were also characterized using a high-resolution scanning electron microscope (SEM). These analyses were performed at the University of Porto Materials Centre (CEMUP) and a high-resolution environmental scanning electron microscope (Schottky) with X-ray microanalysis and patterns of backscattered electron diffraction analysis was used (FEI Quanta ESEM 400FEG / EDAX Genesis X4M).

4 RESULTS AND DISCUSSION

4.1 PRELIMINARY TESTS

The preliminary tests were very important to validate the experimental setup and for improving operating details that can only be detected after assembling. Moreover, they enabled obtaining the first set of results for the study of some optimization parameters. It was used the same hematite precursor solution in all preliminary tests: 10 mM of $Fe(AcAc)_3$ (99.9 %, Aldrich) in EtOH (≥ 99.5 % Aga) [36]. As explained before, the first depositions were made using a HPLC pump to feed the solution into the spray nozzle. Though, during the solution suction air bubbles were often formed and so it was decided to replace this pump by a pressurized tank. Since some depositions were already performed with the HPLC pump, these results were compared with the results obtained with the pressurized tank for validation – Table 4.1. Although the current density values obtained for the samples produced with the pressurized tank were lower than the HPLC pump results, they showed better reproducibility - Table 4.2.

***Table 4.1** - Results validation concerning the use of the pressurized tank for different deposited volumes.*

Volume of deposited solution (ml)	Current density at 1.45 V_{RHE} - HPLC pump ($mA \cdot cm^{-2}$)	Current density at 1.45 V_{RHE} - pressurized tank ($mA \cdot cm^{-2}$)	Major difference between the results obtained for the samples produced with the HPLC pump and with the pressurized tank (%)
30[1]	2.74×10^{-3}	-	-
40[1]	3.39×10^{-1}	-	-
50	5.95×10^{-1}	4.75×10^{-1}	14.6
60	4.72×10^{-1}	4.04×10^{-1}	14.5
70	4.70×10^{-1}	4.32×10^{-1}	7.9
80	5.10×10^{-1}	4.32×10^{-1}	15.3
90	4.82×10^{-1}	4.18×10^{-1}	13.4

[1]No preliminary tests were performed with the pressurized tank for 30 and 40 ml because the results achieved with the HPLC pump clearly showed that these volumes produced very low photocurrent values.

***Table 4.2** - Major difference between the current density values obtained for each series of 3 samples for the two studied cases: depositions with the pump and with the pressurized tank.*

Volume of deposited solution (ml)	Difference between the results obtained for each series of samples produced with the HPLC pump (%)	Major difference between the results obtained for each series of samples produced with the pressurized tank (%)
30	85.3	-
40	16.9	-
50	12.7	3.6
60	31.4	1.5
70	30.8	2.2
80	2.9	1.5
90	4.8	0.2
100	-	6.8

The first parameter tested and identified as critical was the amount of deposited solution. Theoretically, the volume of sprayed solution directly influences the hematite film thickness, which in its turn affects the amount of absorbed light and, consequently, the generated current density, as explained in Chapter 2. Current density results obtained for various samples with different deposited volumes are presented in Table 4.1 and in Figure 4.2. The correspondent *I-V* characteristics are shown in Figure 4.1.

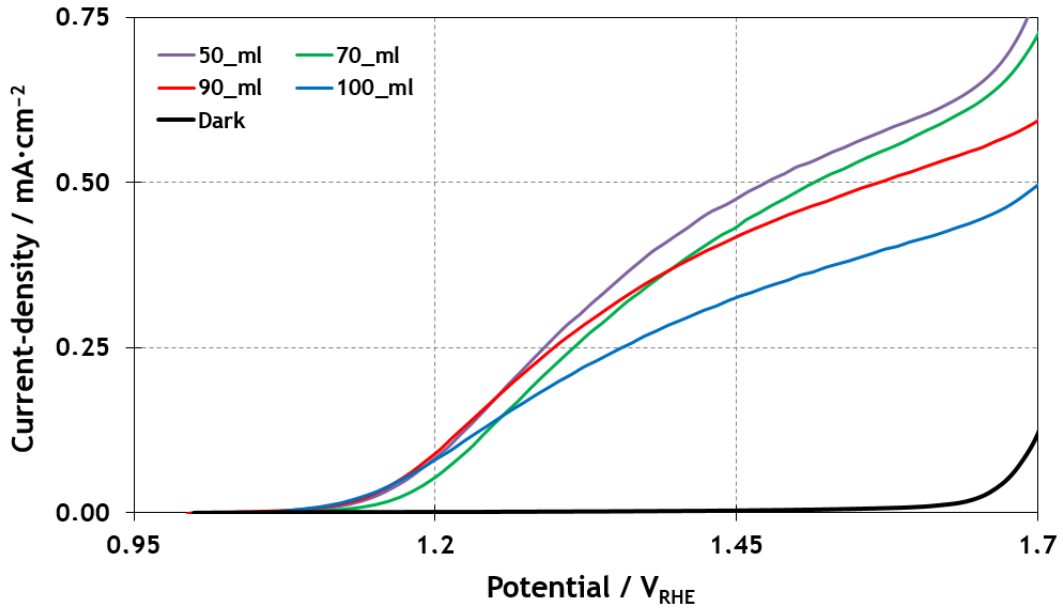

***Figure 4.1** - Current density vs. potential characteristic curves for the samples prepared using the pressurized tank for different volumes.*

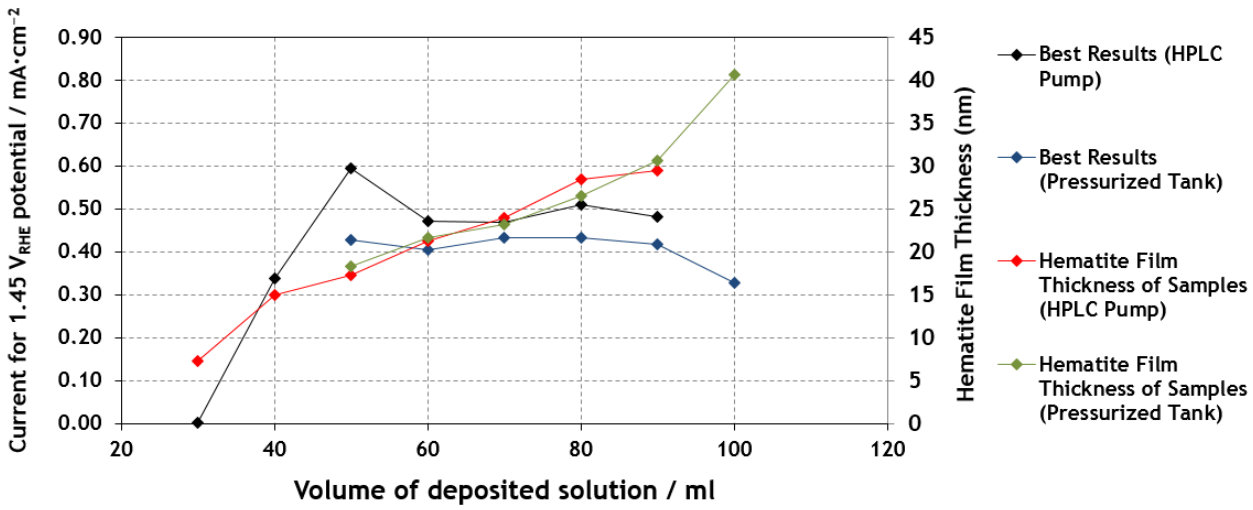

***Figure 4.2** – Current density values (at 1.45 V_{RHE}) as a function of deposited volume (using a HPLC pump and the pressurized tank). Evolution of the hematite film thickness with the sprayed volume.*

Besides the deposited volume, the preliminary tests also included the optimization of two other parameters: i) the spray nozzle height and ii) the interval of time between sprays during a deposition. Based on these first tests the upper and lower limits were identified. The optimal value for the volume of solution to be deposited should be in the interval of 45 to 95 ml - Table 4.1. It was also found that the optimal value for the height of the nozzle should be in the range of 20 to 40 cm and the optimal time interval between sprays should be in the range of 15 to 45 seconds.

4.2 DoE – Searching for the optimal deposition conditions

After identifying the parameters that most influence the current density, a Design of Experiments (DoE) tool was used to perform the complete optimization of bare hematite deposition with the utmost rigor. A commercially available software for DoE analysis - JMP 5.01 (SAS software) - was used. According to the procedure described in Chapter 3 and using the DoE software, it was possible to define a set of experimental conditions for hematite deposition; the defined response variable was the current density at 1.45 V_{RHE}. The results for each experiment of the optimization procedure are shown in Table 4.3. Three samples for each set of experimental conditions were performed to assess reproducibility.

***Table 4.3** - Set of experimental conditions defined by the JMP software for DoE optimization and correspondent current density value (response variable).*[2]

Volume of deposited solution (ml)	Spray height (cm)	Time between sprays (s)	Average current at 1.45 V_{RHE} potential ($mA \cdot cm^{-2}$) for the 3 samples series	Film thickness (nm)	Major difference between current results for the 3 samples series
45	40	15	1.81×10^{-1}	20.1	65.2 %
45	40	45	2.40×10^{-1}	17.5	15.6 %
45	20	15	3.41×10^{-1}	21.2	4.5 %
95	30	30	3.76×10^{-1}	31.9	1.1 %
45	30	30	3.79×10^{-1}	19.1	7.0 %
95	40	15	3.79×10^{-1}	29.8	7.7 %
95	20	15	3.98×10^{-1}	26.7	5.0 %
95	20	45	4.13×10^{-1}	30.2	13.9 %
70	20	30	4.34×10^{-1}	26.1	6.2 %
70	40	30	4.34×10^{-1}	33.4	4.5 %
70	30	15	4.35×10^{-1}	22.5	1.9 %
45	20	45	4.40×10^{-1}	21.6	5.4 %
70	30	30	4.44×10^{-1}	22.7	4.9 %
70	30	30	4.62×10^{-1}	25.1	7.8 %
70	30	45	4.78×10^{-1}	26.2	14.9 %
70	30	30	4.86×10^{-1}	25.8	8.8 %
95	40	45	5.07×10^{-1}	28.0	12.2 %
95	20	45	5.62×10^{-1}	44.6	5.8 %
115	30	30	3.89×10^{-1}	31.1	3.1 %

Table 4.3 shows that the experimental deposition method allowed producing hematite photoanodes with good reproducibility since there was a difference of less than 10 % in the current density results for the majority of experiments. By analysing the results of Table 4.3 it was found that although the majority of the best results were obtained for a volume of 70 ml of sprayed solution, the two highest photocurrents were obtained for 95 ml (0.507 $mA \cdot cm^{-2}$ and 0.562 $mA \cdot cm^{-2}$). However, most of the results obtained for this volume were much lower (0.376 $mA \cdot cm^{-2}$ to 0.413 $mA \cdot cm^{-2}$). It was then decided to perform a screening test to see if the current density continued to increase with the sprayed volume. This screening test consisted of a 115 ml deposition (shaded highlighted in the Table 4.3 since this was not part of DoE set of experimental conditions). The current density obtained in this test (0.389 $mA \cdot cm^{-2}$) confirmed that the volume of 70 ml should be the optimal value. Contrarily to what was expected, the

[2] Important to mention that the values in the table are organized from the lowest to the highest photocurrent density value.

results of Table 4.3 indicate that there is not a direct relation between deposited volume of solution and film thickness. This suggests that other parameters were influencing the growth of hematite crystals. Furthermore, it is possible to conclude that the film thickness is not easy to control in a spray pyrolysis setup with a basic configuration including only the spray nozzle with its control box and a heating plate. Nevertheless, these data allow inferring that the ideal hematite film thickness should be between 25 and 35 nm, as shown in Figure 4.3. These thicknesses are in agreement with the values reported in the literature for hematite films deposited by spray pyrolysis [16, 52, 53]. Thus, the film should have sufficient thickness to ensure good light absorption, but not too large to avoid surface recombination before reaching the external circuit.

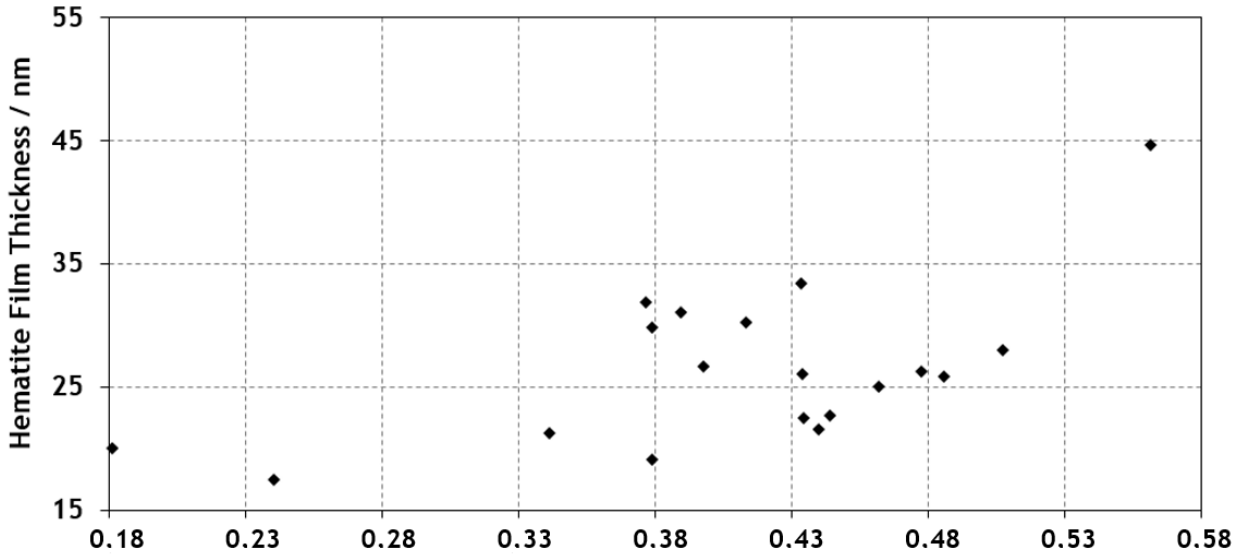

***Figure 4.3** - Relation between the thickness of the hematite film and the measured current density at 1.45 V_{RHE}.*

Although the amount of deposited solution does not directly influence the thickness of the hematite film, it induces a clear difference in colour of the film (Figure 4.4), which is gradually darker for higher values of sprayed volume.

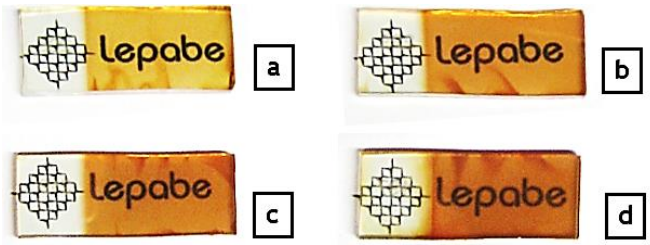

***Figure 4.4** - Colour difference between samples where different volumes of hematite precursor were sprayed: a) 45 ml; b) 70 ml; c) 95 ml; d) 115 ml.*

It is then easily understandable that, from a given volume of sprayed solution, the film becomes so thick that the sample starts to lose transparency and inevitably loses performance due to bulk charge recombination. It should be noted that the darker samples also show worse performance due to poor crystal growth.

Figure 4.5 shows the SEM images of three hematite samples with different values of sprayed volume. It is clearly observed that as the amount of sprayed solution increases, the FTO surface structure becomes less noticeable due to the greater amount of hematite existing over it.

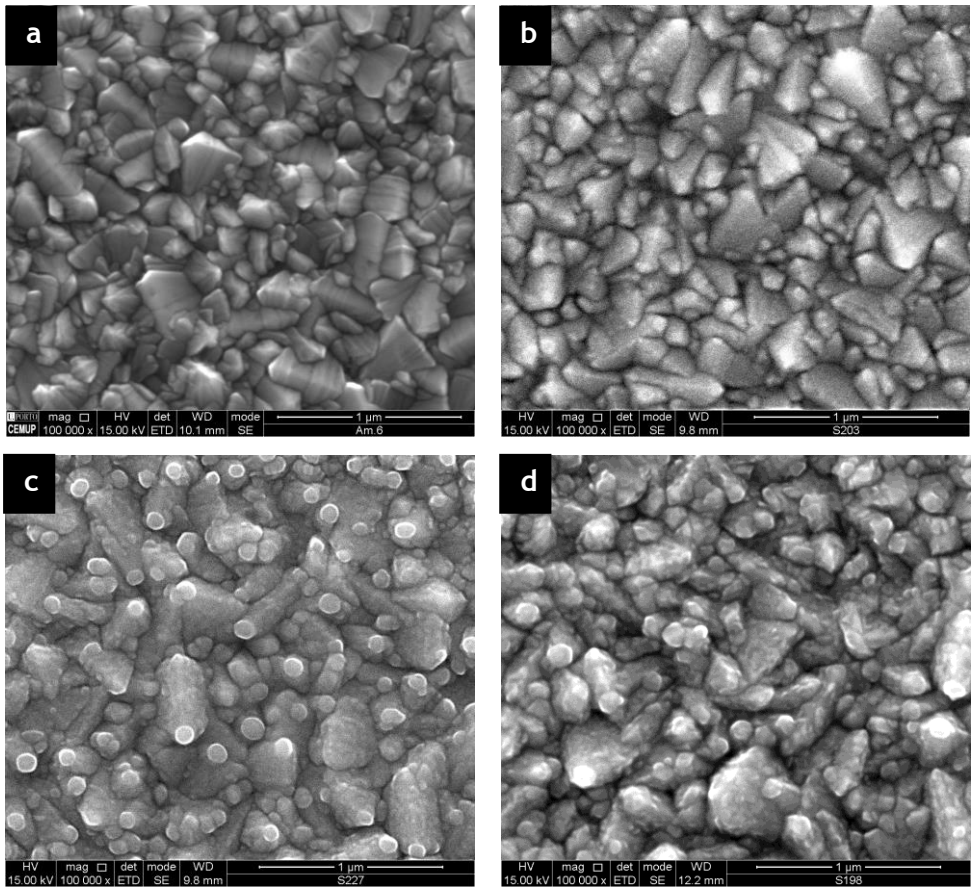

***Figure 4.5** - Top view SEM images; a) FTO glass substrate; b) sample with 45 ml of sprayed solution; c) sample with 70 ml of sprayed solution; d) sample with 95 ml of sprayed solution.*

Another parameter that has a great influence on the morphology of the hematite film is the time between sprays. It is expected that a higher time gap between sprays allows a better crystal growth and better temperature stabilization. SEM images of samples corresponding to the three values of time between sprays tested in the DoE study are shown in Figure 4.6. As the time between sprays increases, the crystals have enough time to grow and to better adhere to the substrate. These images also show that the morphology obtained is again in straight agreement with previous hematite structures reported in the literature [11, 12, 14, 16, 54].

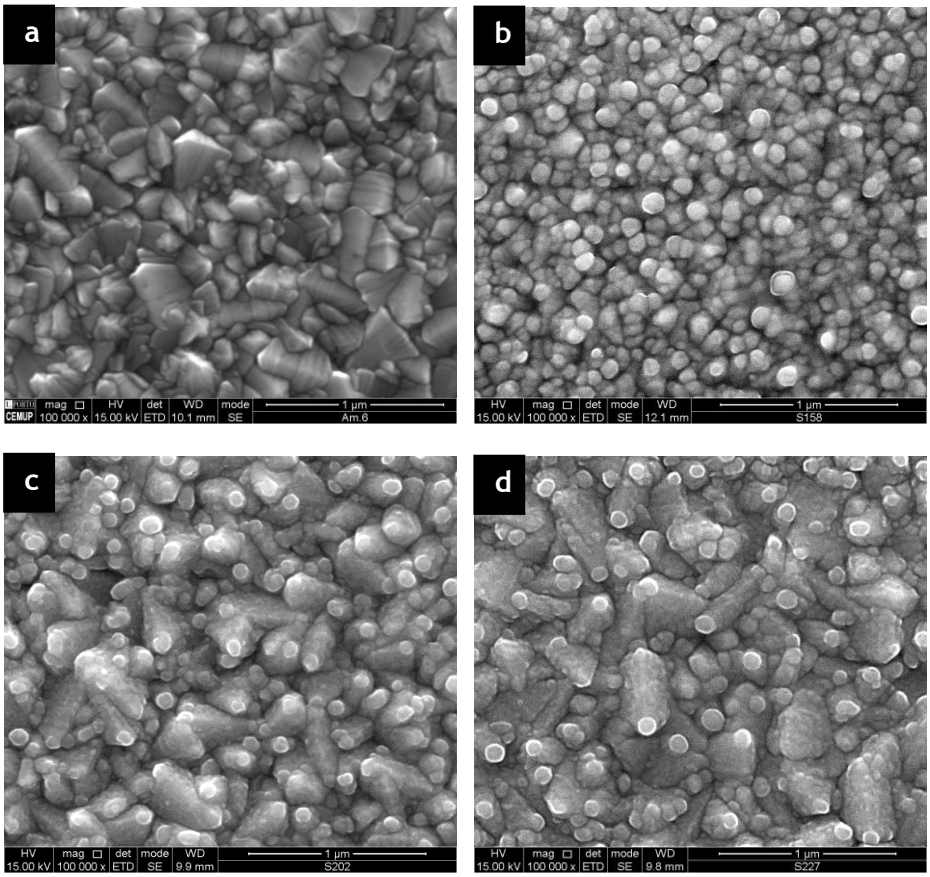

Figure 4.6 *- Top view SEM images; a) FTO glass substrate glass used in depositions; b) sample with a 15 s time gap between sprays; c) sample with a 30 s time gap between sprays; d) sample with a 45 s time gap between sprays.*

After performing the combination of experimental conditions suggested by the DoE software, the user gives as input the response variable (in this case is the current density at 1.45 V_{RHE}). Based on this information the *Prediction Profiler* tool of the software obtains the set of operating conditions able to maximize the current density - Figure 4.7. The optimal operating conditions obtained were: sprayed volume of 70 ml, spray nozzle height of 20 cm and 45 s time gap between sprays.

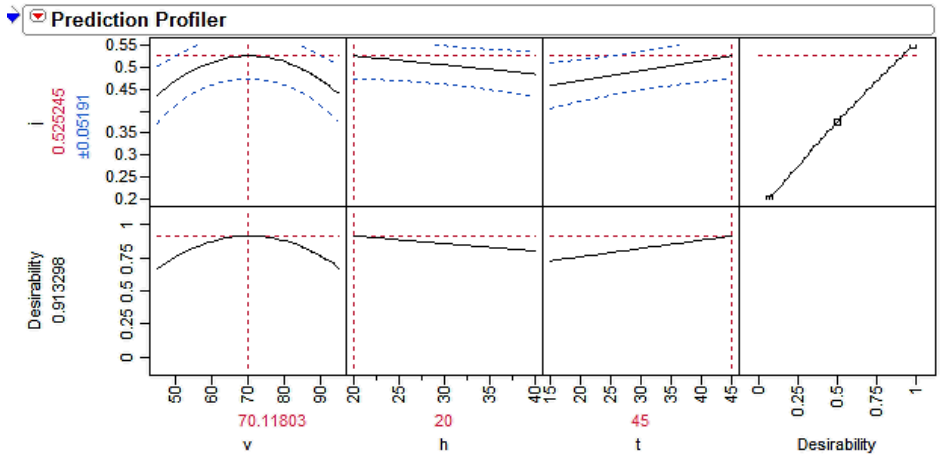

Figure 4.7 *- Prediction Profiler result for optimizing hematite deposition conditions.*

After performing the DoE study, it is also important to verify if the current density values predicted by the software match with the experimental results. The predicted response values for each set of experimental conditions are presented in Appendix D. The graph that appears in the section *Actual by Predicted Plot* of the software (Figure 4.8) represents the value of the response variable obtained experimentally, *j Actual*, vs. the value predicted by the model for the response variable, *j Predicted*. Therefore, it is clear that, for each experiment, the closer the points are to the diagonal line, the best the model fits. The red dashed lines on both sides of the diagonal central line correspond to the prediction error margin and introduce a confidence interval in the results.

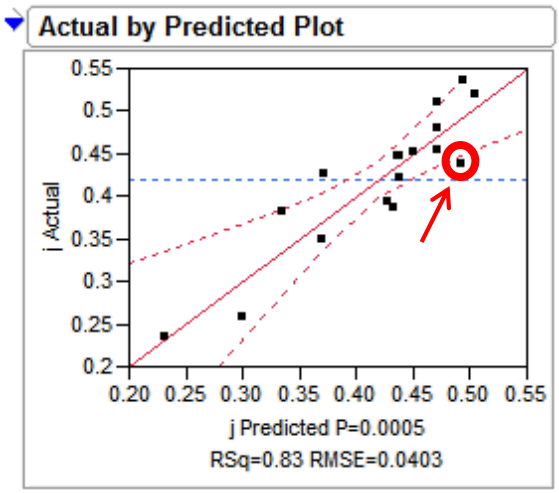

Figure 4.8 *- Current density values obtained experimentally for each set of operating conditions and the correspondent predicted values by the model for the defined confidence interval. The point marked with a red circle corresponds to the only result in the high range density current that stayed outside the confidence interval predicted by the software.*

As Figure 4.8 suggests, almost all the obtained results are in agreement with the values predicted by the model, being therefore within the error ($\pm$ 0.0786 mA·cm^{-2}) for the confidence interval. For higher current density values, approaching the predicted maximum current density value, there was only one result out of the confidence interval, which gives consistency to the results and indicates a correct use of the experimental setup.

The *Scaled Estimates* section of the program examines the influence of each design variables on the response variable and the interactions between the parameters in the same response value. This tool allowed concluding that the parameter that most influenced the performance of the samples was the volume of deposited solution.

4.3 TEOS PRE-TREATMENT

After obtaining the optimal operating conditions for the deposition of undoped hematite, it was attempted to improve the *I-V* characteristic of the samples under standard sunlight conditions, both in terms of produced current density and onset potential. Several studies showed that a SiO_x layer can act as an amorphous buffer that reduces the interfacial strain between the FTO and hematite crystals. The reduced interfacial strain leads to better Fe_2O_3 film organization [12, 15, 36]. Thus, after performing a TEOS (tetraethyl orthosilicate) pre-treatment it is expected to see a change in hematite crystal growth and a better photo activity response.

As described in Chapter 3, during the pre-treatment with TEOS the FTO glass substrates were hand-sprayed with an ethanol solution with 10 % of TEOS (Sigma Aldrich, 98 %) at 450 ºC. After this pre-treatment, hematite was deposited using the optimal conditions obtained by the DoE study. The correspondent *I-V* characteristic curves are exhibited in Figure 4.9.

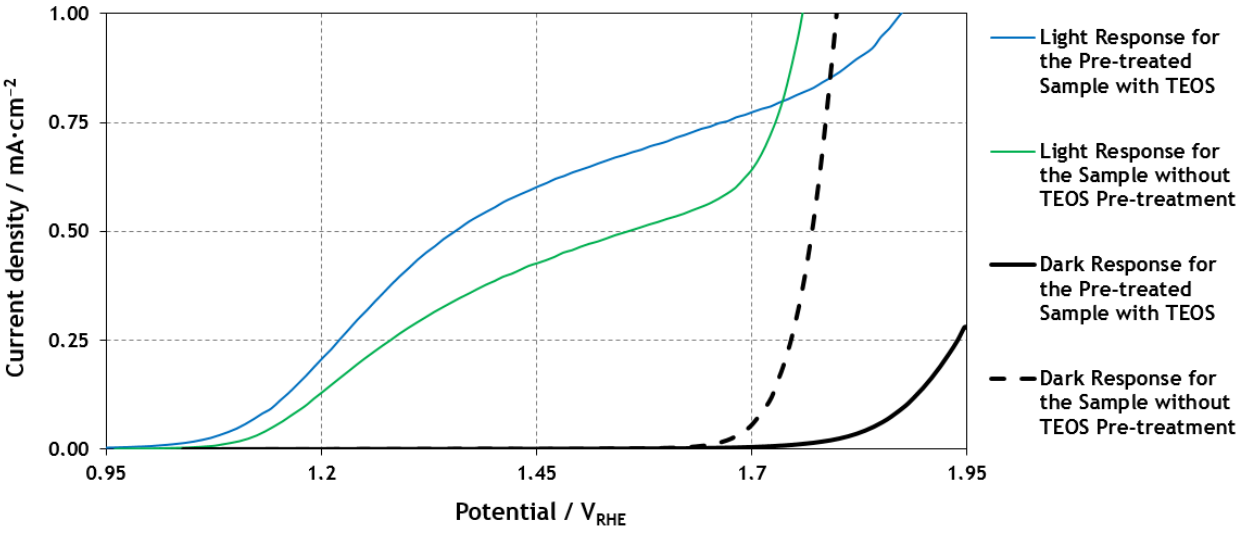

***Figure 4.9** – I-V characteristic curves of the prepared photoanodes in the dark (dashed and solid black lines) and under simulated solar illumination (AM 1.5 G 100 mW·cm^{-2}, coloured lines) with and without TEOS pre-treatment.*

As expected, the pre-treated sample with TEOS yielded a much higher current density and a lower onset potential, which allowed achieving a much higher current density at 1.23 V_{RHE}. For the optimal deposition conditions, the pre-treated sample with TEOS showed a current density of 0.601 mA·cm^{-2} at 1.45 V_{RHE}, whereas the sample without pre-treatment showed only a current density of 0.427 mA·cm^{-2}. This represents an increase of about 29 % on the performance of the sample. It can thereafter be concluded that these results are very promising since they are very similar to the best photoresponses reported in other studies [36].

A significant improvement occurred in the photocurrent produced by the samples pre-treated with TEOS, thus it is important to understand how morphology changed to explain this performance enhancement. Figure 4.10 shows the SEM images of the samples with and without TEOS pre-treatment.

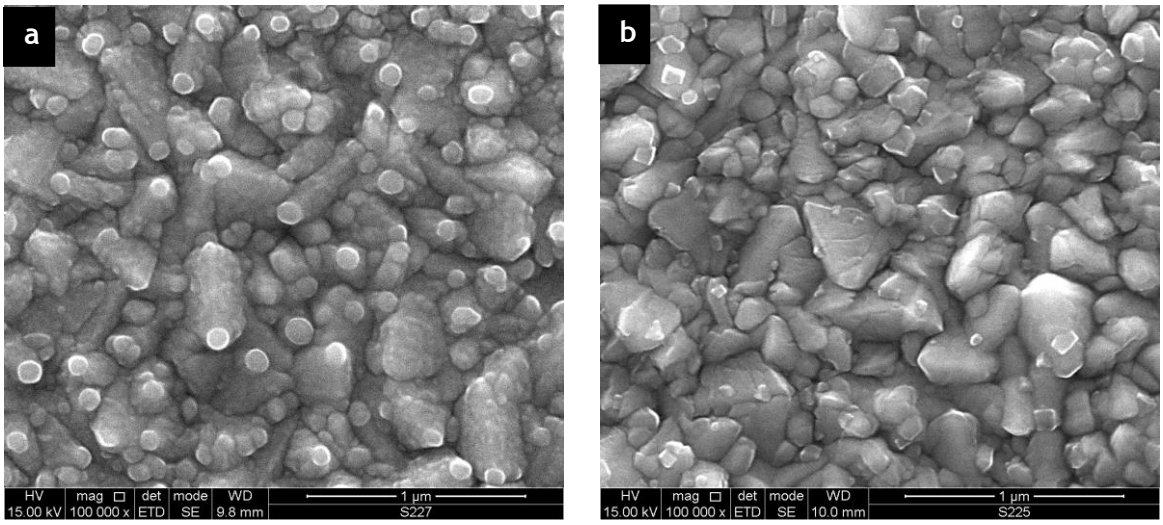

***Figure 4.10** - Top view SEM images of hematite films produced with the optimal conditions obtained by the DoE study: a) without TEOS pre-treatment; and b) with TEOS pre-treatment.*

In Figure 4.10 a) it is possible to observe clusters formation suggesting that after a critical Fe_2O_3 film thickness (which was probably achieved) island formations appeared (Volmer–Weber growth). In this growth mode, adatom-adatom (atom that lies on a crystal surface and can be thought of as the opposite of a surface vacancy clusters or islands) interactions are stronger than those of the adatom with the surface, leading to the formation of three-dimensional adatoms. Growth of these clusters, along with coarsening, will cause rough multi-layer films to grow on the substrate surface. In Figure 4.10 b) the morphology of the film is more likely to be in accordance with a Stranski–Krastanov growth mode. Also known as 'layer-plus-island growth', this mode follows a two-step process. Initially complete films of adsorbates, up to several monolayers thick, grow in a layer-by-layer way on a crystal substrate. Beyond a critical layer thickness, which depends on strain and the chemical potential of the deposited film, growth continues through the nucleation and coalescence of adsorbate "islands" [12, 36, 55]. This is an intermediary process characterized by both 2D layer and 3D island growth in which surface adhesive force is stronger than adatom cohesive force. This difference in species interactions and film growth type can be explained by the difference in interfacial tension due to crystal matrix incompatibility. In Appendix E a schematic representation of these two growth modes is shown. The obtained morphologies are in accordance with the results obtained in the study of Le Formal *et al.* [12, 36]. As showed in Appendix F the FTO substrate shows itself an onset

potential of the dark current at about 1.6 V_{RHE} with faster water oxidation kinetics than any of the hematite electrodes. Therefore, all FTO area should be covered for allowing the dark current onset to appear at greater potential. For this purpose, a Stranski–Krastanov growth mode is better than the Volmer–Weber growth mode, which can be ensured by the TEOS pre-treatment.

4.4 STABILITY TEST

One of the most important contributions and perhaps the most innovative aspect of this study was the stability test that was performed. As described above, the stability test consisted of subjecting the sample to simulated sunlight radiation for several hours at a fixed potential. When such exposure was interrupted, *I-V* curves were obtained in the dark and under simulated sunlight. The results of the stability tests are shown in Table 4.4 and in Figure 4.11.

***Table 4.4** – Current density values at 1.45 V_{RHE} for different times of continuous exposure to simulated sunlight radiation.*

Time (h)	Current density at 1.45 V_{RHE} ($mA \cdot cm^{-2}$)	Overall efficiency gain / loss (compared to the first measurement) / %
0	5.87×10^{-1}	-
12	6.11×10^{-1}	4.0
24	6.06×10^{-1}	3.2
36	5.92×10^{-1}	1.0
48	5.90×10^{-1}	0.6
60	6.46×10^{-1}	9.2
72	5.99×10^{-1}	2.1
84	6.07×10^{-1}	3.3
96	6.12×10^{-1}	4.1
108	6.34×10^{-1}	7.5
120	5.92×10^{-1}	1.0
132	6.16×10^{-1}	4.9
144	6.13×10^{-1}	4.3
156	6.27×10^{-1}	6.5
168	6.28×10^{-1}	6.6

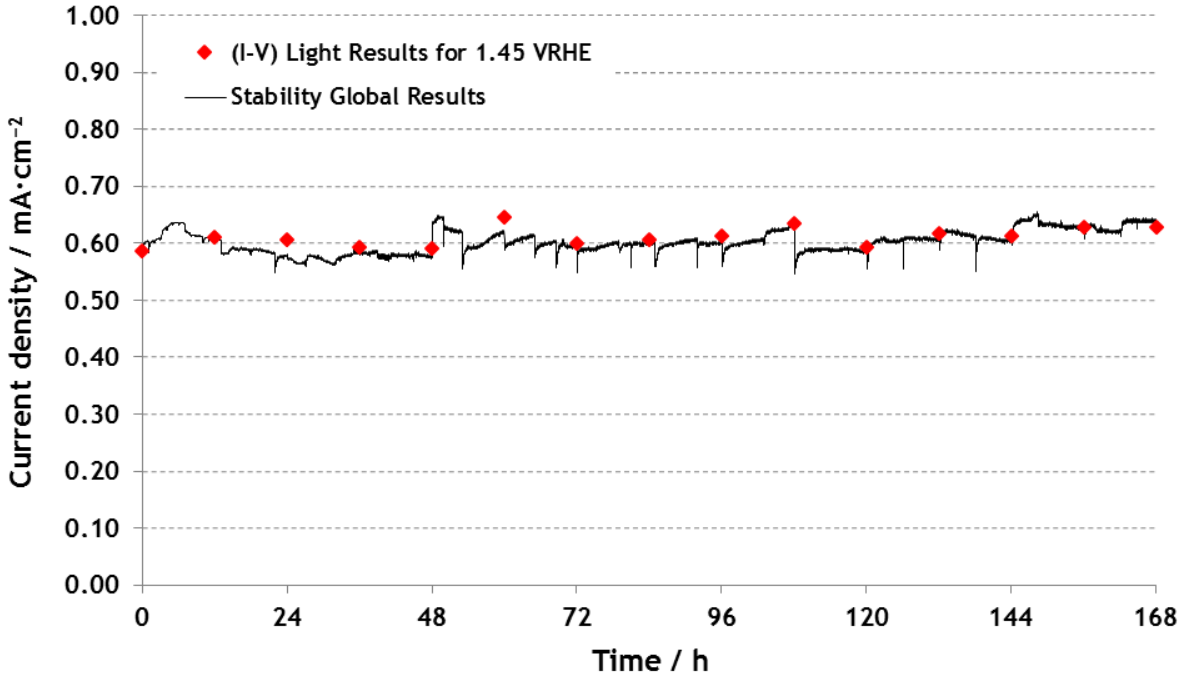

Figure 4.11 *- Polarization curve of hematite sample deposited with the optimal operating conditions with TEOS pre-treatment (applied potential of 1.45 V_{RHE} under 1 sun irradiation). The red dots represent the current density values at 1.45 V_{RHE} obtained every 12 h of simulated sunlight exposure. The peaks of current density values that appear in the black line correspond to the moments when the stability test was restarted.*

As it can be seen from the obtained results, after 168 hours of sun exposure the sample showed an improvement in its performance of more than 6 % compared with the first *I-V* measurement. As described in chapter 3, it was decided that the stability test would be stopped as soon as the sample showed a loss of 10 % in the produced current density value at 1.45 V_{RHE}. However, despite no loss in the current density was observed, the onset potential of the dark current started to emerge at lower potentials and so it was decided to stop the stability test after 168 hours - Figure 4.12. The appearance of the dark current onset at lower potentials may be related to material detachment from the substrate, leaving some FTO areas exposed. The stable photocurrent density produced over 168 hours is a great achievement, since there are no published results for stability of hematite photoanodes produced by spray pyrolysis under continuous simulated sunlight radiation exposure.

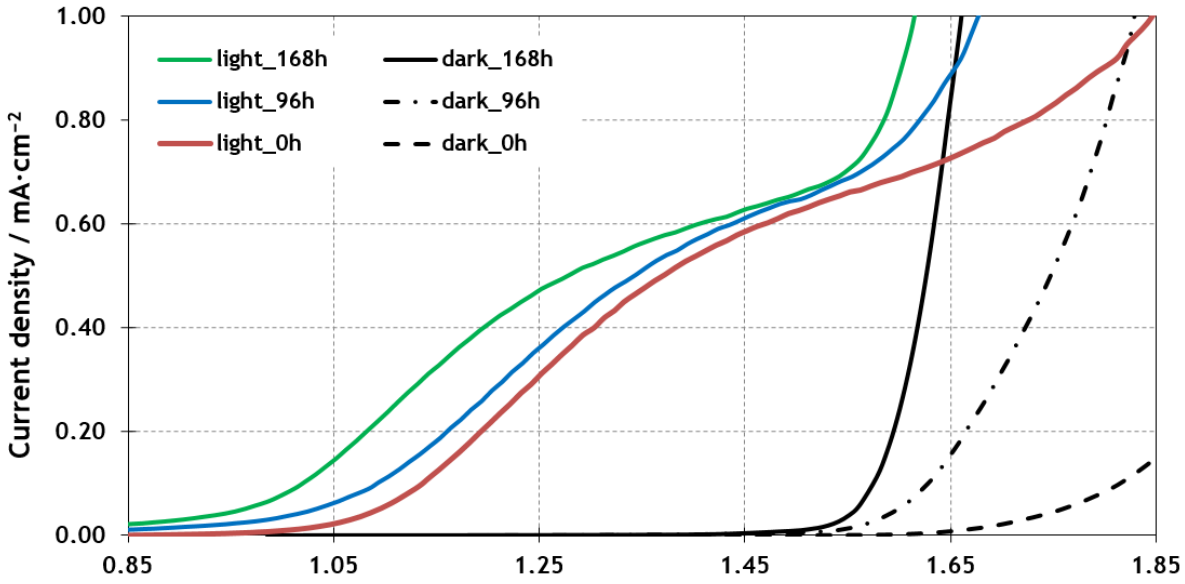

***Figure 4.12** - I-V characteristic curves of the tested sample after different periods of simulated sunlight radiation exposure (AM 1.5G 100 mW·cm^{-2}, coloured curves); the correspondent dark-current curves (black lines) are also shown.*

4.5 TEMPERATURE STUDY

After obtaining the optimal conditions for hematite deposition and improving the performance of the samples by a pre-treatment with TEOS, a brief study on the influence of temperature on the morphology of the samples was made. In this study, the optimal deposition conditions suggested by the DoE study were maintained, as well as the pre-treatment with TEOS procedure. The *I-V* results are shown in Figure 4.13.

By analysing the *I-V* curves obtained in the dark and the curves obtained under sunlight radiation, it can be concluded that the temperature of 450 °C is the optimal value for hematite deposition, allowing reaching a current density of 0.730 mA·cm^{-2}. This result is in agreement with the best published results for hematite photoanodes pre-treated with TEOS and produced by spray pyrolysis under similar experimental conditions [36]. It should be noted that this temperature range was chosen based on previous studies about hematite deposited by spray pyrolysis [36, 54, 56]. The observed improvement in the samples performance at 450 ºC may be related to changes in the hematite morphology due to temperature influence during the crystallization process. Thus, to clarify this point SEM analyses were also performed - Figure 4.14. SEM images confirm that the deposition at 450 °C allowed obtaining crystals with a well-defined cubic shape in a very well organized structure, leading to better results of current density.

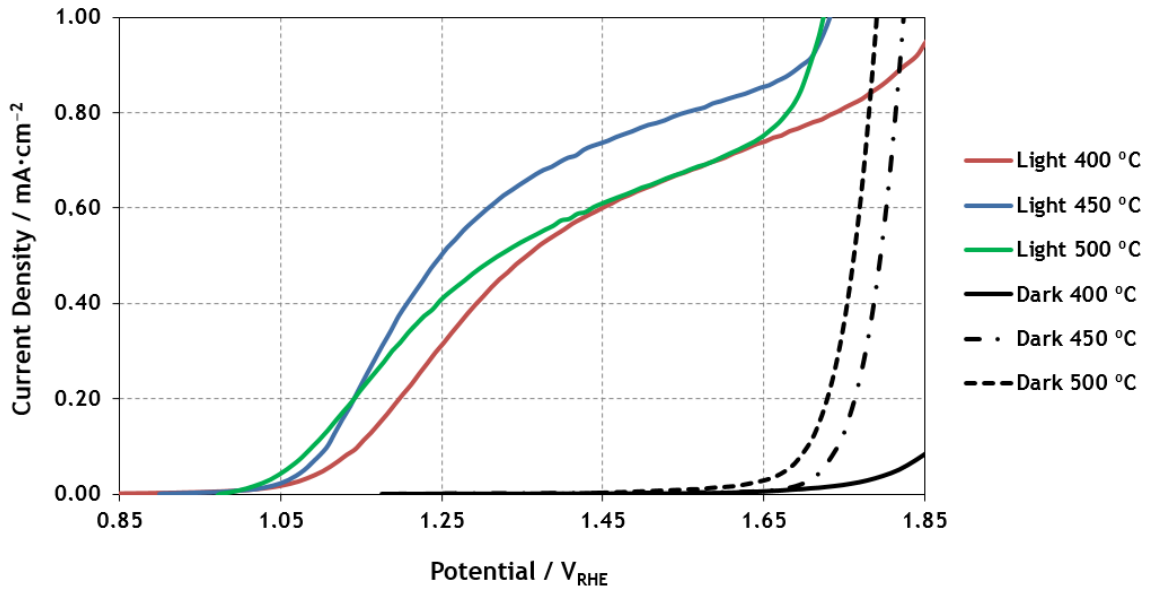

Figure 4.13 *– I-V characteristic curves of the prepared photoanodes at different temperatures in the dark (black lines) and under simulated solar illumination (AM 1.5G 100 mW·cm^{-2}, coloured curves).*

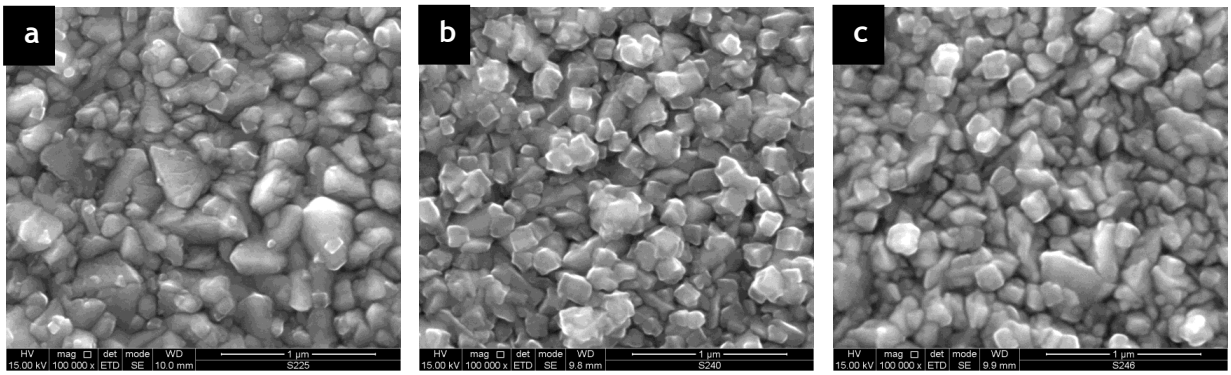

Figure 4.14 *– Top view SEM images of hematite films produced in the optimal conditions with TEOS pre-treatment at different temperatures; a) 400 ºC; b) 450 ºC; 500 ºC.*

It was also studied if placing a stainless steel cylinder around the samples would create a more favourable deposition environment, mainly in terms of temperature stabilization during the tests. The expected improvements in the sample were not observed both in terms of photocurrent production (only 0.480 mA·cm^{-2} at 1.45 V_{RHE}) and in terms of onset potential. These results are presented in Appendix G.

4.6 DOPING OF HEMATITE SAMPLES

As previously mentioned, shallow donors are used to increase the conductivity of n-type oxides [13]. Based on previous works two dopants were chosen to be tested: silicon[IV] and titanium[IV] [11-14, 54, 57, 58]. The doping procedure consisted of adding a specific volume of the dopant material solution to the iron (III) acetylacetonate precursor solution in order to obtain the desired percentage of dopant atoms per iron atoms. For the Si doping the same solution previously applied on the TEOS pre-treatment was used (tetraethyl orthosilicate Sigma Aldrich, 98 %). Doping with titanium was done using a tetra ethyl orthotitanate solution (Sigma Aldrich, 98 %) because of its low tendency to hydrolyse into TiO_2 [11]. The different experimental conditions used for doping hematite and the correspondent current density values at 1.45 V_{RHE} are shown in Table 4.5. The *I-V* characteristics for silicon and titanium doping are presented in Figures 4.15 and 4.18, respectively.

***Table 4.5** - Experimental conditions of doping tests and correspondent current density values at 1.45 V_{RHE}.*

Percentage of doping (wt.% of Fe atoms)	$Fe(AcAc)_3$ solution (mM)	Volume of deposited solution (ml)	Deposition temperature (° C)	TEOS pre-treatment	Current density at 1.45 V_{RHE} ($mA \cdot cm^{-2}$)[a]	Major difference between samples	Film thickness (nm)
Si [IV] 1 %	10	70	450	YES	4.41×10^{-2}	23.7 %	25.8
Si [IV] 1 %	10	115	450	YES	2.64×10^{-2}	23.2 %	43.6
Si [IV] 0.5 %	20	70	500	NO	4.84×10^{-1}	0.0 %	40.4
Si [IV] 0.5 %	20	70	500	YES	4.27×10^{-1}	3.4 %	
Si [IV] 0.5 %	20	100	500	NO	5.59×10^{-1}	0.1 %	49.2
Si [IV] 0.5 %	20	150	450	YES	7.85×10^{-2}	96.8 %	46.4
Si [IV] 0.5 %	20	200	500	NO	4.14×10^{-1}	31.6 %	51.4
Si [IV] 0.5 %	20	200	500	YES	4.51×10^{-1}	17.0 %	
Ti [IV] 10 %	30	70	450	NO	2.38×10^{-1}	10.7 %	38.2
Ti [IV] 10 %	30	70	500	NO	4.90×10^{-1}	2.0 %	42.0
Ti [IV] 10 %	30	70	500	YES	3.72×10^{-1}	5.7 %	45.0
Ti [IV] 10 %	20	100	500	NO	4.99×10^{-1}	18.5 %	44.8
Ti [IV] 10 %	20	100	500	YES	5.01×10^{-1}	3.8 %	44.2

[a] Average value for the 3 samples of the same series.

The first material to be tested was silicon. Firstly, TEOS solution was added to the iron (III) acetylacetonate solution that have been used so far (with a concentration of 10 mM) and the deposition was done under the optimal conditions (with TEOS pre-treatment at 450 °C for a 70 ml deposition of $Fe(AcAc)_3$).

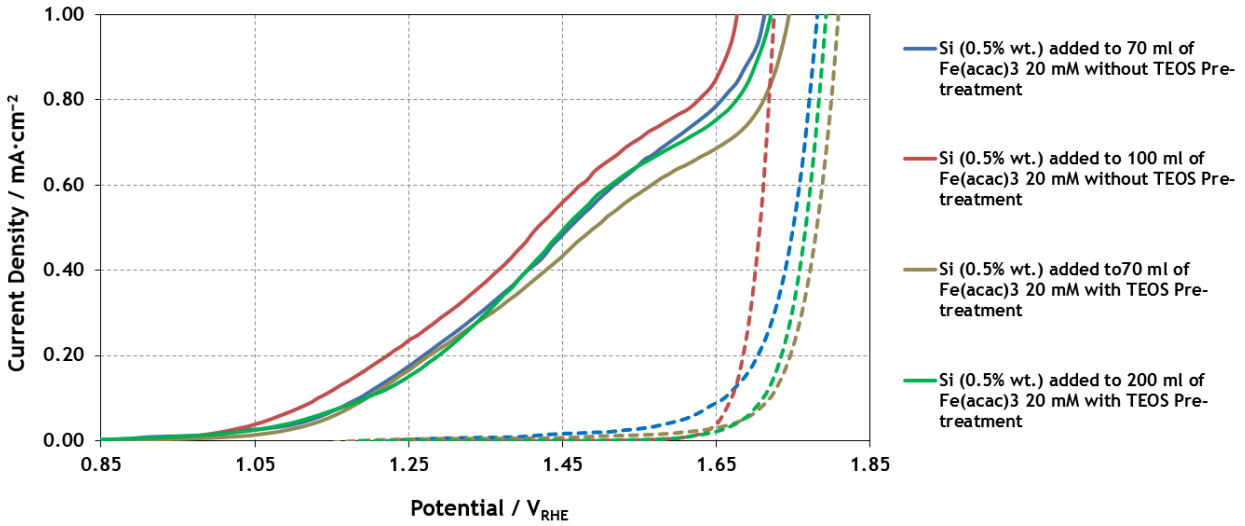

Figure 4.15 *- I-V characteristic curves of the Si [IV] doped photoanodes prepared at 500 ºC in the dark (dashed lines) and under simulated solar illumination (AM 1.5G 100 mW·cm^{-2}, solid lines).*

In the first test with Si dopant it was obtained a current density of only 0.410 mA·cm^{-2} at 1.45 V_{RHE}. Although the film thickness of this sample was 25.8 nm, the obtained colour clearly did not look like the typical colour of a hematite film, presenting a very light yellowish colouring - Figure 4.16 a). Thus, it becomes obvious that the hematite crystals did not grow with the desired morphology. To work around this problem, the volume of iron (III) acetylacetonate solution was increased to 115 ml – Figure 4.16 b). However, the results were even worse, despite the film thickness has increased to nearly the double. Even for higher volumes of sprayed solution a bright orange colour characteristic of hematite was never achieved, always tending to gradually darker reddish-brown colours (Figure 4.16 c, d, e and f). As explained before, thicker films can lead to transparency loss and inevitably performance losses due to bulk charge recombination. It should be noted that the darker samples also show worse performance due to poor crystal growth.

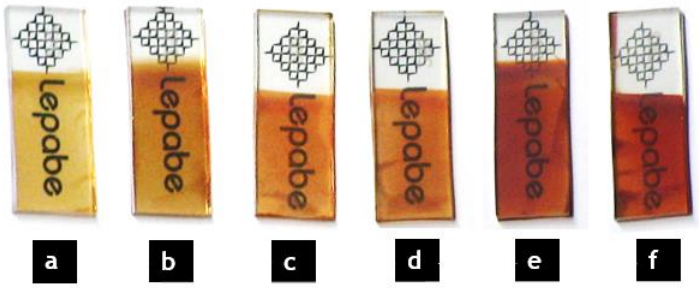

Figure 4.16 *- Colour comparison between samples prepared with different Si [IV] doping concentrations at 500 ºC: a) 1 wt.% in 70 ml of Fe(AcAc)$_3$ 10 mM with TEOS pre-treatment; b) 1 wt.% in 115 ml of Fe(AcAc)$_3$ 10 mM with TEOS pre-treatment; c) 0.5 wt.% in 70 ml of Fe(AcAc)$_3$ 20 mM without TEOS pre-treatment; d) 0.5 wt.% in 70 ml of Fe(AcAc)$_3$ 20 mM with TEOS pre-treatment; e) 0.5 wt.% in 100 ml of Fe(AcAc)$_3$ 20 mM without TEOS pre-treatment; f) 1 wt.% in 100 ml of Fe(AcAc)$_3$ 20 mM with TEOS pre-treatment.*

It is known that low concentrations of Si[IV] as dopant and high temperatures allow better current density results [11, 12]. Thereafter, the concentration of dopant was lowered to 0.5 wt. % (in relation to Fe atoms) and some depositions were made at 500 °C for different volumes of sprayed solution. Although improvements were evident under these conditions, the best result achieved with silicon doping was only of 0.559 $mA \cdot cm^{-2}$ at 1.45 V_{RHE}, being well below the value obtained in the best conditions for undoped samples with TEOS pre-treatment (0.730 $mA \cdot cm^{-2}$). Moreover, doping with silicon leaded to an increase on the onset potential and did not allowed obtaining *I-V* curves under solar illumination with a well-defined plateau (Figure 4.15). In fact, there are studies showing that, in hematite thin films, doping with silicon had a less beneficial effect on the photoactivity than other materials [11, 12, 14, 59]. On the one hand, silicon acts as an electron donor due to substitution of Fe^{3+} by Si^{4+} in the hematite lattice and thus improves electrical conductivity. Moreover, the increased donor concentration reduces the width of the space charge layer. However, on the other hand, it is known that silicon doping decreases the hematite particles size. This effect can be explained by perturbation of the hematite lattice growth due to the smaller ionic radius of Si^{4+} compared to Fe^{3+}. Silicon therefore reduces the grain size to a level that is proportionate with the hole diffusion length of only a few nanometers [11, 14, 59]. Shortly, hematite crystal growth decreases with concentration of silicon as a dopant agent, which leads to the formation of a film made of very small particles and the electron is forced to travel a much longer path to reach the conductive glass. This induces surface recombination and impairs the performance in terms of current density. A scheme that illustrates this phenomenon is shown in Appendix H.

With Ti doping, the photocurrent onset potential was considerably lowered and the photocurrent at low potentials (<1.200 V_{RHE}) was increased as Figure 4.18 shows. Furthermore, the Ti[IV] doping also reduced the dark current especially at higher applied potentials (>1.600 V_{RHE}) and allowed obtaining *I-V* curves with a well-defined plateau. Apparently Ti[IV] doping seems to favour a better crystal growth, which is evidenced by the typical red-orange colour of the produced samples.

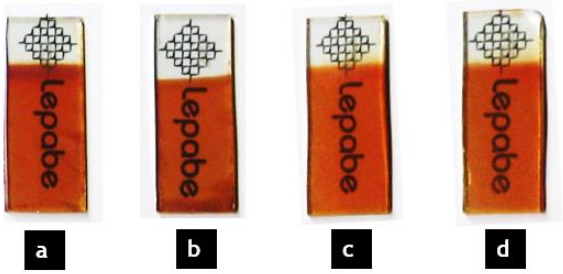

***Figure 4.17** – Colour comparison between samples with different Ti [IV] doping concentrations; a) 10 wt.% in 70 ml of $Fe(AcAc)_3$ 30 mM without TEOS pre-treatment; b) 10 wt.% in 70 ml of $Fe(AcAc)_3$ 30 mM with TEOS pre-treatment; c) 10 wt.% in 100 ml of $Fe(AcAc)_3$ 20 mM without TEOS pre-treatment; d) 10 wt.% in 100 ml of $Fe(AcAc)_3$ 20 mM with TEOS pre-treatment.*

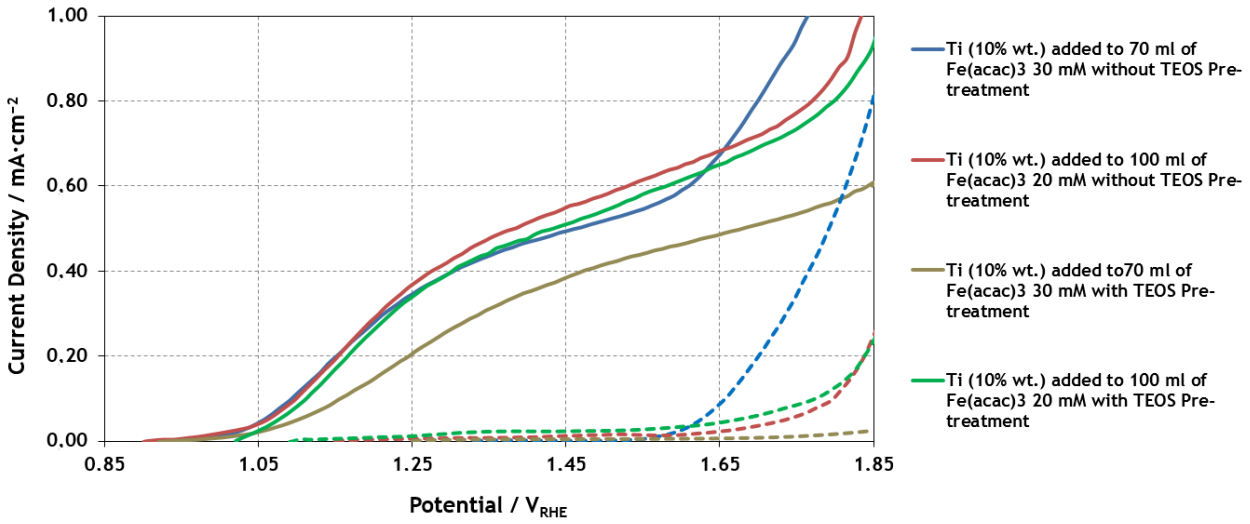

***Figure 4.18** - I-V characteristic curves of the Ti [IV] doped photoanodes prepared at 500 ºC in the dark (dashed lines) and under simulated solar illumination (AM 1.5G 100 mW·cm^{-2}, solid lines).*

This colouring is an indicator of the adequate morphology, even for samples with a lower thickness when compared to Si doping (as shown in Table 4.5). Another important aspect to note is the fact that titanium doping allows producing more reproducible samples. However, despite the improvement in performance of the samples in terms of working potential (onset potential moved to lower values, allowing current densities of ~ 0.330 mA·cm^{-2} at 1.23 V_{RHE}, and dark current moved to higher potentials), improvements in terms of current density were not achieved, which is not in accordance with published results [11, 52, 60]. Titanium should act as a negative charge carrier provider in the hematite layer, increasing the sample free carrier concentration. Ti atoms can furnish up to 4 electrons to become Ti^{4+}, whereas Fe atoms only give 3 electrons to become Fe^{3+} ions. Thus, an increase in carrier concentration should increase the conductivity of the samples. The lower currents of some prepared samples may be related to the morphology of hematite films since very high thicknesses were obtained [11, 54]. In undoped samples the holes photogenerated far from the surface recombine before reaching the surface, and the electrons created near the surface cannot reach the substrate because of recombination with holes. The expected much higher photocurrent for Ti-doped hematite would be due to a higher diffusion length of holes (lower recombination rate) in the depletion layer upon Ti doping [12, 13, 54, 57, 60].

Finally, it was shown that pre-treatment with TEOS only improves the performance of undoped samples and no improvements were observed for doped samples so far. Though, it is believed that after an optimization study of the operating conditions for doped hematite deposition, different results may be obtained.

5 CONCLUSIONS

There are many technologies that enable changing and controlling the morphology of hematite. In this work the spray pyrolysis technique was selected to deposit hematite films; this deposition technique presents several advantages: high reproducibility of stable samples, easy operation mode and common and low-cost lab equipment. An important goal that was reached with this work was the assembling and optimization of a spray pyrolysis experimental setup. During the preliminary tests of the setup, its configuration was continuously improved: the HPLC pump was replaced by a stainless steel pressurized tank, which allows more reproducible samples, the hot plate was painted with a black ceramic paint resistant to high temperature and the temperature uniformity assessed, etc.

This study focused on two key aspects to improve the photoresponse of hematite photoanodes: (1) optimization of the hematite morphology, which can significantly increase the water splitting photocurrent density; (2) reduction of the overpotential required by doping samples with different materials. For the hematite morphology control a DoE analysis was done to perform the optimization of the experimental setup with utmost rigor. Thanks to preliminary tests, the upper and lower limits of response variables were known. Then it was intended to maximize the response variable *j* (current density in $mA \cdot cm^{-2}$), by giving to the software the ranges of values for the process variables *v* (volume of solution deposited in ml), *h* (height of the spray nozzle in cm) and *t* (time between sprays in seconds). The software calculated a maximum current density that can be achieved of 0.525 $mA \cdot cm^{-2}$. This optimized value of current density was reached for a sprayed solution volume of 70 ml, a spray nozzle height of 20 cm and a 45 s time gap between sprays. The majority of the experimental results were in agreement with what was predicted by the DoE model and they were therefore covered in the margin of error for the confidence interval. The *Scaled Estimates* tool allowed concluding that the parameter that most influenced the samples performance was the amount of sprayed solution.

Samples prepared using the optimized experimental conditions defined by the DoE software were then pre-treated with TEOS, which allowed yielding a much higher current density and a lower onset potential. The pre-treated sample with TEOS showed a current density of 0.601 $mA \cdot cm^{-2}$ at 1.45 V_{RHE}, whereas the sample without pre-treatment showed only a current density of 0.427 $mA \cdot cm^{-2}$, which represented an increase of more than 29 % on the performance of the sample.

One of the most important contributions and perhaps the most innovative aspect of this work was studying the stability of the samples. The majority of works found in literature concerns mainly in improving the efficiency and less attention is given to stability. The stability test

consisted of subjecting the sample to simulated sunlight radiation for several hours. After 168 hours of sun exposure the sample showed an improvement in its performance of almost 7 % in relation to the first *I-V* measurement, having never lost efficiency over this period. Despite no loss of efficiency was observed in terms of current density, the onset potential of the dark current phenomenon started at lower potentials probably due to some detachment of hematite crystals from the FTO substrate.

After finding the optimal conditions for the deposition of hematite and after improving the performance of the samples by a pre-treatment with TEOS, a brief study on the influence of temperature on the morphology of the samples was made. It was concluded that the temperature of 450 °C was the optimal value for hematite deposition, allowing reaching a current density of 0.730 $mA \cdot cm^{-2}$. This value is in accordance with the best published results for the undoped hematite photoanodes produced under similar conditions. Top view SEM images confirmed that the deposition at 450 °C allowed obtaining crystals with a well-defined cubic shape in a very well organized structure, leading to better results of current density.

To further enhance the hematite photoresponse, silicon[IV] and titanium[IV] were chosen as dopants to be tested in this study. It was demonstrated that lower concentrations of Si[IV] as dopant and higher temperatures allow better current density results. Although improvements were evident under these conditions, the best result achieved with silicon doping was only of 0.559 $mA \cdot cm^{-2}$ at 1.45 V_{RHE}, being well below the value obtained in the best conditions for undoped samples with TEOS pre-treatment. Moreover, doping with silicon leaded to an increase on the onset potential and did not allowed obtaining *I-V* curves in tests under solar illumination with a well-defined plateau. Though, further optimizations are needed. Apparently Ti[IV] doping seemed to favour a better crystal growth evidenced by the colour of the produced samples, which showed a typical red-orange colour for hematite. Titanium doping also allowed producing more reproducible samples. Despite the improvement in performance of the samples in terms of working potential (onset potential moved to lower values and dark current moved to higher potentials), improvements in terms of current density were not achieved since the best result for a Ti doped sample was 0.501 $mA \cdot cm^{-2}$ at 1.45 V_{RHE}, which is not in accordance with previous reported results. Doping with Ti resulted in thicker films and this may explain the low values of photocurrent. Again, further optimizations should be pursued. Finally, it was shown that pre-treatment with TEOS only improved the performance of undoped samples.

Bearing in mind the defined work plan, it can be concluded that the major objective of assembling and optimizing an experimental setup for hematite deposition was fully addressed. The performance enhancement of the hematite photoanode was performed by implementing TEOS pre-treatment. Very interesting results were obtained in terms of doping materials and important conclusions were taken that can serve as starting point for other future works.

6 LIMITATIONS AND FUTURE WORK

In a future work, another DoE study should be performed to further optimize the doped hematite deposition conditions. The parameters that showed to be relevant to the hematite morphology development were temperature of the heating plate, hematite precursor solution concentration, volume of solution in each spray , annealing time and temperature and percentage of doping [11, 12, 14, 57, 61]. Adding all these parameters will result in a DoE study with much more experiments to be made, requiring a longer period for its implementation. It should be also tested the deposition on alternating multi-layers, decoration and different pre-treatments. The range of values of the time between sprays should also be extended [12, 61]. However, for that it is advisable to automate the spray control box, allowing adjusting the volume of deposited solution in each spray and the time between sprays automatically. This system is actually being acquired by the host lab.

As mentioned above, a SiO_x layer can reasonably act as an amorphous buffer that reduces the interfacial strain and should directly lead to better Fe_2O_3 film organization at an atomic level [12, 15, 36]. Regarding the principles that underlie these considerations, it would be interesting to test other materials to be applied in a layer between the FTO and the hematite particles in future studies, such as titanium, aluminium, gold, tin, among others.

It is important to remember that the stability test was performed on the sample from the series that achieved the best results so far. With more available time, it would be challenging to perform this test to the samples doped with different materials. In particular, testing the stability of the sample doped with Ti will be very interesting since Ti doping allowed the dark current appearing at higher potentials, which may prolong stability since the appearance of dark current at lower potentials was the motive for stopping the stability test developed within this work.

The best performing samples should be scaled-up up to 10 × 10 cm^2 to be tested in the new large prototype developed in the host lab.

7 REFERENCES

[1] E. World Commission on and Development, *Our common future*. Oxford; New York: Oxford University Press, 1987.

[2] E. Bozoglan, A. Midilli, and A. Hepbasli, "Sustainable assessment of solar hydrogen production techniques," *Energy,* vol. 46, pp. 85-93, 10// 2012.

[3] R. van de Krol and M. Grätzel, "Introduction," in *Photoelectrochemical Hydrogen Production*. vol. VIII, R. van de Krol, Grätzel, Michael, Ed., ed New York, USA: Springer Science+Business Media, 2012, pp. 3-11.

[4] P. P. Edwards, V. L. Kuznetsov, W. I. F. David, and N. P. Brandon, "Hydrogen and fuel cells: Towards a sustainable energy future," *Energy Policy,* vol. 36, pp. 4356-4362, 12// 2008.

[5] J. Nowotny, T. Bak, D. Chu, S. Fiechter, G. E. Murch, and T. N. Veziroglu, "Sustainable practices: Solar hydrogen fuel and education program on sustainable energy systems," *International Journal of Hydrogen Energy,* vol. 39, pp. 4151-4157, 3/18/ 2014.

[6] T. Abbasi and S. A. Abbasi, "'Renewable' hydrogen: Prospects and challenges," *Renewable and Sustainable Energy Reviews,* vol. 15, pp. 3034-3040, 8// 2011.

[7] L. Andrade, T. Lopes, H. A. Ribeiro, and A. Mendes, "Transient phenomenological modeling of photoelectrochemical cells for water splitting – Application to undoped hematite electrodes," *International Journal of Hydrogen Energy,* vol. 36, pp. 175-188, 1// 2011.

[8] R. Chaubey, S. Sahu, O. O. James, and S. Maity, "A review on development of industrial processes and emerging techniques for production of hydrogen from renewable and sustainable sources," *Renewable and Sustainable Energy Reviews,* vol. 23, pp. 443-462, 7// 2013.

[9] J. Keable and B. Holcroft, "Economic and Business Perspectives," in *Photoelectrochemical Hydrogen Production*. vol. VIII, R. van de Krol, Grätzel, Michael, Ed., ed New York, USA: Springer Science+Business Media, 2012, pp. 211-292.

[10] T. Lopes, "Characterization and Phenomoligal Modeling of Photoelectrochemical Cells for Hydrogen Production from Solar Energy " Doctor in Chemical and Biological Engineering, Chemical Engineering Department, Umiversity of Porto, Porto, 2014.

[11] A. Duret, "Mesoscopic thin films of hematite as photoanode for water photoelectrolysis," EPFL, 2005.

[12] F. Le Formal, "On the Morphology and Interfaces of Nanostructured Hematite Phtoanodes for Solar-Driven Water Splitting," EPFL, 2011.

[13] R. van de Krol, "Principles of Photoelectrochemical Cells," in *Photoelectrochemical Hydrogen Production*. vol. VIII, R. van de Krol, Grätzel, Michael, Ed., ed New York, USA: Springer Science+Business Media, 2012, pp. 13-67.

[14] I. Cesar, "Solar photoelectrolysis of water with translucent nano-structured hematite photoanodes," EPFL, 2007.

[15] K. Sivula, "Nanostructured α-Fe_2O_3 Photoanodes," in *Photoelectrochemical Hydrogen Production*, R. van de Krol and M. Grätzel, Eds., ed New York, USA: Springer Science+Business Media, 2012, pp. 121-156.

[16] K. Sivula, F. Le Formal, and M. Grätzel, "Solar Water Splitting: Progress Using Hematite (a-Fe2O3) Photoelectrodes," *ChemSusChem,* vol. 4, pp. 432-449, 2011.

[17] K. L. Hardee and A. J. Bard, "Semiconductor Electrodes: V . The Application of Chemically Vapor Deposited Iron Oxide Films to Photosensitized Electrolysis," *Journal of The Electrochemical Society,* vol. 123, pp. 1024-1026, July 1, 1976 1976.

[18] F. Le Formal, N. Tétreault, M. Cornuz, T. Moehl, M. Grätzel, and K. Sivula, "Passivating surface states on water splitting hematite photoanodes with alumina overlayers," *Chemical Science,* vol. 2, pp. 737-743, 2011.

[19] U. Bjoerksten, J. Moser, and M. Graetzel, "Photoelectrochemical Studies on Nanocrystalline Hematite Films," *Chemistry of Materials,* vol. 6, pp. 858-863, 1994/06/01 1994.

[20] K. Sivula, R. Zboril, F. Le Formal, R. Robert, A. Weidenkaff, J. Tucek, *et al.*, "Photoelectrochemical Water Splitting with Mesoporous Hematite Prepared by a Solution-Based Colloidal Approach," *Journal of the American Chemical Society,* vol. 132, pp. 7436-7444, 2010/06/02 2010.

[21] X. Zong, S. Thaweesak, H. Xu, Z. Xing, J. Zou, G. M. Lu, *et al.*, "A scalable colloidal approach to prepare hematite films for efficient solar water splitting," *Physical Chemistry Chemical Physics,* vol. 15, pp. 12314-12321, 2013.

[22] S. Xiong, J. Xu, D. Chen, R. Wang, X. Hu, G. Shen, *et al.*, "Controlled synthesis of monodispersed hematite microcubes and their properties," *CrystEngComm,* vol. 13, pp. 7114-7120, 2011.

[23] R. Wang, Y. Chen, Y. Fu, H. Zhang, and C. Kisielowski, "Bicrystalline hematite nanowires," *The Journal of Physical Chemistry B,* vol. 109, pp. 12245-12249, 2005.

[24] A. Mao, G. Y. Han, and J. H. Park, "Synthesis and photoelectrochemical cell properties of vertically grown α-Fe2O3 nanorod arrays on a gold nanorod substrate," *Journal of Materials Chemistry,* vol. 20, pp. 2247-2250, 2010.

[25] Gurudayal, S. Y. Chiam, M. H. Kumar, P. S. Bassi, H. L. Seng, J. Barber, *et al.*, "Improving the Efficiency of Hematite Nanorods for Photoelectrochemical Water Splitting by Doping with Manganese," *ACS Applied Materials & Interfaces,* vol. 6, pp. 5852-5859, 2014/04/23 2014.

[26] Y. Qiu, S.-F. Leung, Q. Zhang, B. Hua, Q. Lin, Z. Wei, *et al.*, "Efficient Photoelectrochemical Water Splitting with Ultrathin films of Hematite on Three-Dimensional Nanophotonic Structures," *Nano letters,* vol. 14, pp. 2123-2129, 2014.

[27] H. E. Prakasam, O. K. Varghese, M. Paulose, G. K. Mor, and C. A. Grimes, "Synthesis and photoelectrochemical properties of nanoporous iron (III) oxide by potentiostatic anodization," *Nanotechnology,* vol. 17, p. 4285, 2006.

[28] M. Paulose, H. E. Prakasam, O. K. Varghese, L. Peng, K. C. Popat, G. K. Mor, *et al.*, "TiO2 nanotube arrays of 1000 μm length by anodization of titanium foil: phenol red diffusion," *The Journal of Physical Chemistry C,* vol. 111, pp. 14992-14997, 2007.

[29] Y.-S. Hu, A. Kleiman-Shwarsctein, A. J. Forman, D. Hazen, J.-N. Park, and E. W. McFarland, "Pt-doped α-Fe2O3 thin films active for photoelectrochemical water splitting," *Chemistry of Materials,* vol. 20, pp. 3803-3805, 2008.

[30] J. Y. Kim, G. Magesh, D. H. Youn, J.-W. Jang, J. Kubota, K. Domen, *et al.*, "Single-crystalline, wormlike hematite photoanodes for efficient solar water splitting," *Sci. Rep.,* vol. 3, 09/17/online 2013.

[31] I. Cesar, A. Kay, J. A. Gonzalez Martinez, and M. Grätzel, "Translucent Thin Film Fe2O3 Photoanodes for Efficient Water Splitting by Sunlight: Nanostructure-Directing Effect of Si-Doping," *Journal of the American Chemical Society,* vol. 128, pp. 4582-4583, 2006.

[32] W.-J. An, E. Thimsen, and P. Biswas, "Aerosol-chemical vapor deposition method for synthesis of nanostructured metal oxide thin films with controlled morphology," *The Journal of Physical Chemistry Letters,* vol. 1, pp. 249-253, 2009.

[33] M. Cornuz, M. Grätzel, and K. Sivula, "Preferential Orientation in Hematite Films for Solar Hydrogen Production via Water Splitting," *Chemical Vapor Deposition,* vol. 16, pp. 291-295, 2010.

[34] K. Sivula, F. L. Formal, and M. Grätzel, "WO3− Fe2O3 Photoanodes for Water Splitting: A Host Scaffold, Guest Absorber Approach," *Chemistry of Materials,* vol. 21, pp. 2862-2867, 2009.

[35] A. Duret and M. Grätzel, "Visible Light-Induced Water Oxidation on Mesoscopic α-Fe2O3 Films Made by Ultrasonic Spray Pyrolysis," *The Journal of Physical Chemistry B,* vol. 109, pp. 17184-17191, 2005/09/01 2005.

[36] F. Le Formal, M. Grätzel, and K. Sivula, "Controlling Photoactivity in Ultrathin Hematite Films for Solar Water-Splitting," *Advanced Functional Materials,* vol. 20, pp. 1099-1107, 2010.

[37] E. W. McFarland, P. Zhang, A. Kleiman-Shwarsctein, Y. Hu, N. Hight-huf, and R. Garland, "II. H. 5 Photoelectrochemical Hydrogen Production Using New Combinatorial Chemistry Derived Materials."

[38] A. Kay, I. Cesar, and M. Grätzel, "New Benchmark for Water Photooxidation by Nanostructured α-Fe2O3 Films," *Journal of the American Chemical Society,* vol. 128, pp. 15714-15721, 2006/12/01 2006.

[39] S. D. Tilley, M. Cornuz, K. Sivula, and M. Grätzel, "Light-Induced Water Splitting with Hematite: Improved Nanostructure and Iridium Oxide Catalysis," *Angewandte Chemie,* vol. 122, pp. 6549-6552, 2010.

[40] J. Brillet, M. Grätzel, and K. Sivula, "Decoupling Feature Size and Functionality in Solution-Processed, Porous Hematite Electrodes for Solar Water Splitting," *Nano Letters,* vol. 10, pp. 4155-4160, 2010/10/13 2010.

[41] J. Deng, J. Zhong, A. Pu, D. Zhang, M. Li, X. Sun, *et al.*, "Ti-doped hematite nanostructures for solar water splitting with high efficiency," *Journal of Applied Physics,* vol. 112, pp. -, 2012.

[42] R. van de Krol, "Photoelectrochemical Measurements," in *Photoelectrochemical Hydrogen Production*. vol. VIII, R. van de Krol and M. Grätzel, Eds., ed New York, USA: Springer Science+Business Media, 2012, pp. 13-67.

[43] G. Rahman and O.-S. Joo, "Facile preparation of nanostructured [small alpha]-Fe2O3 thin films with enhanced photoelectrochemical water splitting activity," *Journal of Materials Chemistry A,* vol. 1, pp. 5554-5561, 2013.

[44] F. Ribeiro, "Heating Plate Thermal Analysis Study with SolidWorks," 2013.

[45] S. S. Shinde, R. A. Bansode, C. H. Bhosale, and K. Y. Rajpure, "Physical properties of hematite α-Fe 2 O 3 thin films: application to photoelectrochemical solar cells," *Journal of Semiconductors,* vol. 32, p. 013001, 2011.

[46] S. Shen, C. X. Kronawitter, D. A. Wheeler, P. Guo, S. A. Lindley, J. Jiang, *et al.*, "Physical and photoelectrochemical characterization of Ti-doped hematite photoanodes prepared by solution growth," *Journal of Materials Chemistry A,* vol. 1, pp. 14498-14506, 2013.

[47] "JMP - The Statistical Discovery Software, Manual de Utilizador," FEUP, Porto, LEPABE.

[48] M. J. W. P. J. Anderson, *RSM simplified : optimizing processes using response surface methods for design of experiments*. New York, N.Y.: Productivity Press, 2005.

[49] M. Catarino, A. Ferreira, and A. Mendes, "Study and optimization of aroma recovery from beer by pervaporation," *Journal of Membrane Science,* vol. 341, pp. 51-59, 9/30/ 2009.

[50] R. van de Krol, Y. Liang, and J. Schoonman, "Solar hydrogen production with nanostructured metal oxides," *Journal of Materials Chemistry,* vol. 18, pp. 2311-2320, 2008.

[51] L. A. Marusak, R. Messier, and W. B. White, "Optical Absorption Spectrum of Hematite, α-Fe_2O_3 near IR to UV," *Journal of Physics and Chemistry of Solids,* vol. 41(9), pp. 981-984, 1980

[52] S. Kumari, A. P. Singh, Sonal, D. Deva, R. Shrivastav, S. Dass, *et al.*, "Spray pyrolytically deposited nanoporous Ti4+ doped hematite thin films for efficient photoelectrochemical splitting of water," *International Journal of Hydrogen Energy,* vol. 35, pp. 3985-3990, 5// 2010.

[53] V. R. Satsangi, S. Kumari, A. P. Singh, R. Shrivastav, and S. Dass, "Nanostructured hematite for photoelectrochemical generation of hydrogen," *International Journal of Hydrogen Energy,* vol. 33, pp. 312-318, 1// 2008.

[54] C. Jorand Sartoretti, B. D. Alexander, R. Solarska, I. A. Rutkowska, J. Augustynski, and R. Cerny, "Photoelectrochemical Oxidation of Water at Transparent Ferric Oxide Film Electrodes," *The Journal of Physical Chemistry B,* vol. 109, pp. 13685-13692, 2005/07/01 2005.

[55] D. J. Eaglesham and M. Cerullo, "Dislocation-free Stranski-Krastanow growth of Ge on Si(100)," *Physical Review Letters,* vol. 64, pp. 1943-1946, 04/16/ 1990.

[56] C. Jorand Sartoretti, M. Ulmann, B. D. Alexander, J. Augustynski, and A. Weidenkaff, "Photoelectrochemical oxidation of water at transparent ferric oxide film electrodes," *Chemical Physics Letters,* vol. 376, pp. 194-200, 7/17/ 2003.

[57] L. Wang, C.-Y. Lee, and P. Schmuki, "Ti and Sn co-doped anodic α-Fe2O3 films for efficient water splitting," *Electrochemistry Communications,* vol. 30, pp. 21-25, 5// 2013.

[58] R. M. Navarro Yerga, M. C. Alvarez-Galván, F. Vaquero, J. Arenales, and J. L. G. Fierro, "Chapter 3 - Hydrogen Production from Water Splitting Using Photo-Semiconductor Catalysts," in *Renewable Hydrogen Technologies*, L. M. Gandía, G. Arzamendi, and P. M. Diéguez, Eds., ed Amsterdam: Elsevier, 2013, pp. 43-61.

[59] I. Cesar, K. Sivula, A. Kay, R. Zboril, and M. Grätzel, "Influence of Feature Size, Film Thickness, and Silicon Doping on the Performance of Nanostructured Hematite Photoanodes for Solar Water Splitting," *The Journal of Physical Chemistry C,* vol. 113, pp. 772-782, 2009/01/15 2008.

[60] M. Rioult, H. Magnan, D. Stanescu, and A. Barbier, "Single Crystalline Hematite Films for Solar Water Splitting: Ti-Doping and Thickness Effects," *The Journal of Physical Chemistry C,* vol. 118, pp. 3007-3014, 2014/02/13 2014.

[61] A. A. Akl, "Microstructure and electrical properties of iron oxide thin films deposited by spray pyrolysis," *Applied Surface Science,* vol. 221, pp. 319-329, 1/15/ 2004.

APPENDIX A - TEMPERATURE STUDY FOR DIFFERENT SURFACE MATERIALS WHERE SAMPLES WERE PLACED ON

In the spray pyrolysis setup used in this work a heating plate with 4 thermal resistors was used. The surface of the plate was painted with a black ceramic paint resistant to high temperature to allow obtaining a temperature distribution as much uniform as possible. The heating plate was side protected with a ceramic material coated with aluminium foils to ensure adequate thermal insulation. To protect the paint of the plate and to ensure the temperature distribution uniformity after several depositions it was necessary to place the samples on top of a protective surface (so that the sprayed solution did not damage the paint). Due to the heat losses between the thermal resistors and the glass substrate placed on the surface of the heating plate the temperature value entered in the control box did not correspond to the temperature measured on the substrate. It was therefore necessary to conduct a study for different heating surfaces to determine which would be the best material to allow obtaining the desired temperature on the substrates. The results of this study are shown in Figure A.1

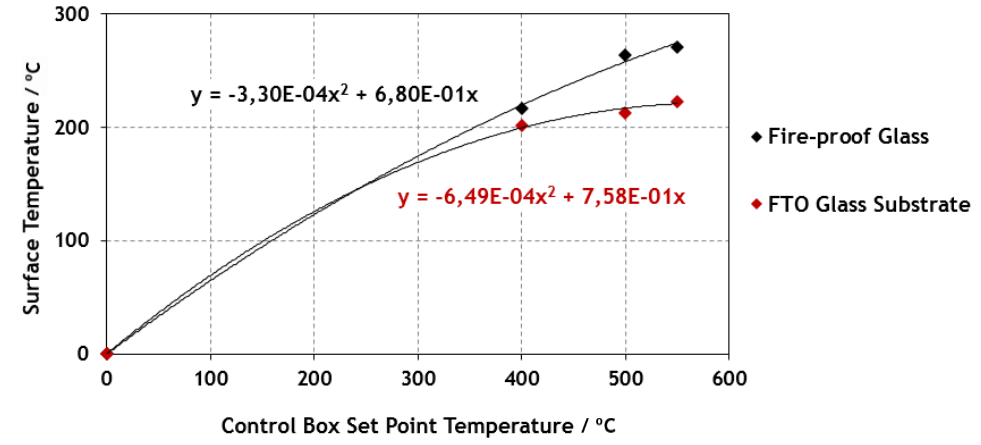

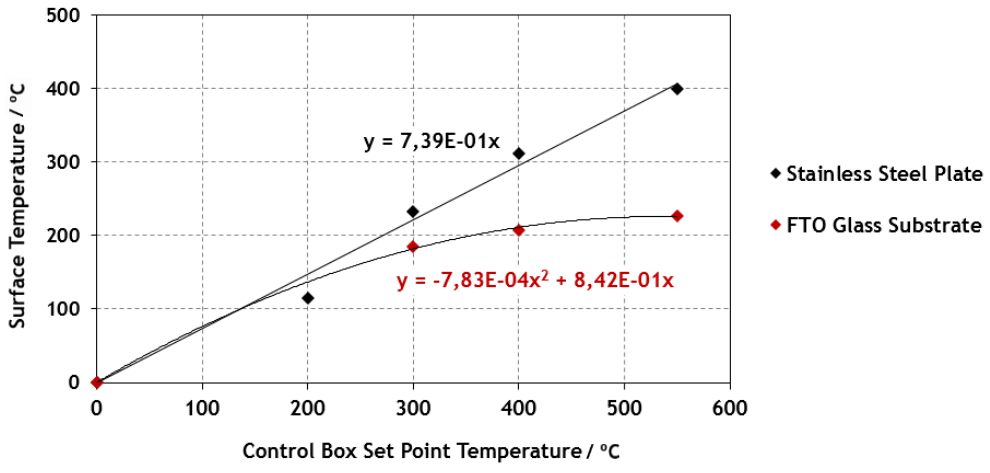

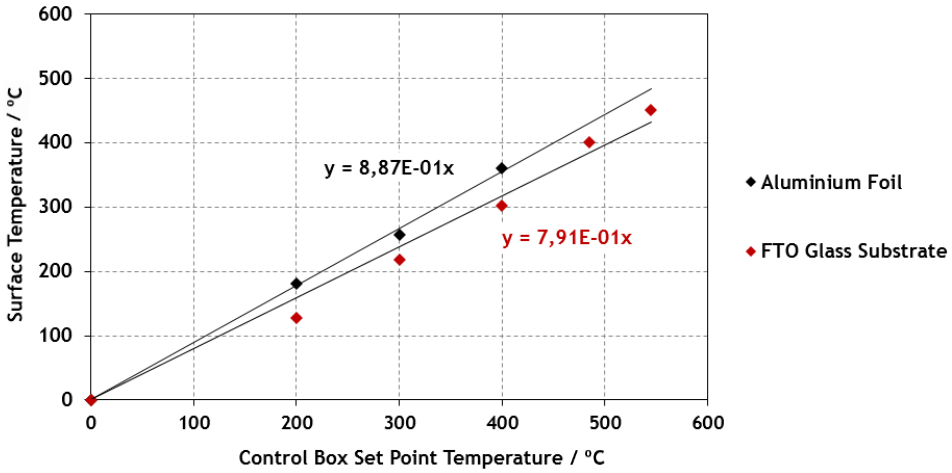

Figure A.1 *- Relation between the control box set point temperature and measured temperature on the glass substrate placed on different surfaces.*

Obtained results show that the only surface that allowed achieving the desired temperature on the glass substrates and showed the best relation with the temperature entered in the control box was the aluminium foil. Based on this study, the samples were always placed in an aluminium foil during hematite depositions. The temperature values that should be inserted in the set point for different desired temperatures on the glass substrate are shown in Table A.1

Table A.1 *- Measured temperatures in the FTO glass substrate placed in an aluminium foil for different set point temperatures.*

Set point temperature (ºC)	Glass substrate temperature (ºC) [3]
200	180.6
300	257.5
400	360
485	400
545	450

[3] The temperature reached on the glass substrate was manually measured with a thermocouple.

APPENDIX B - THERMAL IMAGER TEMPERATURE STUDY ON THE HEATING PLATE

As shown in Appendix A, it was necessary to conduct a temperature study to determine what would be the necessary temperature value to be introduced in the control box so that the desired temperature in the substrate could be reached. This study was done with a thermocouple placed manually on the substrate. However, this could not be a very accurate way to measure the temperature, due to the permanent movement of air and due to the difficulty of ensuring a static position of the thermocouple. Therefore, a study with a thermal imager was carried out, which allowed seeing which temperatures were really being achieved in the surface of the heating plate.

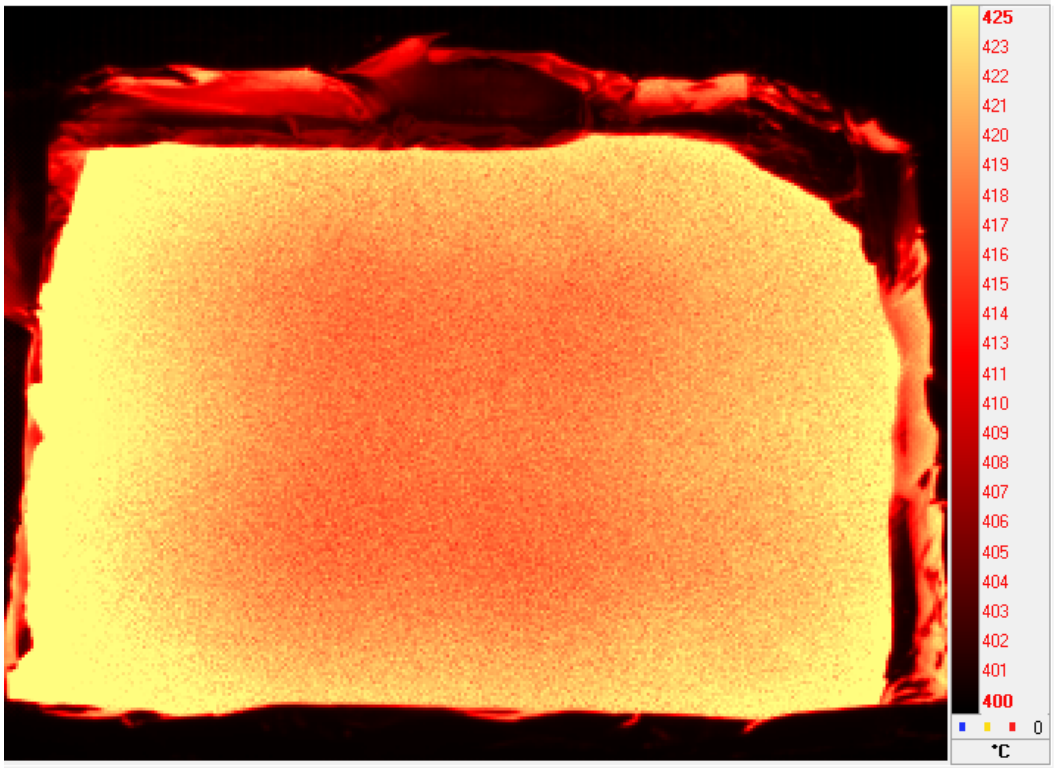

***Figure B.1** - Thermal image of the temperature reached on the surface of the heating plate for a 400 ºC desired value (in relation to a 485 ºC value inserted in the control box).*

The study previously done with the thermocouple showed that a value of 485 ºC should be inserted in the control box to obtain 400 °C on the substrate surface where the hematite film would be deposited. Figure B.1 shows that in the central area of the plate a temperature of ~415 ºC was achieved, which should correspond to 400 °C on the substrate surface due to heat losses. The study that was previously done could therefore be validated. It should be noted that the heating plate was painted in order to obtain a thermal distribution as uniform as possible. As Figure B.1 shows this goal was achieved. In the edges of the plate slightly higher

temperatures were reached probably due to the aluminium foil coating which was placed to avoid high heat losses in this areas. The thermal insulation effect was also achieved.

APPENDIX C – SEM TOP VIEW IMAGES WITH LOWER MAGNIFICATION

In order to confirm that the deposited hematite films were uniform, SEM analyses were performed with lower magnification (1000 ×). As it can be seen for all studies hematite films showed a uniform appearance.

VOLUME STUDY

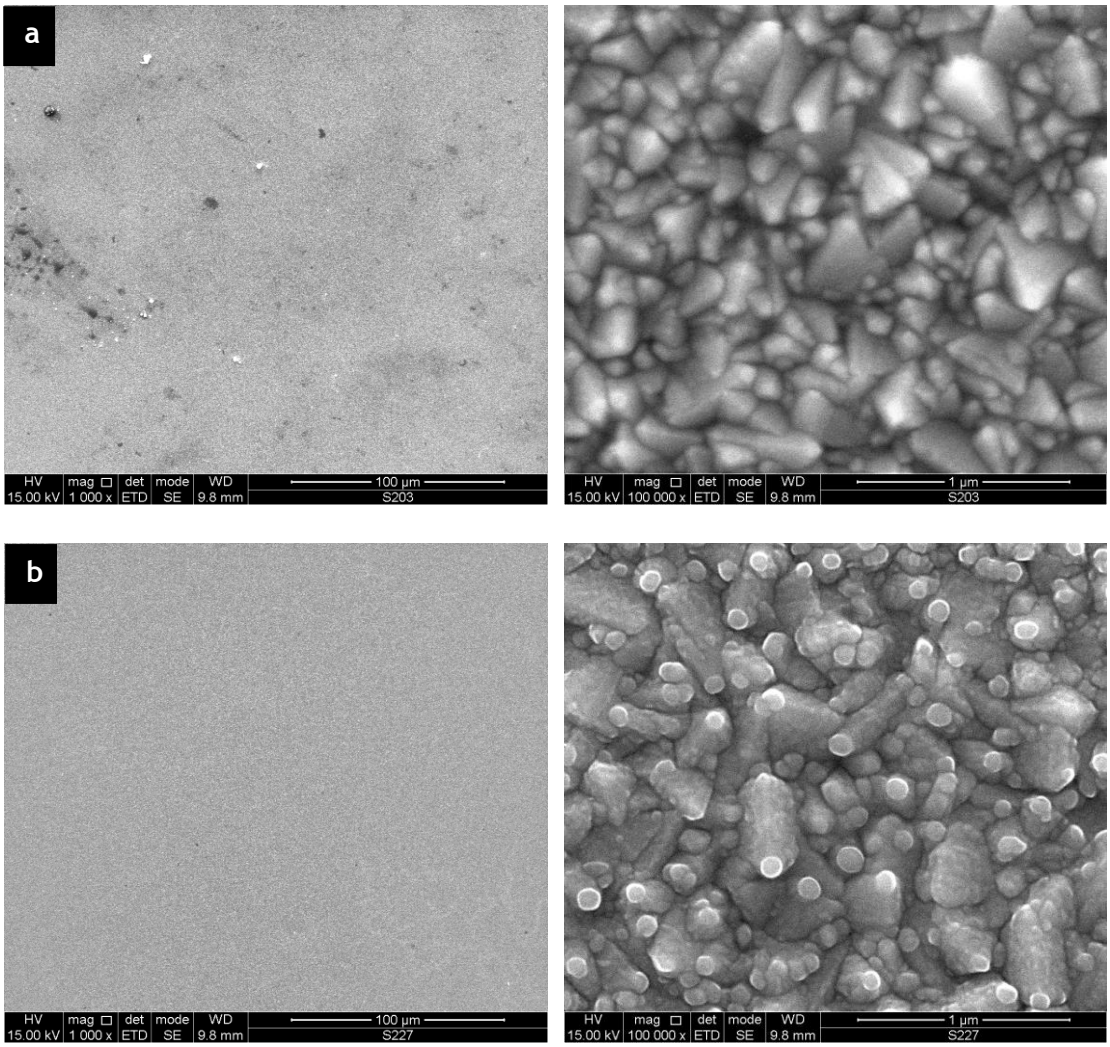

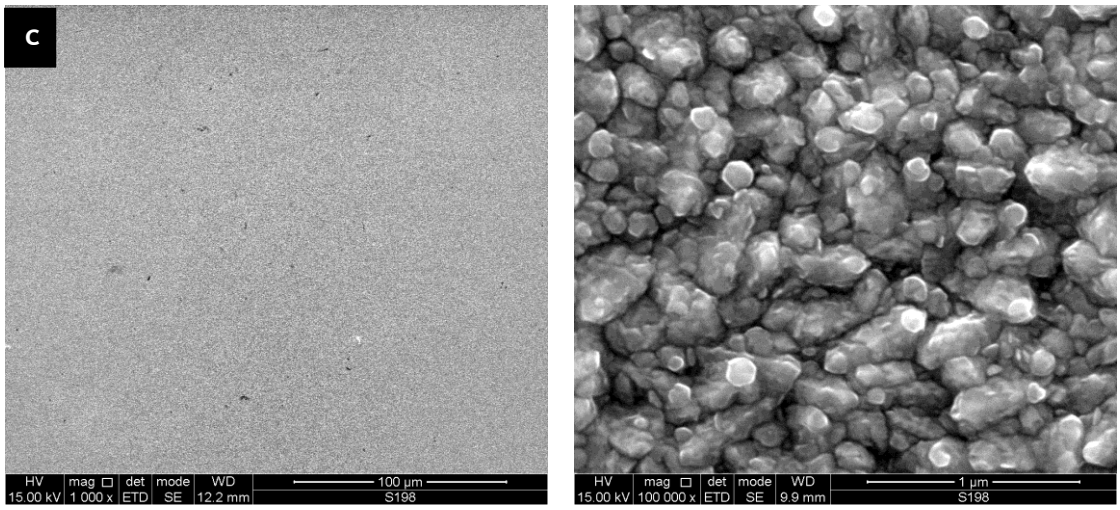

Figure C.1 *- Top view SEM images (1000 × magnification on the left and 100 000 × on the right) of the samples produced with different volumes of sprayed solution in the same experimental conditions (spray nozzle height of 20 cm and 45 s between sprays at 400 ºC); a) 45ml; b) 70 ml; c) 95 ml;*

TIME BETWEEN SPRAYS STUDY

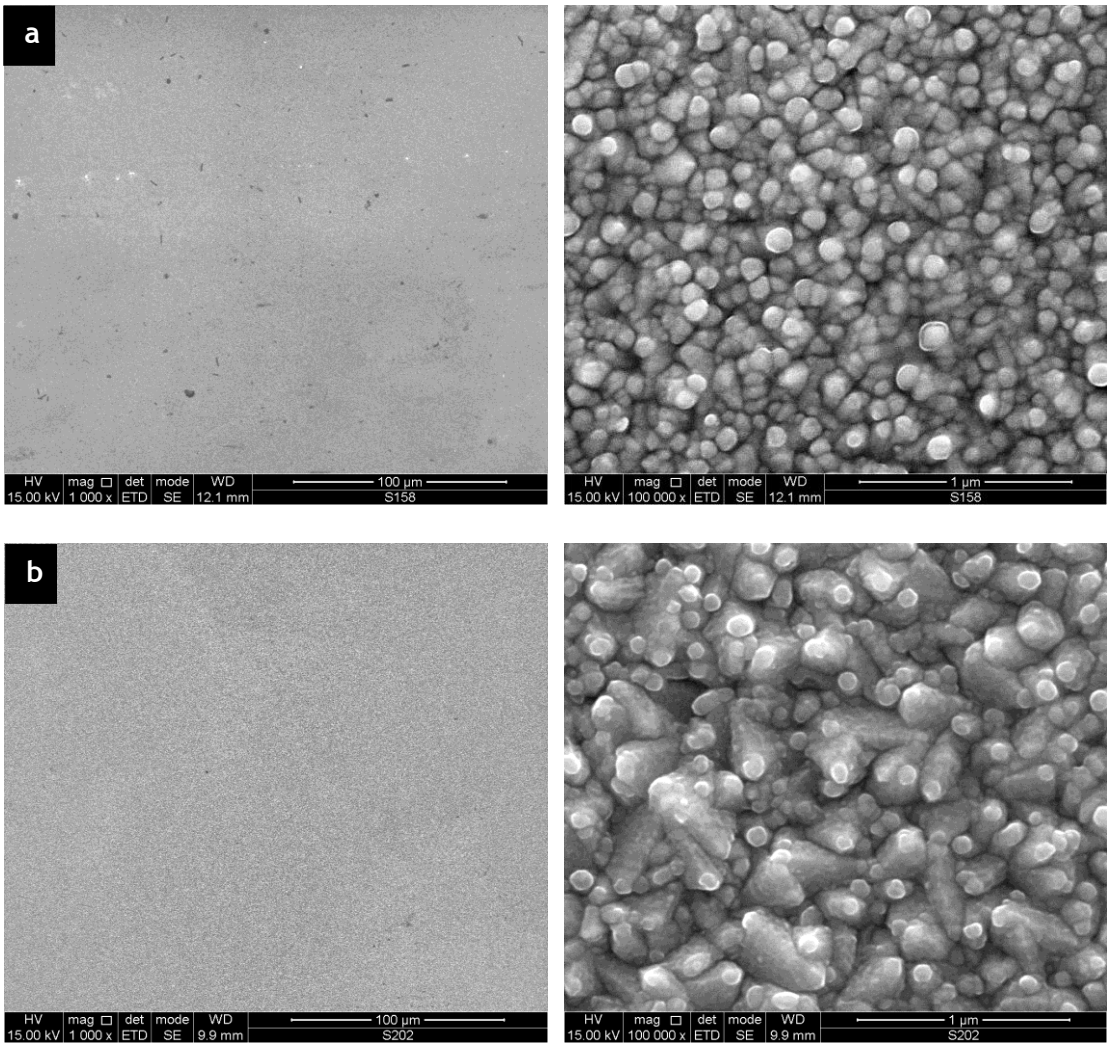

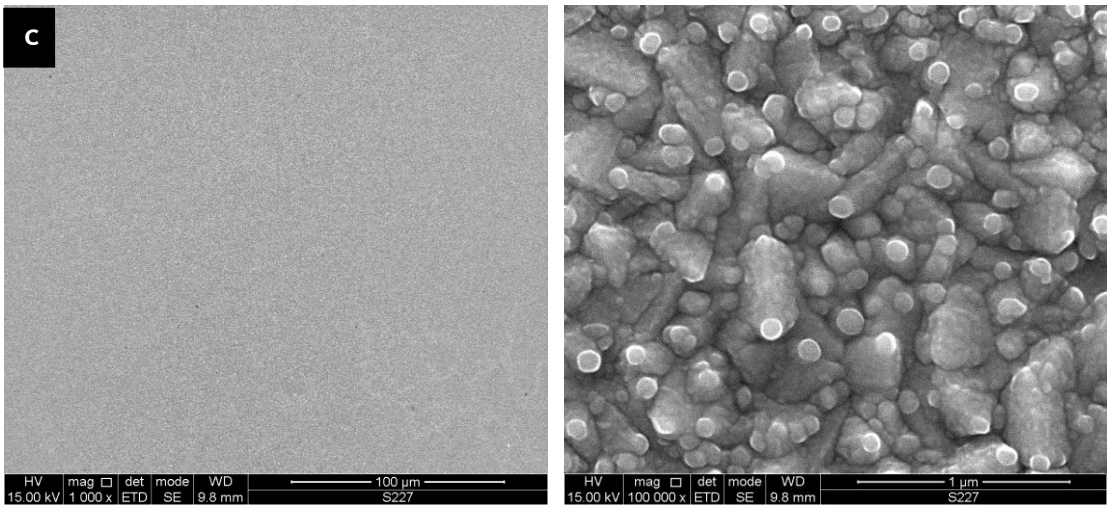

***Figure C.2** - Top view SEM images (1000 × magnification on the left and 100 000 × on the right) of the samples produced with different times between sprays under the same experimental conditions (spray nozzle height of 20 cm and 70 ml of sprayed solution at 400 ºC); a) 15 s; b) 30 s; c) 45 s;*

TEMPERATURE STUDY

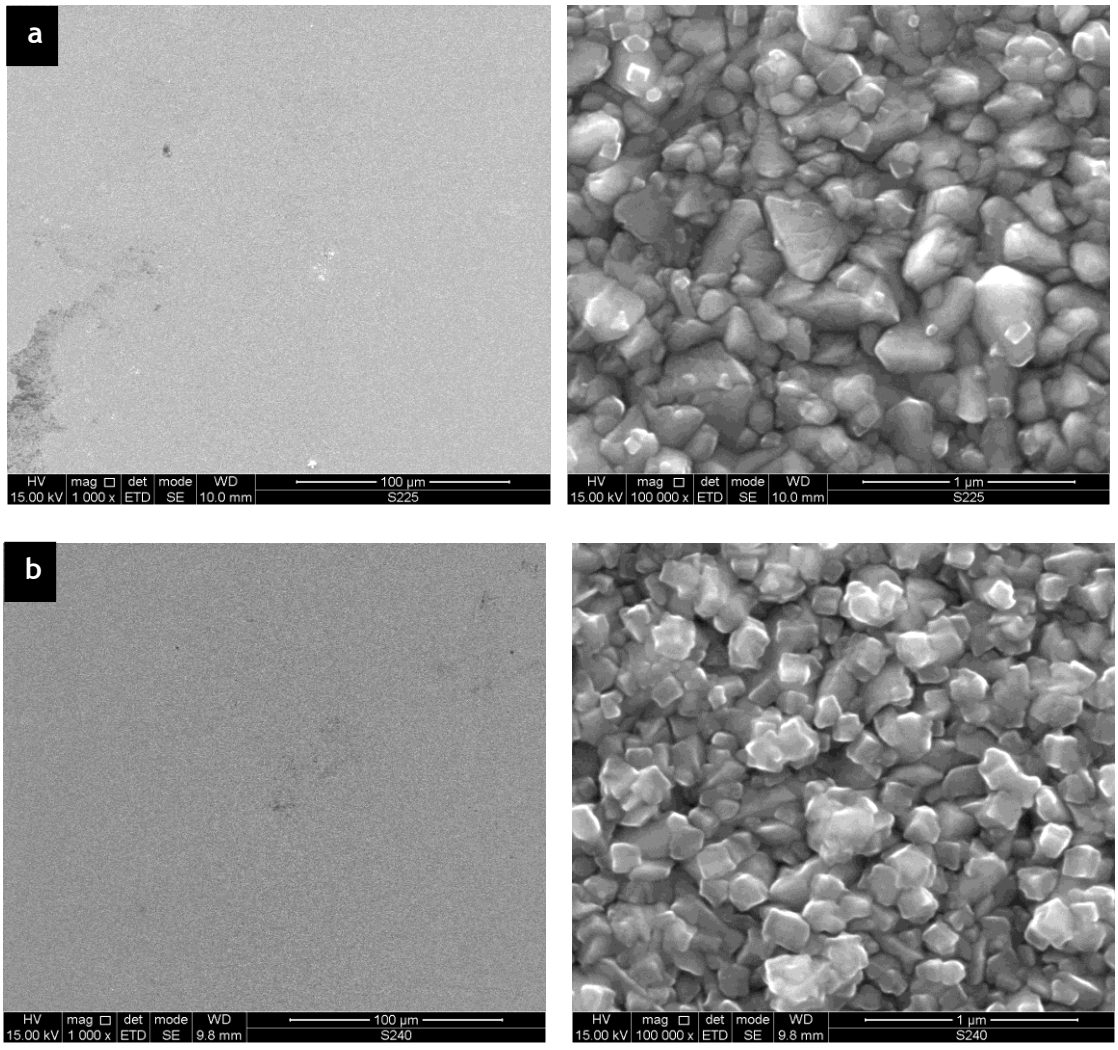

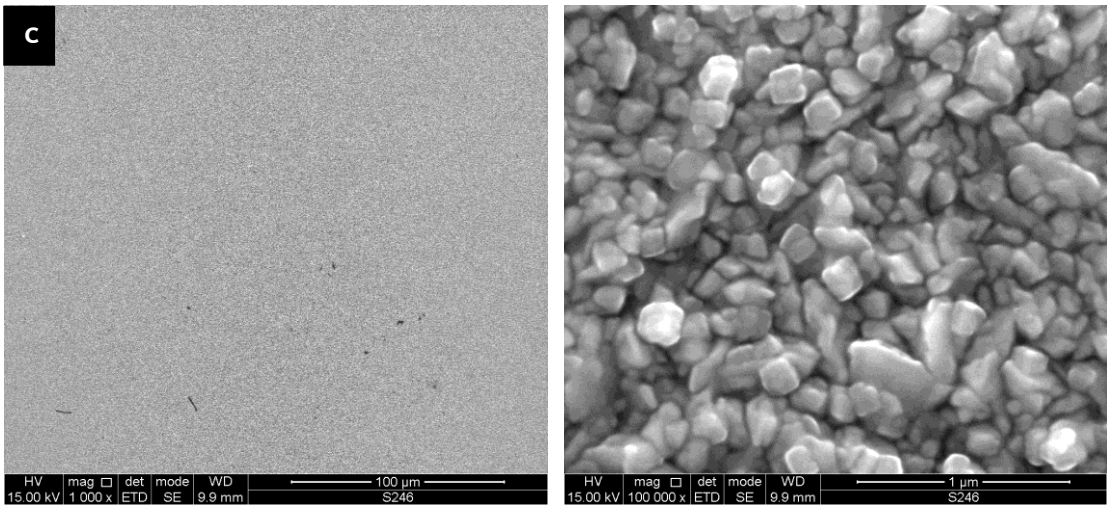

Figure C.3 *- Top view SEM images (1000 × magnification on the left and 100 000 × on the right) of the samples produced at different temperatures under the same experimental conditions (spray nozzle height of 20 cm, 70 ml of sprayed solution, 45 s between sprays and pre-treatment with TEOS); a) 400 ºC s; b) 450 ºC; c) 500 ºC;*

APPENDIX D – PREDICTED RESPONSE VALUES IN THE DOE STUDY

For each set of experimental conditions defined by the JMP software a photocurrent density response value was predicted. These results are presented in Table D.1.

***Table D.1** – Predicted photocurrent density values for each set of experimental conditions of the DoE study.* [4]

Volume of deposited solution (ml)	Spray height (cm)	Time between sprays (s)	Average current density at 1.45 V_{RHE} potential ($mA \cdot cm^{-2}$) for the 3 samples series	Predicted photocurrent for 1.45 potential ($mA \cdot cm^{-2}$)	Difference between the predicted and obtained average value ($mA \cdot cm^{-2}$)
45	40	15	1.81×10^{-1}	2.24×10^{-1}	4.25×10^{-2}
45	40	45	2.40×10^{-1}	3.05×10^{-1}	6.43×10^{-2}
45	20	15	3.41×10^{-1}	3.80×10^{-1}	3.89×10^{-2}
95	30	30	3.76×10^{-1}	4.39×10^{-1}	6.22×10^{-2}
45	30	30	3.79×10^{-1}	3.40×10^{-1}	3.89×10^{-2}
95	40	15	3.79×10^{-1}	4.15×10^{-1}	3.58×10^{-2}
95	20	15	3.98×10^{-1}	3.78×10^{-1}	2.02×10^{-2}
95	20	45	4.13×10^{-1}	4.30×10^{-1}	1.71×10^{-2}
70	20	30	4.34×10^{-1}	4.71×10^{-1}	3.66×10^{-2}
70	40	30	4.34×10^{-1}	4.29×10^{-1}	4.43×10^{-3}
70	30	15	4.35×10^{-1}	4.56×10^{-1}	2.14×10^{-2}
45	20	45	4.40×10^{-1}	4.24×10^{-1}	1.54×10^{-2}
70	30	30	4.44×10^{-1}	4.73×10^{-1}	2.93×10^{-3}
70	30	30	4.62×10^{-1}	4.73×10^{-1}	1.10×10^{-2}
70	30	45	4.78×10^{-1}	5.23×10^{-1}	4.52×10^{-2}
70	30	30	4.86×10^{-1}	4.73×10^{-1}	1.24×10^{-2}
95	40	45	5.07×10^{-1}	5.04×10^{-1}	3.21×10^{-3}

Results of Table D.1 show that all the obtained photocurrent densities in the conducted experiments are in agreement with the values predicted by the model, being therefore within the error ($\pm$ 0.0786 $mA \cdot cm^{-2}$) for the confidence interval.

[4] Important to mention that the values in the table are organized from the lowest to the highest photocurrent density value.

APPENDIX E - HEMATITE THIN FILM GROWTH MODES

Currently there are three well known crystal growth modes in thin films. In the Volmer-Weber (VW) growth mode, adatom-adatom interactions are stronger than those of the adatom[5] with the surface, leading to the formation of three-dimensional clusters or islands. During Frank–van der Merwe (FM) growth, adatoms attach preferentially to surface sites resulting in atomically smooth, two dimensional fully formed layers. This layer-by-layer growth indicates that complete films form before growth of subsequent layers. Stranski–Krastanov (SK) growth is an intermediary process characterized by both 2D layer and 3D island growth. Transition from the layer-by-layer 2D growth to 3D island-based growth occurs at a critical layer thickness which is highly dependent on the substrate and film chemical and physical properties, such as surface energies and lattice parameters [1, 2]. Figure E.1 is a schematic representation of these three main growth modes for thin films.

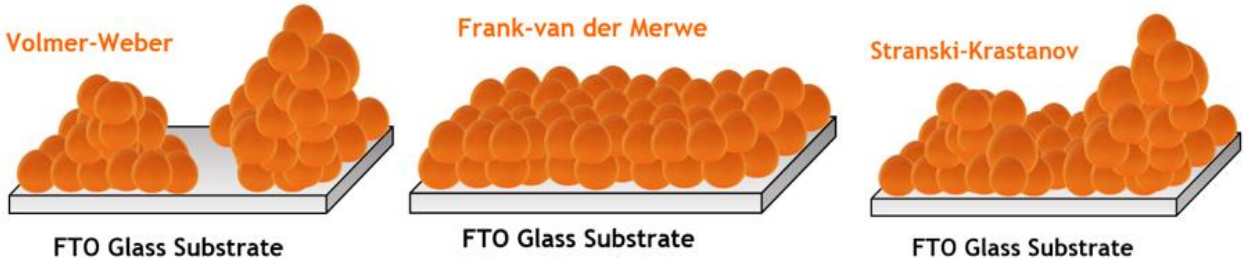

Figure E.1 *- Three primary modes of thin-film growth.*

In the SK growth mode while initial film growth follows a FM mechanism, positive non-trivial amounts of strain energy accumulate in the deposited layers. At a critical thickness, this strain induces a sign reversal in the chemical potential, which leads to a switch in the growth mode. At this point nucleate islands are energetically favourable to develop and further growth occurs by a VW type mechanism [1, 2].

REFERENCES

1. Le Formal, F., *On the Morphology and Interfaces of Nanostructured Hematite Phtoanodes for Solar-Driven Water Splitting*. 2011, EPFL.
2. Eaglesham, D.J. and M. Cerullo, *Dislocation-free Stranski-Krastanow growth of Ge on Si(100).* Physical Review Letters, 1990. **64**(16): p. 1943-1946.

[5] Adatom - atom that lies on a crystal surface and can be thought of as the opposite of a surface vacancy clusters or islands.

APPENDIX F - DARK CURRENT OF THE FTO GLASS SUBSTRATE

As Figure F.1 shows when potential is applied to the conductive substrate the dark current phenomenon appears to values slightly below 1.6 V_{RHE} which indicates that the electrolysis of water may occur because of electrochemical phenomena that are not related to the photo response of the sample.

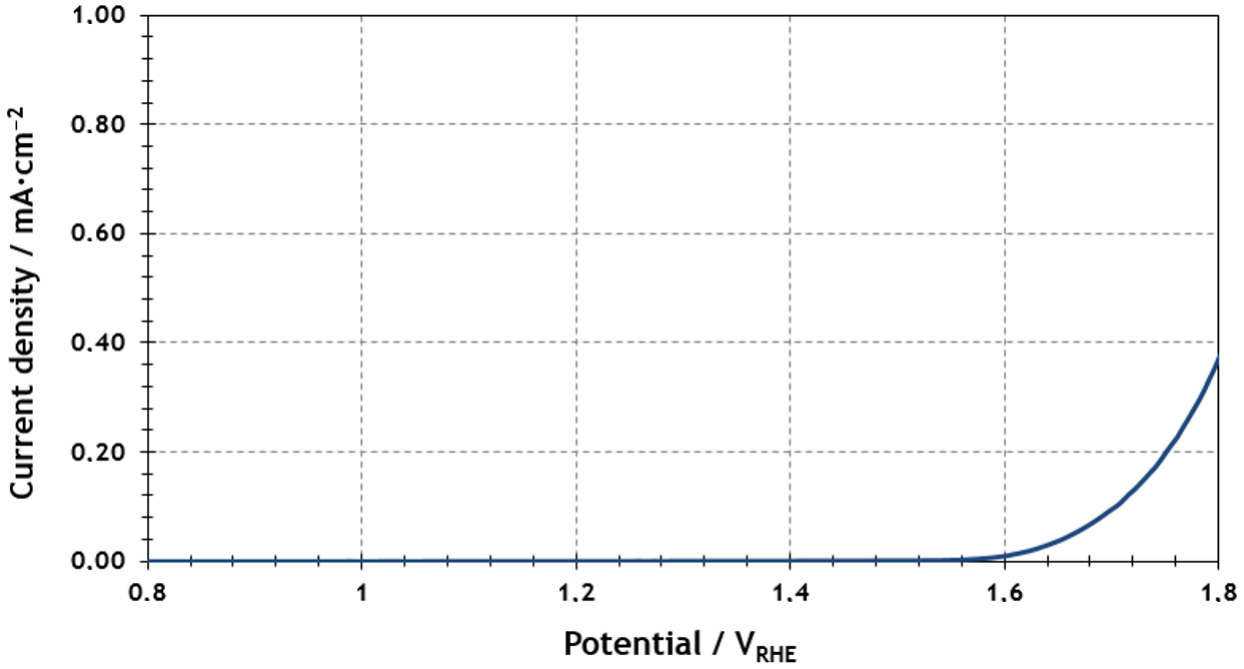

***Figure F.1** - Current density vs. potential curve obtained in the dark for a sample of the FTO glass substrate.*

APPENDIX G - EFFECT OF PLACING A STAINLESS STEEL CYLINDRICAL PROTECTIVE STRUCTURE IN THE SPRAY PYROLYSIS SETUP

As mentioned before it was also studied if placing a stainless steel cylindrical protective structure around samples (17 cm diameter and 17 cm height) would create a more favourable deposition environment, either in terms of temperature stabilization during the tests or in terms of spray droplets dispersion. The change in the configuration of the experimental setup is shown in Figure G.1.

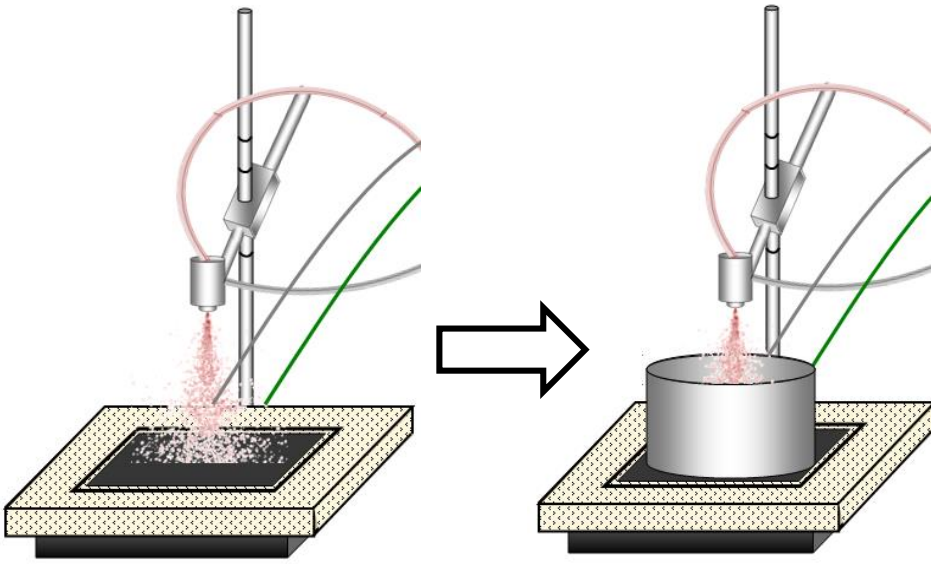

***Figure G.1** – Placement of the stainless steel cylindrical protective structure in the experimental spray pyrolysis setup.*

In this test the samples were produced under the optimal deposition conditions (70 ml of sprayed 10 mM $Fe(AcAc)_3$ solution, 20cm spray nozzle height, 45 s between sprays and with TEOS pre-tratment). As it can be seen from the obtained results shown in Figure G.2, the expected improvements in the sample photocurrent production were not observed. The samples produced with the stainless steel cylindrical protective structure showed worse performance both in terms of produced photocurrent (only 0.480 $mA \cdot cm^{-2}$ at 1.45 V_{RHE}) and in terms of onset potential. These results may be due to adverse effects on the sample temperature and due to the creation of a whirlwind of droplets that could have impaired the uniformity of the hematite film.

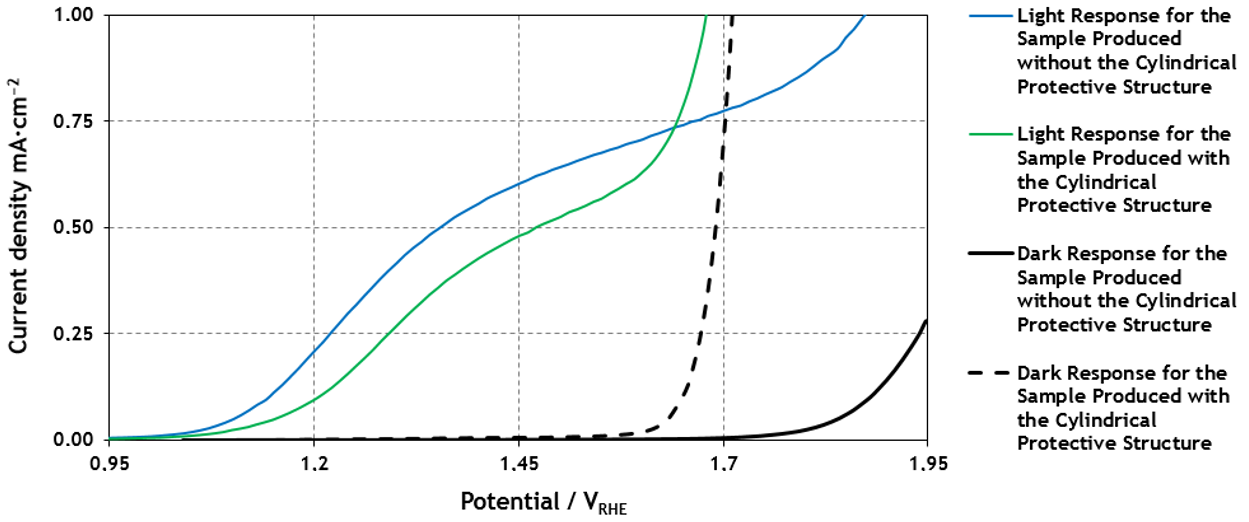

***Figure G.2** - I-V characteristic curves of the prepared photoanodes in the dark (dashed and solid black lines) and under simulated solar illumination (AM 1.5 G 100* mW·cm^{-2}*, coloured lines) with and without the stainless steel cylindrical protective structure.*

APPENDIX H - CHARGE RECOMBINATION EFFECT ON PHOTOANODES EFFICIENCY

As already mentioned in this work hematite (α-Fe_2O_3) satisfies many requirements for photoelectrochemical hydrogen production: a small bandgap (2.1 eV) that allows 15.3 % of theoretical solar-to-hydrogen (STH) efficiency (or photocurrent generation of 12.6 $mA \cdot cm^{-2}$ at 1.23 V_{RHE} under 1-sun irradiation), excellent stability under alkaline conditions, low price, and environmentally friendly characteristics. However, hematite has a critical drawback, which is the extremely poor electrical conductivity due to a hole diffusion length of 2–4 nm [1]. Thus most of the hematite anodes have exhibited very low PEC performance because of the excessive charge recombination. Consequently charge carriers get trapped in the bulk of hematite and recombine to lower the efficiency. The three key limiting processes are: (1) bulk recombination via bandgap states, (2) directly electron loss to holes in the valence band and (3) surface recombination. Some studies have indicated that hematite with a well-defined nanocrystalline morphology could be one way to increase the current yield by minimising the distance the charge carriers have to diffuse before reaching the interface [2]. It is important to remember that a trap is an energy level lying within the bandgap able to capture charges (holes or electrons) from the valence or the conduction band and a recombination centre is an energy level able to capture charges (holes and electrons) from both the valence and the conduction bands [3]. As it is known, a better crystallinity reduces the recombination phenomenon, since the electron has to travel a shorter path to achieve the conductive substrate, as shown in Figure H.1.

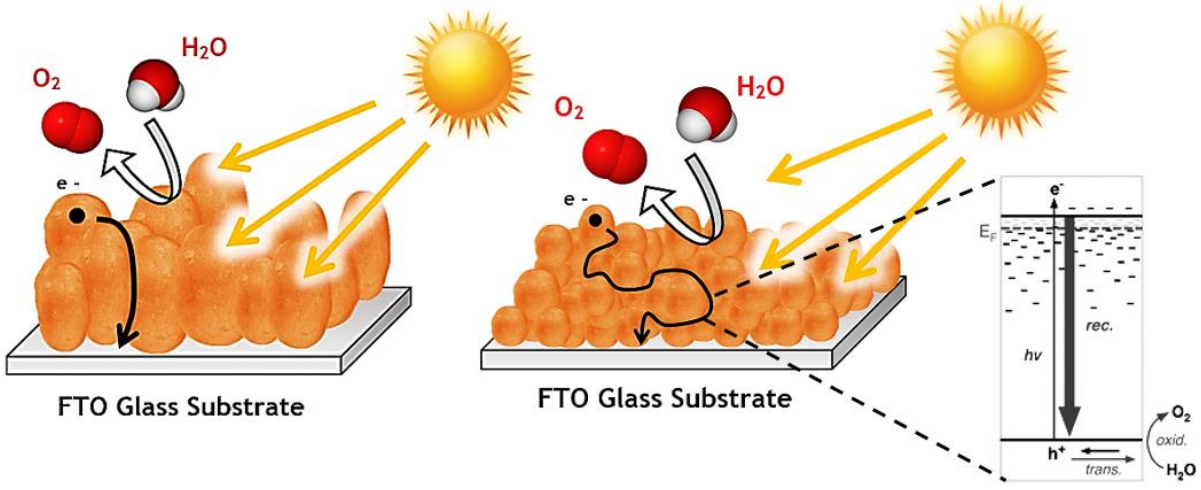

Figure H.1 *- Schematic representation of the path of an electron (charge carrier) in a hematite photoanode with well-developed crystals (on the right) and a photoanode with lower crystallinity (on the left) where the effects of the recombination phenomenon are enhanced.*

In the situation shown on the right dislocations and grain boundaries are two typical formations that can appear and represent also two important families of crystal defects. Both may introduce energy levels in the bandgap since they may act as donors or acceptors. Dislocations commonly appear near the surface of the crystal lattice and represent atoms that are poorly coordinated due to the crystal lattice discontinuity. On the other hand grain boundaries occur at the interface of two different crystals. So it is expected that in a morphology where there are many small poorly developed crystals more grain boundaries can appear. All these defects may form traps or recombination centres [3].

REFERENCES

1. J. Y. Kim, G. Magesh, D. H. Youn, J.-W. Jang, J. Kubota, K. Domen, et al., "Single-crystalline, wormlike hematite photoanodes for efficient solar water splitting," Sci. Rep., vol. 3, 09/17/online 2013.
2. T. Lindgren, H. Wang, N. Beermann, L. Vayssieres, A. Hagfeldt, and S.-E. Lindquist, "Aqueous photoelectrochemistry of hematite nanorod array," Solar Energy Materials and Solar Cells, vol. 71, pp. 231-243, 2002.
3. Duret, "Mesoscopic thin films of hematite as photoanode for water photoelectrolysis," EPFL, 2005.